Investigations of Earthquakes and Other Seismic Sources in Regions of Volcanism

Thesis by
Holly K. Eissler

In Partial Fulfillment of the Requirements
for the Degree of
Doctor of Philosophy

California Institute of Technology
Pasadena, California

1986

(submitted May 28, 1986)

Acknowledgements

The research presented in this thesis was primarily supported by grant EAR-8313223 of the Earth Sciences Division of the National Science Foundation, awarded to H. Kanamori and D. G. Harkrider for the global seismological study of volcanic eruptions.

I am extremely grateful to my thesis advisor, Professor Hiroo Kanamori, for his support of my scientific aspirations. Not only is he an impeccable scientist, but he has the valuable human qualities of humor, modesty, objectivity, and patience. I thank Professor David G. Harkrider for his unique perspective and friendship, and for suggesting a collaborative project to study the air waves from Mt. St. Helens that contained the seeds of this thesis. I thank Professor Robert P. Sharp for his ability to teach geology in the field, even to someone from urban Illinois, and all of the faculty of the Seismological Laboratory for working very hard to provide graduate students with a secure, liberal, and unencumbered environment in which to study science. Larry Ruff and Karen McNally provided guidance during my first year at Caltech.

Thanks to my wonderful close friends and associates, particularly Lucianita, Vicki, Jenny, Jerry, the Deacon, Creaven, Chris S., Phyllis B., Chris W., Jen, Sally, Pat and J^2. I would like to acknowledge my immediate family, Charles and Betty Eissler, Gertrude Poggendorf, Mark Eissler, and Melanie Rottmann, for their constant faith in me.

--

Abstract

Source properties of earthquakes in Hawaii and seismological aspects of explosive volcanic eruptions are examined in three chapters. In Chapter 1, source depths are estimated for all earthquakes larger than magnitude 6 on the island of Hawaii since 1940 by comparing relative amplitudes of short-period surface waves to body waves. Rayleigh wave excitation functions are calculated versus source depth, and the calculation is compared with observed data and calibrated using known depths of recent earthquakes. In general, results show that large earthquakes near the volcanic flanks and fault systems are shallow ($\leq$ 20 km), but those near active volcanic centers can be deeper ($\sim$ 50 km). Two earthquakes with the largest depth estimates (40-55 km and 35-50 km) occurred under the active volcanoes Mauna Loa and Kilauea, preceding eruptions by three days and 14 months respectively. As a check on the data set, which consisted of Pasadena seismograms alone, M_S values assigned from many global amplitude readings were compared with those from Pasadena amplitudes for worldwide earthquakes. Global M_S values on the average are 0.05 magnitude units larger than M_S values from Pasadena amplitudes.

In Chapter 2, the horizontal single-force source used to model seismic radiation from the Mt. St. Helens landslide is investigated as the source of the $M_S = 7.1$ Kalapana, Hawaii earthquake. The azimuthal radiation pattern of 100 s Love waves is two-lobed, consistent with a horizontal single-force source. The observed surface deformation is also more consistent with the single force than the conventional double-couple shear dislocation source. The single force is a crude representation of motion of a large slide mass that is partially decoupled from the Earth. The interpretation is that the bulk of seismic radiation from the Kalapana earthquake was

produced by large-scale slumping of the south flank of Kilauea volcano. The peak amplitude f_o of the force time function is estimated at 1 x 10^{20} dyne from Love and Rayleigh surface waves. The peak acceleration inferred from the seismic force is 10 - 100 cm s^{-2}, comparable to that of gravity on a gently inclined plane.

In Chapter 3, far-field seismograms were searched for signals associated with recent large volcanic eruptions to examine whether models of the volcano as a seismic source derived for Mt. St. Helens are applicable to other explosive volcanoes. The 1982 eruption of El Chichón in Mexico produced Rayleigh waves and body waves that were marginally recorded at IDA and SRO stations less than 40^o away; still, several characteristics of the eruption can be inferred from the seismic waves. Near-field seismograms of smaller eruptions at Mt. Asama, Japan, were found to be comparable in size to smaller secondary eruptions of Mt. St. Helens, and appear to have a more complicated source. Atmospheric pressure waves recorded on barographic instruments from several large explosive eruptions are compared and show differences in signal duration, amplitude, and characteristic period that are indicative of the overall size of the eruption.

Table of Contents

Introduction

The work presented in this thesis comprises three of the research projects undertaken during my graduate work at the Seismological Laboratory. Although each is essentially a separate body of work, all are related in that they are concerned with the relationship of seismology and volcanism.

In Chapters 1 and 2, I examine source properties of large earthquakes on Hawaii, one of the world's most copious sites of volcanism. Work on Chapter 1 began abruptly with the occurrence of a large (M_L =6.6) earthquake on the island of Hawaii on November 16, 1983. The epicenter was very near the volcano Mauna Loa, which had not experienced a large eruption since 1950, but had been showing signs of renewed magmatic activity. A large earthquake near Mauna Loa preceded the 1950 eruption by 78 hours. In light of the 1950 experience, we asked how the November 1983 earthquake was related to the renewed activity at Mauna Loa.

To answer this question, it was necessary to reexamine the 1950 earthquake. I quickly became acquainted with general properties of Hawaiian earthquakes. Moderate to large events are not unusual; there have been 12 earthquakes on Hawaii since 1940 larger than magnitude 6. However, events over magnitude 7 are rare. The moderate event size plus Hawaii's isolated location in the middle of the Pacific Ocean means that Hawaiian events are poorly recorded globally. Frequently, even precise locations of earthquakes were poorly known prior to 1960, when the U.S. Geological Survey began to instrument the island with a dense seismic network. Depth patterns of earthquakes after 1960 quickly revealed that a focused "plumbing system" or active magma zone, well-defined by seismicity, existed to at least 60 km depth under the active volcanoes, whereas seismicity on the remainder of the island is usually

shallow and more diffuse. Thus the depth of an earthquake can be an indication of its relationship to volcanism.

The problem of data availability for events before 1960 remained. Fortunately, the Seismological Laboratory at Pasadena, California had been operating a battery of broad-band instruments since the 1930's, long before plate tectonics had channeled research focus from local to global study of earthquakes. The Pasadena collection includes records of all the large Hawaiian events since at least 1940. We exploited the differences in these records — all from essentially the same source location with the same travel path — to study source properties of the large Hawaiian earthquakes, particularly their depth. The most notable difference between events was the different relative amplitudes of surface waves to body waves, which is a direct function of source depth. In Chapter 1, I present depth estimates of large Hawaiian earthquakes obtained by a calculation of surface wave excitation versus source depth that was calibrated using known depths of recent earthquakes. This method can be applied anywhere there is a suite of seismograms from tightly clustered earthquakes recorded at the same station, so that the effects of differential propagation or site response can be ignored. Chapter 1 appeared as a research article in the *Journal of Geophysical Research, 91,* 1986, with Hiroo Kanamori. While the project was underway, Mauna Loa erupted in March 1984, in one of the most voluminous eruptions of its history.

Chapters 2 and 3 concern very different geographical areas and phenomena, but they were both originally motivated by the eruption of Mt. St. Helens volcano in Washington 1980. Mt. St. Helens produced a rich data set of global seismic observations that was analyzed extensively by researchers at Caltech. Two elements were observed in the seismic source of Mt. St. Helens: a very long-period horizontal force, created by the landslide motion of a large mass on the north slope of the mountain;

and shorter-period vertical forces, arising from the explosions themselves.

In Chapter 2, I reexamine the source of a large Hawaiian earthquake that caused unusually large seaward displacement of the entire south flank of Kilauea volcano. I show that the earthquake can be interpreted as a horizontal force event, much like the Mt. St. Helens landslide. The scales of the two events are very different; the Mt. St. Helens landslide involved a mass of 5×10^{15} grams, whereas the mass involved in the Kalapana, Hawaii earthquake is estimated to be much larger, 10^{18}–10^{19} grams. The character of the events was also different. The Mt. St. Helens event was a classical landslide, where the block became detached and traveled about 700 meters. The Kalapana event involved an onland area of roughly 10 x 50 km. The block motion was not entirely free but stretched the south flank seaward, with the toe of the block eventually deteriorating into a slide or rubble flow undersea. For this reason I prefer to call the Kalapana earthquake a "slump event." However both events can be modeled with the same non-double-couple source, the horizontal single force. The slump event appears to be a common deformation mode on Hawaii, where the unbuttressed and constantly growing volcanic edifice moves seaward under gravitational and magmatic forces. The main importance of my result is that this process can occur seismically with an observably different seismic source than a conventional earthquake. This class of seismic events can occur in areas traditionally thought of as non-seismogenic, such as a passive continental margin where there is a large accumulation of sediments.

In Chapter 3, I investigate seismic records of explosive volcanic eruptions to see if the model of a volcanic explosion developed for Mt. St. Helens could be applied to other volcanoes. I also discuss records of atmospheric waves arising from explosive volcanic eruptions. Much of this project involved identifying the largest eruptions and

search for existing records. Aside from Mt. St. Helens, very few volcanoes have been large enough to produce global seismic recordings. In spite of the scarcity of the data set, I am able to present some interesting far-field seismic and atmospheric observations of explosive volcanoes. Hopefully, work presented in Chapter 3 will serve to carve out areas of investigation of volcanoes by remote methods that will be useful to future researchers as better quality data become available.

Chapter 1

Depth Estimates of Large Earthquakes on the Island of Hawaii Since 1940

Abstract

Although hypocenters of earthquakes on the island of Hawaii are now routinely assigned to within 5 km, depth was a poorly determined parameter until the early 1960's. However, the 1950-1960 period was very active both in volcanic eruptions and large earthquakes. Source depths for the 12 largest Hawaiian earthquakes (magnitude 6 or greater) since 1940 are estimated from the ratios of body and surface wave amplitudes recorded at Pasadena, California. Excitation functions for Rayleigh waves are calculated as a function of source depth for the two dominant periods in the Pasadena records, 8 s and 20 s. Theoretical body wave amplitudes are determined from synthetic seismograms. Calculated ratios are very sensitive to source depth; for example, amplitudes of 8-s Rayleigh waves diminish by a factor of 300 between depths of 10 km and 50 km. This is a much larger effect than the fault geometry, which we estimate to be a factor of 4 between representative focal mechanisms. Estimated depths for post-1960 earthquakes agree fairly well with the instrumental depths. In general, large earthquakes near the volcanic flanks and fault systems are shallow ($\leq$ 20 km). Two earthquakes of magnitude 6 occurred under the volcanoes Mauna Loa (in 1950) and Kilauea (in 1951); they preceded major eruptions by 3 days and 14 months, respectively, and had the largest depth estimates at 40-55 km and 35-50 km. M_S values assigned from global amplitudes are compared with those assigned from Pasadena amplitudes alone, for 70 events in 1973-1974 with $5.1 \leq M_S \leq 6.0$. The global values are only slightly larger (0.05 magnitude units) than the Pasadena values, indicating that Pasadena amplitudes are on the average representative of the event magnitude.

1. Introduction

Several moderate to large earthquakes, magnitude 6 or greater, occurred on the island of Hawaii in the 1950's. Some of these were spatially and temporally associated with volcanic eruptions. Two events in 1950 and 1951 under the summits of Mauna Loa and Kilauea preceded eruptions of the volcanoes, the first by less than 1 week. Although the depths of these events were not well determined, there was some indication that the 1951 Kilauea earthquake was deep, about 40 or 50 km. In general, the larger earthquakes in Hawaii are much shallower, $<$20 km, and they are not necessarily associated with specific eruptions or volcanic centers.

The depth of an earthquake is significant because it may indicate how the seismic activity is associated with the volcanic process. For example, some of the deepest seismicity on Hawaii consists of intense swarms of small earthquakes at about 50-60 km beneath Kilauea. Deep swarms have long been thought to signify the movement of magma upward into the shallow reservoirs of the volcanic system. Small shallow earthquakes may also occur due to rock failure induced by increased magmatic pressure in the reservoirs. Many of the large shallow earthquakes are in response to regional tectonic stresses that arise from the building up of the large volcanic load on the old seafloor. Although all earthquakes in Hawaii are connected in some way to its volcanism, some events appear to have a more primary relationship to the volcanic process than others.

Modern array coverage on Hawaii began to develop in 1955-1960. Hypocenters assigned after 1960 are quite reliable for the larger earthquakes. Before this, depths were estimated primarily from noninstrumental information, such as isoseismal patterns. Here, we use a simple technique to arrive at another estimate of depth or, at

least, relative depth ranking, for the largest earthquakes in Hawaii since 1940.

Seismic instruments in Pasadena, California, have been continuously recording for over 50 years. Prior to worldwide standardization of equipment in 1963, these instruments were among the highest gain in operation. Pasadena was also one of the closest stations to Hawaii and thus could record its intermediate-magnitude events. Events of magnitude 6 were clearly recorded on both long- and short-period Pasadena instruments, and the relative amplitudes of surface and body waves can be compared in the two different period bands. While the excitation of Rayleigh waves decreases rapidly with source depth, body wave amplitudes are a much weaker function of depth. By comparing calculations of the relative excitation of these waves as a function of source depth to the Pasadena data set, estimates of the depths of the events can be obtained.

2. Earthquake Data

Seismicity on the island of Hawaii is illustrated by Figure 1*a*, which shows all earthquakes greater than magnitude 3.5 since 1970 in the NOAA catalog. Locations of the volcanic centers and major fault zones are shown in Figure 1*b*. The Hilina, Kealakekua, and Kaoiki fault systems show normal motion and were built up predominantly by large-scale gravitational slumping of the volcanic flanks (Stearns, 1966; Swanson et al., 1976; Lipman, 1980). In general, most of the earthquakes occur on the south part of the island, near the volcanic centers of Mauna Loa and Kilauea, or the volcanically active east rift zone of Kilauea, and near the Kaoiki and Hilina fault zones. The Kaoiki zone has numerous earthquakes, related to the tectonics of

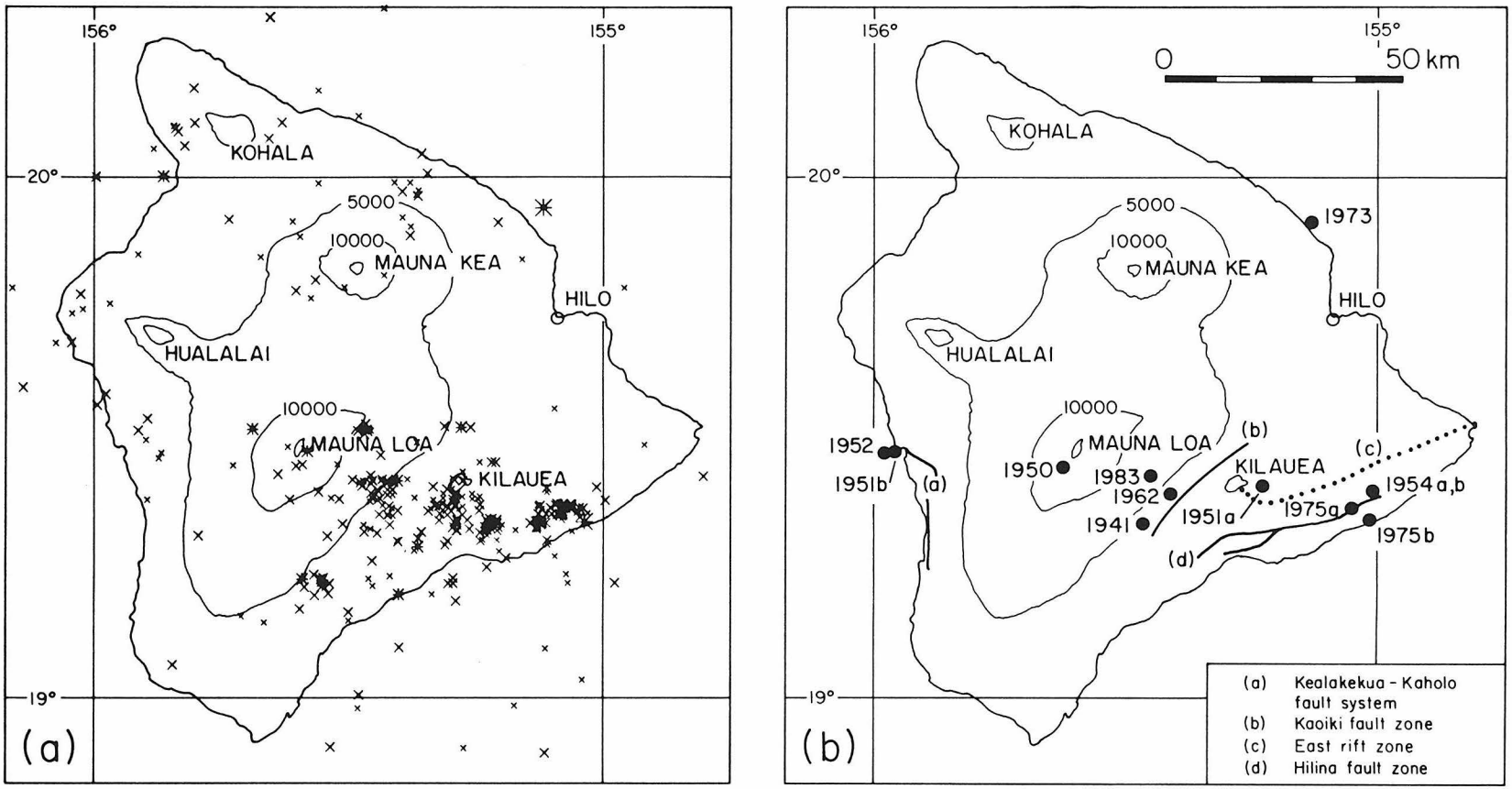

Figure 1. (*a*) Seismicity of the island of Hawaii, from the NOAA catalog. Events are those with $M_L \geq 3.5$ from 1970 to 1981. Small crosses indicate magnitudes less than 4.0; larger crosses, 4.0 - 4.9; asterisks, 5.0 and larger. Volcanic centers are named. (*b*) Map showing the locations of the 12 events chosen for the depth study, and some fault zones of the island.

Mauna Loa's southeast flank and the relative activity of Mauna Loa versus Kilauea volcanism. Displacement of Kilauea's south flank occurs in the area of the east rift zone and the Hilina fault system and is the primary cause of earthquakes there (Swanson et al., 1976; Tilling et al., 1976; Koyanagi et al., 1972). The first hypocenter studies on the island showed that most of the seismicity in the Kaoiki zone is $\leq$ 15 km deep; in the Hilina zone, $\leq$ 20 km; in the east rift zone, about 10 km; and under Kilauea, $\leq$ 60 km (Eaton and Murata, 1960).

We chose to study all earthquakes since 1940 with magnitudes of 6 and larger. The 12 selected events are shown in Figure 1*b* and listed in Table 1. Magnitudes for the earthquakes from 1941 to 1954 are from Gutenberg and Richter (1954) or the Seismological Laboratory in Pasadena, California. These magnitudes (denoted by M) are usually equivalent to the standard M_S (Geller and Kanamori, 1977). The m_b and M_S magnitudes for the events between 1973 and 1983 are from the monthly bulletin *Preliminary Determination of Epicenters* published by the U.S. Geological Survey, and M_L values are from the Hawaiian Volcano Observatory (HVO). In all cases, the locations listed are either estimated or instrumental epicenters assigned by HVO. The five earthquakes since 1962 have precisely determined hypocenters from the Hawaiian network; these events are used primarily as reference events for the depth estimates of the earlier earthquakes.

Descriptions of the pre-1960 study events were found in *The Volcano Letters*, compiled by the staff of the HVO [U.S. Geological Survey, 1925-1955]. The reports frequently contained information on isoseismal patterns, damage and surface cracking, estimated epicenters, and depth ranges of the earthquakes. In what follows, we briefly summarize this information. It should be noted that high-gain, short-period instruments did not begin operation on Hawaii until 1955. In 1950 there were only

Table 1

Study Events

Date	m_b	M or M_S	M_L	Latitude, °N	Longitude, °W	Estimated or Instrumental Depth, km	Estimated Depth From This Study, km
Sept. 25, 1941		6		19.3	155.4 est.*	~11	35-40
May 30, 1950		6 1/4		19.5	155.6 est.	--	>40
April 23, 1951a		6 1/2		19.4	155.2 est.	~40-50	35-40
Aug. 21, 1951b		6.9		19.5	155.9 est.	--	20-25
May 23, 1952		6.0		19.48	155.98 inst.	~10	~40
March 30, 1954a		6.0		19.4	155.0 est.	~20	20-25
March 30, 1954b		6.5		19.4	155.0 est.	~20	~10
June 28, 1962		5 3/4	6.1	19.40	155.41 inst.	8	25-30
April 26, 1973	6.0	6.1	6.2	19.90	155.13 inst.	45	~40
Nov. 29, 1975a	5.8	5.1	5.7	19.37	155.04 inst.	10	25-30
Nov. 29, 1975b	6.0	7.1	7.2	19.35	155.01 inst. *	10	10-15
Nov. 16, 1983	6.4	6.7	6.6	19.43	155.45 inst.	12	15-20

* Indicates whether the epicenter is estimated (est.) or instrumental (inst.).

five seismic stations on the island, many of which were equipped only with horizontal instruments with longer response periods. These instruments were frequently rendered inoperable by shaking during the larger events. Synchronized time signals were just beginning in 1952 (Klein and Koyanagi, 1980). Thus the earthquake locations (and certainly instrumental depths) prior to 1960 are of much lower quality than those of recent events.

September 25, 1941. This earthquake occurred on the southeast flank of the volcano Mauna Loa. The epicenter shown on Figure 1*b* was estimated from the geographic description in *The Volcano Letter* 473. Although HVO did assign a depth of 11 km, depth assignments in this period should be considered dubious due to the sparse instrumentation. (Routine depth assignments were discontinued in subsequent *Volcano Letters* from this period.)

May 30, 1950. This event occurred on or below the upper southwest rift of Mauna Loa near its summit. Its occurrence in part caused the HVO to immediately release an eruption alert. Mauna Loa erupted 78 hours later, in one of its largest eruptions for at least 1000 years (Macdonald, 1954; Lipman, 1980). Shaking disabled all of the instruments on the island, but intensity 6 was reported along the western coast. No depth estimate was given. We checked the basis of the 6 1/4 magnitude figure by examining the supporting notepads for Gutenberg and Richter (1954) (Goodstein et al., 1980). We found that this was assigned from the amplitude of the Pasadena record only. However, the other events in this study with comparable body wave amplitudes on the Pasadena instrument had magnitudes between 5 3/4 and 6.9 that were assigned on the basis of more than one station.

April 23, 1951. This earthquake was located just east of the crater of Kilauea. Based on the uniformity of intensity distribution, a depth estimate of 40-50 km was

given (Macdonald, 1954). The epicenter and depth estimates were noninstrumental. However, a moderate foreshock 11 km away was assigned a depth of 34 km. A magnitude of 6.5 was assigned at Pasadena. Kilauea had been quiet since 1934 but erupted 14 months after the occurrence of this earthquake. To our knowledge, this earthquake and the 1950 Mauna Loa event are the largest events in such close spatial association with the active volcanoes.

August 21, 1951. This earthquake was located along the Kona (western) coast near the Kealakekua fault system. Again, there was no instrumental epicenter or depth information. Most of the aftershocks aligned closely with the surficial expression of the fault. Tsunami activity was reported throughout the Hawaiian Islands (Macdonald and Wentworth, 1951). Gutenberg and Richter (1954) reported magnitude 6.9 and a depth of about 60 km. From the notepads we found that this depth was inferred by adjusting the magnitude determined from the surface waves, M, until it equaled the magnitude determined from the body waves, m, at 6.9. However, a comparison of the isoseismal patterns from this earthquake and the April 1951 Kilauea event clearly indicates that the Kona earthquake was the shallower (Figure 2).

May 23, 1952. This event was very close to the 1951 Kona earthquake, perhaps an aftershock on the Kealakekua fault. HVO reported a depth of about 10 km. The magnitude at Pasadena was 6.0 (*Volcano Letter* 516).

March 30, 1954. The two earthquakes on this date were near the east shore of Hawaii along the east rift zone of Kilauea. HVO reported depths of about 24 km. Magnitudes given by Pasadena were 6.0 and 6.5 (*Volcano Letter* 523). A large eruption began from the east rift zone the following February.

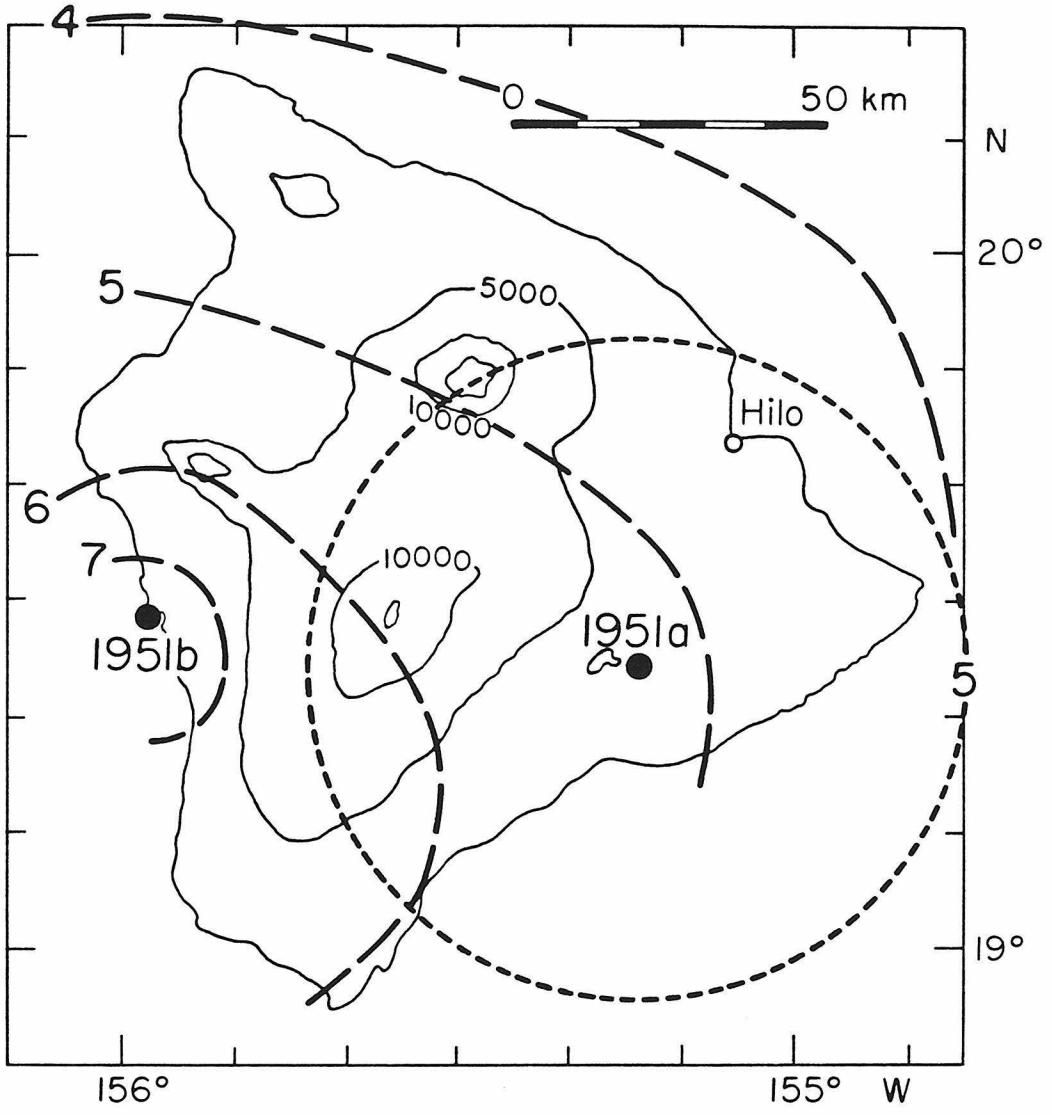

Figure 2. Comparison of isoseismal contours from the April, 1951 Kilauea earthquake (1951a) and the August, 1951 Kona earthquake (1951b). Intensities from the Kilauea earthquake were uniform for a radius of 50 km, suggesting a large depth, estimated at 40-50 km. Contours from the Kona event fall off more rapidly with distance from the epicenter, indicating a shallower depth. (Isoseismal contours for the Kona earthquake were redrawn from Macdonald and Wentworth, 1951.)

June 28, 1962. Each of the earthquakes after 1960 was the subject of one or more studies. The June 28, 1962 event was among the smallest considered in this study ($M_S \sim 5\ 3/4$, assigned at Berkeley). It was included because of its location near the recent earthquake in November 1983; both were located in the Kaoiki zone of the east flank of Mauna Loa. The depth was well constrained at 8.1 km (Koyanagi et al., 1966).

April 26, 1973. This earthquake, $M_S = 6.1$, was located off the northeast shore of Hawaii, away from most of the island's seismic activity. Detailed studies involving crustal velocity structures and station corrections, and intricate body wave modeling, gave this event depths of 48 ± 7 km and 42 km, respectively (Unger and Ward, 1979; Butler, 1982). This is the only large deep event to have occurred since local instrumentation was installed in the late 1950's.

November 29, 1975 (the Kalapana earthquake). This event had the largest instrumental magnitude to date of all Hawaiian earthquakes ($M_S = 7.1$). The Kalapana earthquake and its magnitude 5.2 foreshock had depths of about 10 km (Ando, 1979; Crosson and Endo, 1981). The earthquake occurred on the south flank of Kilauea along the Hilina fault system and involved a large crustal subsidence over the area between Kilauea's summit and the coast (Tilling et al., 1976). It also caused large tsunamis in the Hawaiian Islands. The mechanism may be interpreted either as a very shallow dipping normal fault or as a large landslide or detachment event, brought on by repeated magma injection into the east rift zone (Ando, 1979; Furumoto and Kovach, 1979; Nakamura, 1980; Eissler and Kanamori, 1985). The March 1954 earthquakes occurred in the same general area.

November 16, 1983. This earthquake, $M_S = 6.6$, was located near Mauna Loa in the Kaoiki zone. Its occurrence raised considerable interest in light of renewed

seismic and inflation activity over several years at Mauna Loa. Mauna Loa had been quiet for many years after the 1950 eruptive phase, until a resurgence in both shallow and deep seismicity in 1974 (Koyanagi et al., 1975). A brief but voluminous eruption occurred in July 1975. Earthquakes continued at a low level until mid-1980, when both shallow and deep seismicity began to rise (Decker et al., 1983). Extension rates also increased, indicating a growing volume of magma in the shallow reservoirs. Mauna Loa subsequently began to erupt on March 25, 1984; this eruption is being compared in size to that of 1950. The preliminary depth assigned to the earthquake was 12 km (Decker and Koyanagi, 1984).

Seismograms from the vertical Benioff short-period ($T_p = 1$ s, $T_g = 0.2$ s, Gain $\sim$ 100,000) and long-period ($T_p = 1$ s, $T_g = 90$ s, Gain $\sim$ 3,000) instruments at Pasadena were available for all 12 earthquakes. For illustrative purposes, we show complete sections of seismograms of four selected earthquakes in Figures 3 and 4: the shallow 1983 Kaoiki event, the August 1951 Kona earthquake, the deep 1973 event, and the May 1950 Mauna Loa earthquake. On the short-period records (Figure 3), the 1983 earthquake has large 8-s Rayleigh waves arriving 11 min after the P wave. Note that the amplitude of the body waves of the 1973 event is the same as for the 1983 earthquake, but the 8-s surface waves are only one tenth as large. The surface wave amplitude from the 1951 Kona earthquake is intermediate to the 1983 and 1973 events. Although the P wave from the 1950 Mauna Loa event is comparable in size to the Kona event (about one half as large), its Rayleigh waves are at noise level.

The long-period 1-90 records in Figure 4 show a similar pattern. The largest signal from the 1983 event is the 8 to 10-s Rayleigh wave train, which arrives between 11 and 12 min after the P wave and then goes offscale. The 8-s waves are also the largest-amplitude signal for the 1951 Kona earthquake. However, this wave period is

entirely suppressed in the 1973 record; instead, there is a distinctive train of Rayleigh waves with a period of about 20 s, arriving 9 min after the P wave. On close inspection, some 20-s energy can be seen at about 9 min for the 1983 and 1951 events, but it is clearly enhanced for the 1973 earthquake. Note that, as on the short-period records, the amplitudes of the body waves of the 1983 earthquake and the 1973 earthquake are roughly equal. The signal on the 1-90 record of the May 1950 earthquake is very small, but although the body wave is clearly visible, there is no discernible 20-s wave. From these examples, it appears that the excitation of Rayleigh waves in the period range of 8-20 s is sensitive to differences in focal depth of about 50 km or less.

Portions of the short-period seismograms containing the body waves and the 8 to 10-s surface waves for all the study events are reproduced in Figure 5. The large 1975 Kalapana earthquake has high-amplitude surface waves and a body wave nearly as large, although the maximum in the body wave train is about 30 s after the signal onset. The surface waves from the 1954b event are twice as large as its body waves. The foreshock to the Kalapana earthquake, event 1975a, and events 1954a and 1962 all have similar body and surface wave amplitudes. The 1941 record is very different from the others, with a large distinctive body wave but a small Rayleigh wave. The body wave signals on the 1952 and 1951a records are about the size of the 1975a, 1954a, and 1962 group, but the surface waves are significantly smaller; those of the 1951a earthquake are only slightly above noise level. Since Rayleigh wave excitation decreases with source depth, we expect that events with very small surface waves, such as the 1941 earthquake, the 1951a Kilauea earthquake, and the 1950 Mauna Loa earthquake, are deeper than events with large surface waves, such as the 1983 Kaoiki, 1951 Kona, and 1975 Kalapana earthquakes. This observation can be quantified by calculating the excitation of Rayleigh waves as a function of source depth.

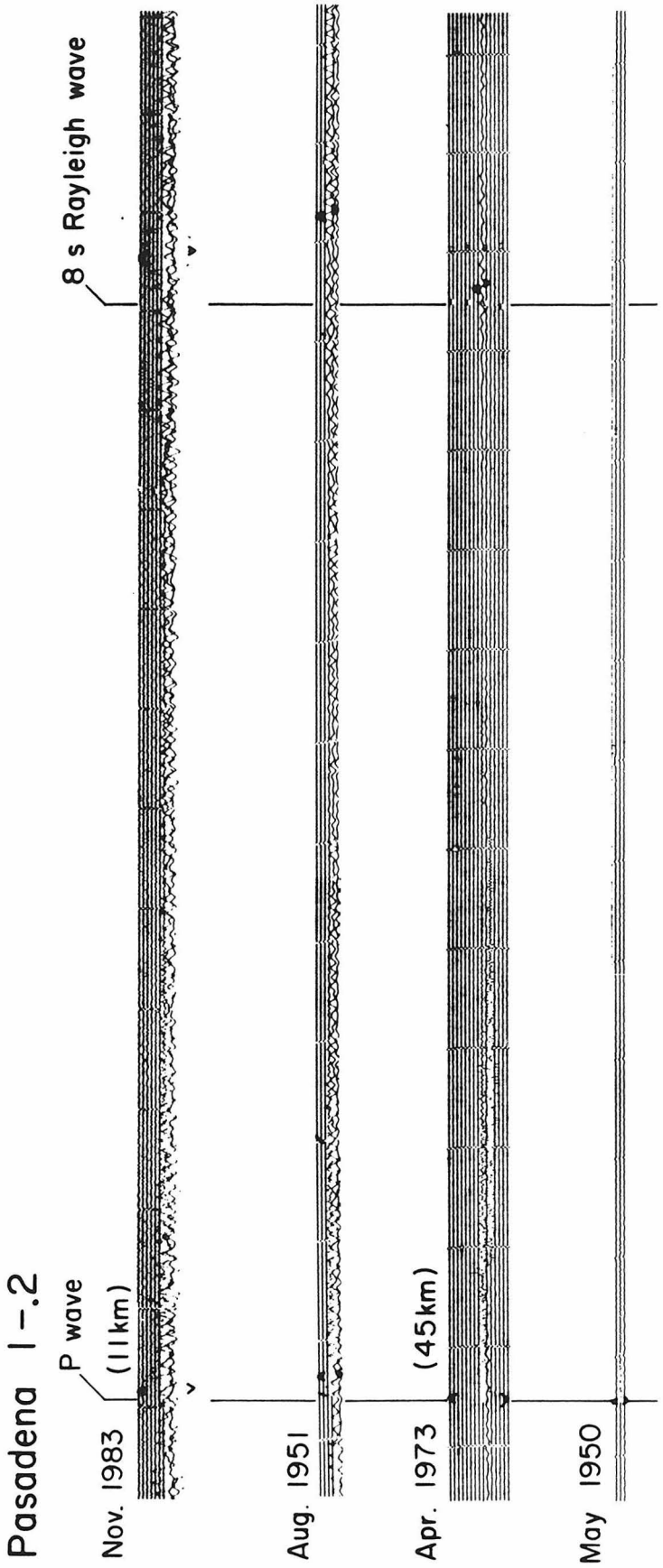

Figure 3. Portions of records of the November 1983 Kaoiki, August 1951 Kona, April 1973, and May 1950 Mauna Loa earthquakes from the short period (1 - .2) vertical instrument at Pasadena. The depths of the 1983 and 1973 earthquakes are known to be 12 km and 45 km, respectively. The body waves of these two events have comparable amplitudes, but the surface waves are much smaller for the deeper earthquake. Note that the P wave of the Mauna Loa event is one half that of the Kona event, but the Rayleigh waves are indiscernable. The width of the records is 15 min; tick marks are one min.

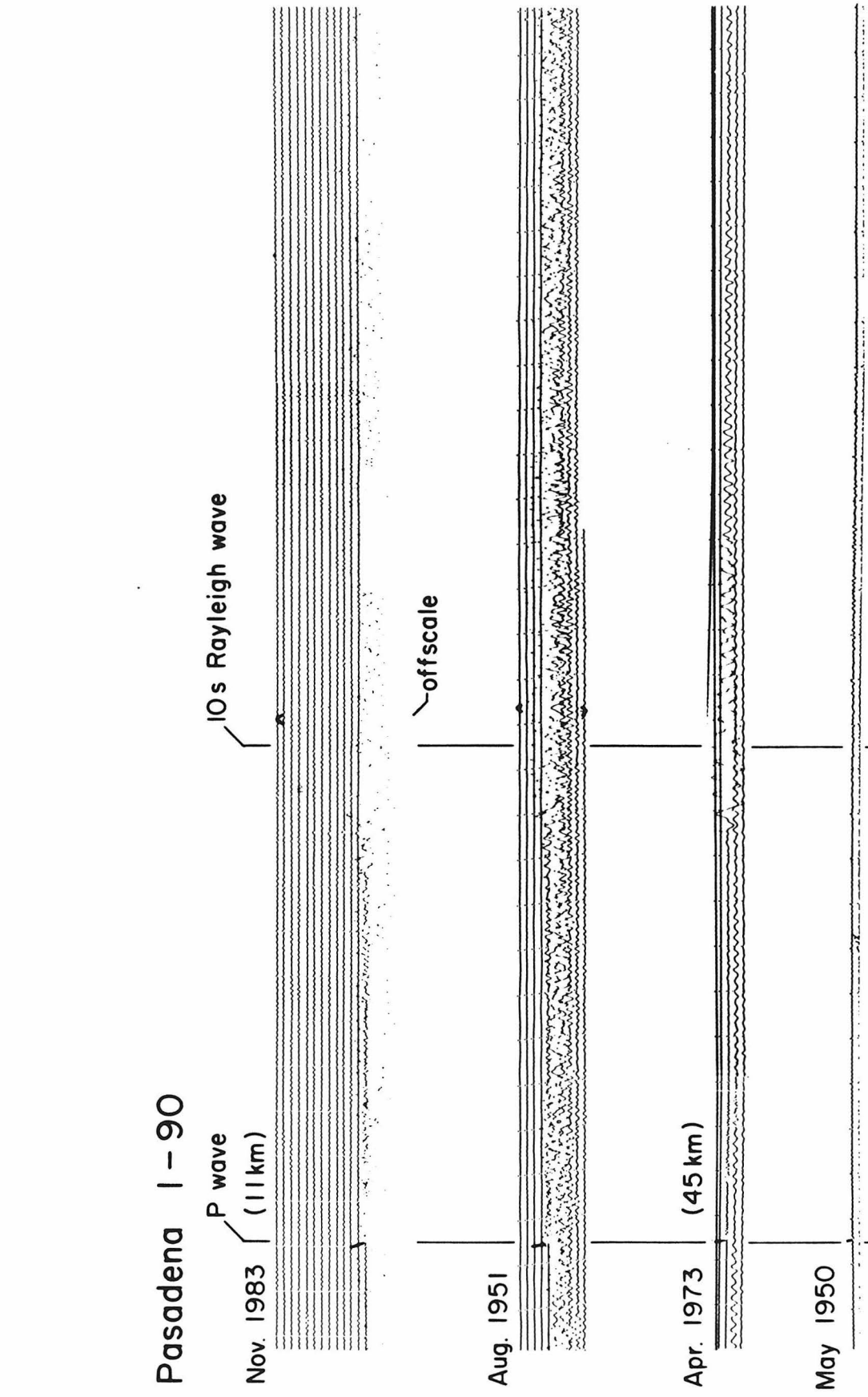

Figure 4. Long-period (1 - 90) vertical seismograms for the same events as in Figure 3. The dominant signal on the 1983 Kaoiki and 1951 Kona records is the 8 s Rayleigh wave, which is suppressed for the 1973 event. Instead, the 1973 record has a strong enhancement of 20 s waves. Smaller 20 s waves with the same group velocity are noticeable in the 1983 and 1951 records. The Mauna Loa record shows no 20 s energy. The width of the records is 30 min; tick marks are one min.

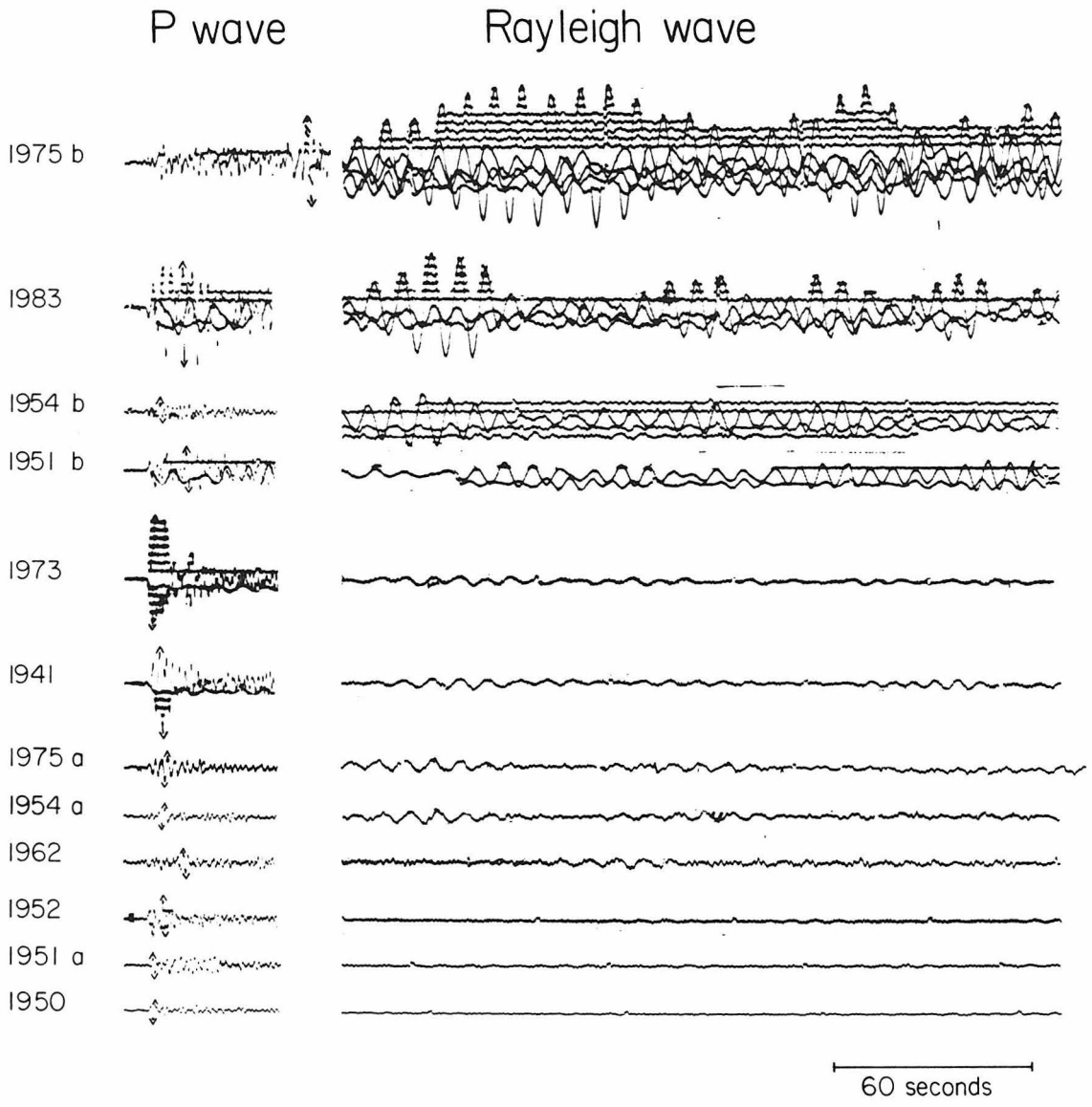

Figure 5. Portions of the short-period records from the 12 study events, showing the P waves and Rayleigh wavetrains. The Rayleigh wave sections begin 11 minutes after the P wave arrival (group velocity $\sim$ 3.7 km s^{-1}). Note the difference between the relative amplitudes of the body and surface waves.

3. Analysis

Surface Wave Excitation Amplitudes

To model the excitation of Rayleigh waves as a function of depth, we computed the eigenfunctions describing the radial and horizontal components of displacement and stress in a nongravitating, spherically layered earth. We follow the method described by Bolt and Dorman (1961). The calculation was done for the two dominant periods in the Rayleigh waves on the Pasadena seismograms, 8 s and 20 s. A composite velocity structure was used, consisting of the model used by HVO in their hypocenter locations above 40 km (Tanigawa et al., 1983), and an average oceanic model below 40 km (Ben-Menahem et al., 1970). This velocity structure has the Moho discontinuity at 15 km. To check the sensitivity to structure, eigenfunctions were calculated for another crustal model of Hawaii with the Moho at 13.5 km (model C of Ward and Gregersen (1973)). The difference in the amplitude of the eigenfunctions was 6% at 8 s and negligible at 20 s. Crustal structure studies on the island of Hawaii show that the depth to Moho varies from about 12 km to about 15 km under the active volcanic centers (Hill, 1969; Crosson and Koyanagi, 1979).

The spectrum of the vertical component of Rayleigh wave motion from a double-couple source is proportional to the "excitation functions" $P_R^{(1)}$, $S_R^{(1)}$, and $Q_R^{(1)}$ as follows:

$$\left(s_R \, S_R{}^{(1)} + p_R \, P_R{}^{(1)} + i q_R \, Q_R{}^{(1)} \right) \tag{1}$$

where the coefficients p_R, s_R, and q_R are simple trigonometric functions of the fault dip, slip, and strike angles (Ben-Menahem et al., 1970). The excitation functions are

simple combinations of the displacement and stress eigenfunctions, as given by Kanamori and Stewart (1976).

Once the excitation functions are determined from the eigenfunctions, it is simple to calculate the excitation amplitude expected for a given fault geometry and source depth. However, for the earthquakes in this study before 1960, focal mechanism information is incomplete or absent. Further, the waves with periods of 20 s and less are likely to suffer severe ray path refractions, so that a precise mechanism may not adequately explain the amplitude variation with azimuth. As an overall calculation, we determined the range of excitation expected from three basic faults: a pure strike-slip fault on a vertical fault plane, a pure dip-slip fault on a vertical fault plane, and a pure dip-slip fault on a fault plane dipping at 45^o. Evaluating the coefficients in (1), the mechanism-dependent part of the spectrum is given by $P_R^{(1)} \sin 2\theta$, $-iQ_R^{(1)} \sin \theta$, and $1/2\ (S_R^{(1)} - P_R^{(1)} \cos 2\theta)$, respectively, for the three faults, where θ denotes the azimuth. To determine a general value for each fault, we take the azimuthal average by integrating the absolute value of the excitation over one cycle of θ. The azimuthally averaged excitation for the three basic faults is then

$$
\begin{array}{lll}
\text{Vertical strike slip} & & \dfrac{2}{\pi} \left| P_R^{(1)} \right| \\
\text{Vertical dip slip} & \left| \overline{Ex} \right| \ \alpha & \dfrac{2}{\pi} \left| Q_R^{(1)} \right| \\
45^o \text{ dip slip} & & \dfrac{1}{2} \left| S_R^{(1)} \right|
\end{array}
\qquad (2)
$$

The averaged excitation amplitudes are plotted as a function of depth for the 8-s and 20-s cases in Figure 6. In the 8-s case the excitation falls off dramatically with depth; amplitudes excited by a source at 50 km are roughly 300 times smaller than those excited by a source at 10 km depth. The effect of the fault geometry on the

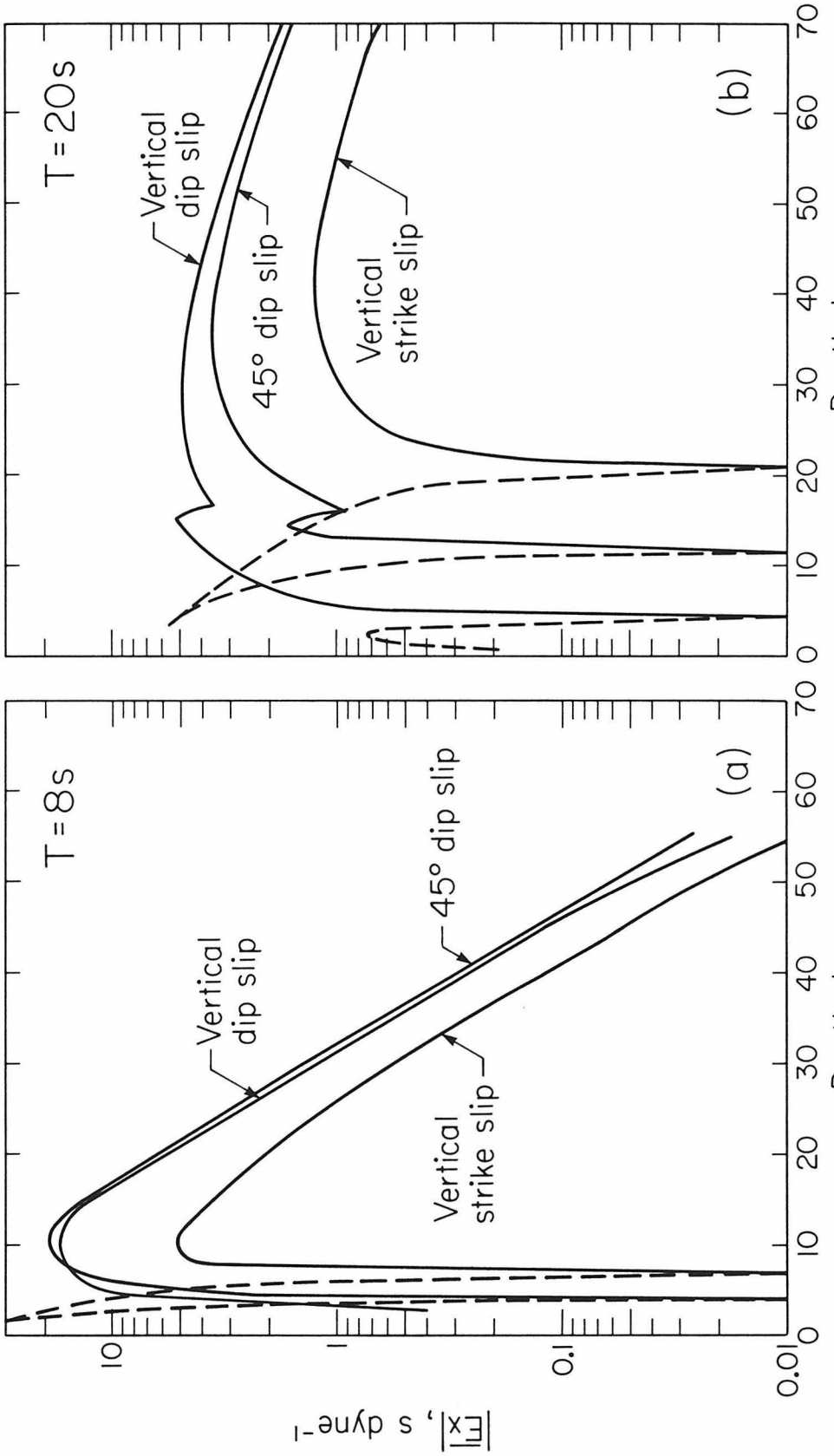

Figure 6. (*a*) Absolute values of amplitudes of the azimuthally averaged excitation of Rayleigh waves vs depth for three basic faults at T = 8 s; dashes indicate negative values. Depth variation, not fault geometry, has the most severe effect on excitation. (*b*) Excitation vs depth at T = 20 s. Excitation is less sensitive to depth at this period, but fault geometry can have a severe effect at certain depths where the functions cross zero.

excitation is much smaller; at 10 km depth the maximum amplitude difference between the azimuthally averaged faults is a factor of 4. Above about 8 km, the functions vary rapidly and are very sensitive to any change in the shallow crustal structure. We judge that the calculation is not accurate for extremely shallow depths. The excitation was calculated for a unit seismic moment of 1 x 10^{27} dyne cm.

At 20 s the excitation varies much more slowly with the source depth (Figure 6*b*). Unlike the 8-s case, the effect of focal mechanism on the excitation amplitude is severe at lower crustal and shallow mantle depths, where the functions $P_R^{(1)}$ and $S_R^{(1)}$ have zero crossings whose locations are fairly stable with respect to changes in the velocity structure. For example, it is possible for a pure vertical dip-slip fault at 20 km depth to have large 20-s excitation, whereas a pure vertical strike-slip fault would have virtually none. Since most fault geometries have components of each of the basic faults, 20-s excitation will be small for some events above 25 km. The excitation for all three faults reaches a broad maximum between depths of 30 and 45 km and decays only by a factor of 2-3 by 70 km. The expected maximum fits well with the records shown in Figure 4, where the 1973 earthquake ($h \sim 45$ km) had a relative enhancement of 20-s energy. Tréhu et al. (1981) calculate excitation functions at selected source depths and $T = 20$ s for an oceanic structure with the Moho at 9 km. The agreement in overall character of the two sets of functions, in terms of location of maxima, shape of fall-off, and relative amplitudes, is quite good.

Effect of Body Waves

To describe the body wave amplitudes, synthetic P wave seismograms for the three basic faults were computed for a near-surface focus, following the method in

Kanamori and Stewart (1976). We include the contribution from the direct P wave and the surface reflections pP and sP for a half-space and apply the 1-0.2 instrument response. Once again, the average value of the azimuthal radiation pattern was used. For the vertical strike-slip fault and the vertical dip-slip fault, the azimuthal dependence is sin 2θ and sin θ, respectively. For the 45^o dip-slip fault, the azimuthal pattern is a function of takeoff angle and can be evaluated and averaged for the appropriate Hawaii-Pasadena value (31^o). The range in the azimuthally averaged body wave amplitudes for these three fault geometries is between a factor of 2-3.

Theoretically, for a given seismic moment, body wave amplitudes diminish somewhat with source depth as velocity increases. In assigning magnitudes from body waves, Gutenberg devised empirical charts to describe this effect (Richter, 1958, Appendix 8). We use these to modify the surface-focus amplitudes for various source depths. This is a small effect; at 60 km depth the amplitude is about 0.6 times the surface value. Since the interference pattern between the direct and reflected rays changes with depth, it can also have a small effect on the amplitude; however we chose to ignore this factor.

Excitation Ratios

We define the excitation ratio as the azimuthally averaged peak-to-peak synthetic body wave amplitude, A_b, divided by the absolute value of the azimuthally averaged surface-wave excitation, $|\overline{Ex}|$, both for the same basic fault. The ratios are controlled by the fall-off of the surface wave excitation, although the body wave fall-off has a slight effect. Both the A_b and $|\overline{Ex}|$ calculations are scaled to the same unit seismic moment, so that taking the ratio eliminates the moment and allows

direct comparison of ratios between the study events. It should be noted that the surface wave excitation $|\overline{Ex}|$ is calculated at the source location and does not include the effects of propagation, attenuation, or instrument. However, since the path and instrument are common to all events, the difference between $|A_b/\overline{Ex}|$ and the measured ratio A_b/A_s will be a constant correction factor, which can be found by comparing the observed and calculated ratios of the earthquakes with well-determined hypocenters.

The calculated ratios versus depth are shown in Figure 7. For the 8-s case the ratio at 50 km is about 200 times larger than at 10 km. The values above 10 km should be disregarded as before. For the 20-s case the effect of focal mechanism is larger than the effect of depth between 30 and 70 km. The 20-s observations will not be as diagnostic of depth as the 8-s observations, due to both the local, mechanism-dependent singularities at 10-25 km, and the rather slight increase of the excitation ratios over the depth range of interest for Hawaiian earthquakes.

Excitation Ratios for Events With Known Focal Mechanisms

The five events since 1960 have known focal mechanisms from either the HVO network or teleseismic studies. The mechanisms are shown in Figure 8. Exact theoretical values of $|Ex|$ and A_b, without azimuthal averaging, were evaluated for these specific mechanisms. $|Ex|$ is now defined as the modulus of equation (1), evaluated for the correct trigonometric coefficients p_R, s_R, and q_R. Figure 9 shows the values of $|Ex|$ and $|A_b/Ex|$. The band defined previously by the three basic faults is indicated by heavy dashed lines. For the 1962 and 1973 mechanisms, the surface wave excitation $|Ex|$ falls within the band of the three basic faults, and for the 1975a,

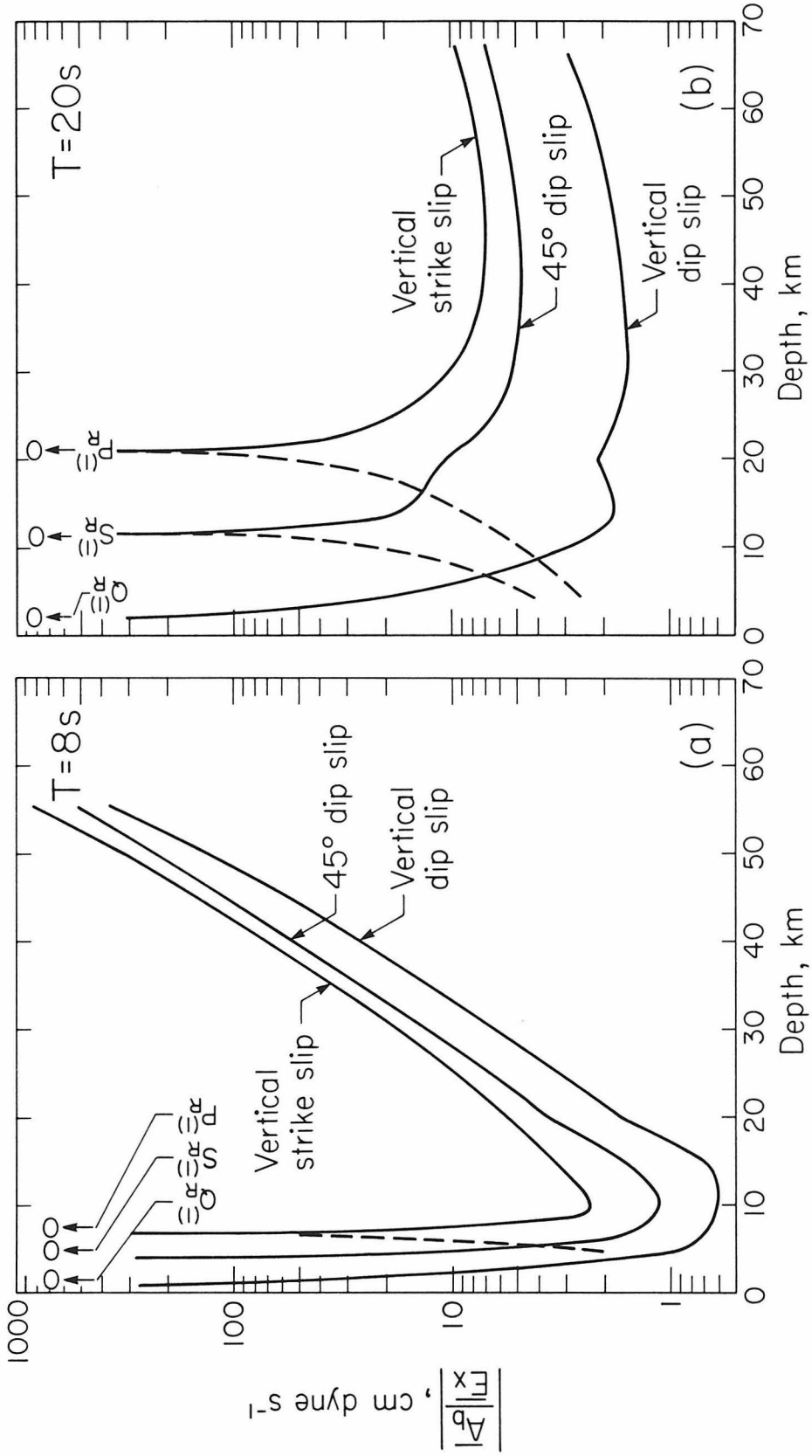

Figure 7. (*a*) Absolute values of the azimuthally averaged excitation ratios vs source depth, for the three basic faults at T = 8 s. (Values above 8 km should be disregarded.) The ratios steadily increase by factor of 200 from 10 to 70 km. (*b*) Excitation ratios vs source depth at 20 s. Note that ratios may become large for some fault geometries at lower-crustal and shallow-mantle source depths.

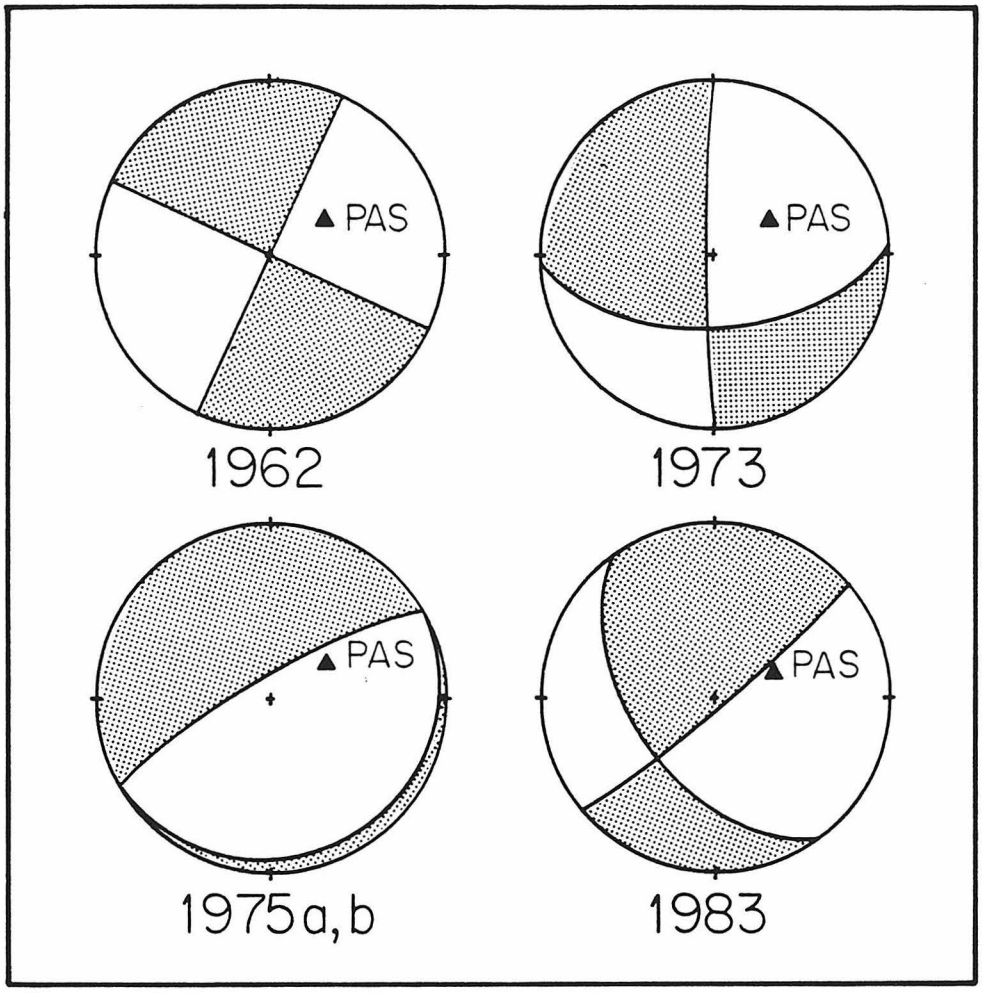

Figure 8. Focal mechanisms for the five post-1960 events. The location of Pasadena on the focal sphere is indicated by a triangle. Mechanisms are from the following sources: 1962, Koyanagi et al., 1966; 1973, Butler, 1979; 1975a and b, Ando, 1979; 1983, Decker and Koyanagi, 1984.

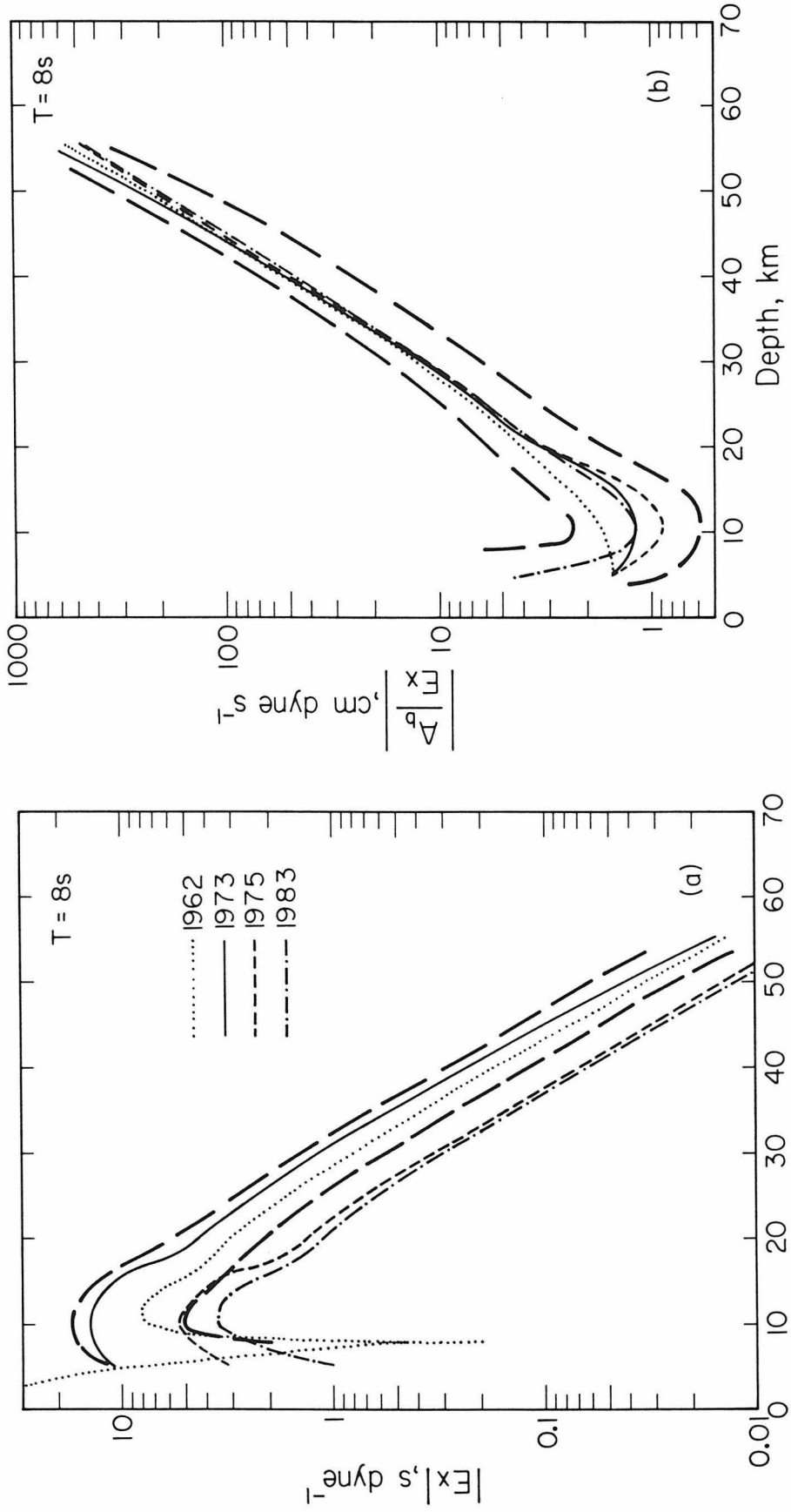

Figure 9. (*a*) Modulus of the calculated 8 second surface wave excitation amplitude Ex, as a function of source depth, evaluated for the five events with known focal mechanisms (events 1975a and b had the same mechanism). The heavy, long dashed lines indicate the range of azimuthally averaged excitation amplitudes for the three basic faults. (*b*) Excitation ratios vs source depth, where both A_b and Ex have been evaluated for the known mechanisms. Note that the ratios fall within the range defined by the three basic faults.

1975b, and 1983 mechanisms, $|Ex|$ is slightly below the band (Figure 9*a*). However, Pasadena is located essentially in the nodal azimuth for these two mechanisms, causing the low values (Figure 8). When the theoretical A_b is considered, the excitation ratios $|A_b/Ex|$ for all five events fall within the basic fault band, even though Pasadena is near-nodal for two of the mechanisms (Figure 9*b*). Thus the ranges of $|\overline{Ex}|$ and A_b found by the general fault calculations provide reasonable estimates of the theoretical excitation for various fault geometries. Again, we point out that the azimuthally averaged general calculations may be more realistic due to the scattering of short-period waves.

Depth Estimates

The peak-to-peak amplitudes in millimeters of the observed records are listed in Table 2. Both the A_b and A_s values were measured from the shorter-period 1-0.2 instrument for comparison with the calculations. Surface wave information at 20 s on the 1-90 records was incomplete; energy was absent for some events, and the periods of identifiable signals ranged from 16 to 24 s. On the short-period instrument the maximum surface wave energy was always between periods of 8 and 10 s. The observed body wave amplitudes of the earthquakes are plotted versus the observed surface wave amplitudes in Figure 10. The bands indicate where the excitation ratio ranges for various source depths, as calculated above, would fall on this plot. The correction to the calculated ratios, 0.36, was determined by forcing the 1973 and 1983 earthquakes to fall near the 45-km and 10-km depth bands, respectively. For the most part, the earthquakes correspond to depth bands in the way expected from qualitative examination of the character of the body and surface waves. The 1983 Kaoiki

Table 2

Peak-to-Peak Amplitudes of Body and Surface Waves on the Short-Period (1-0.2) and Long-Period (1-90) Instruments

Event	A_b (1-0.2), mm $T\sim1$ s	A_s (1-0.2), mm $T\sim8$ s	A_s (1-90), mm $T\sim10$ s	$T\sim20$ s	$m_{b\,(PAS)}$	$M_{S\,(PAS)}$*
1941	25	3	15	2	6.6	(6.0)
1950	5	<0.5	3	~1	5.9	(5.2)
1951a	5	<1	3	~1	5.8	(5.4)
1951b	11	7	41	16	6.4	6.4
1952	10	1	3	~2	5.9	(5.4)
1954a	5	4	14	~1	6.0	6.0
1954b	5	15	62	~5	5.8	6.6
1962	6	3	8	~1	5.7	5.8
1973	32	3	--	20	6.3	(5.9)
1975a	8	4	13	~1	6.0	6.0
1975b	25	43	offscale	17	6.7	7.1
1983	28	31	offscale	20	6.6	6.9

*Parentheses indicate a known or suspected deep hypocenter.

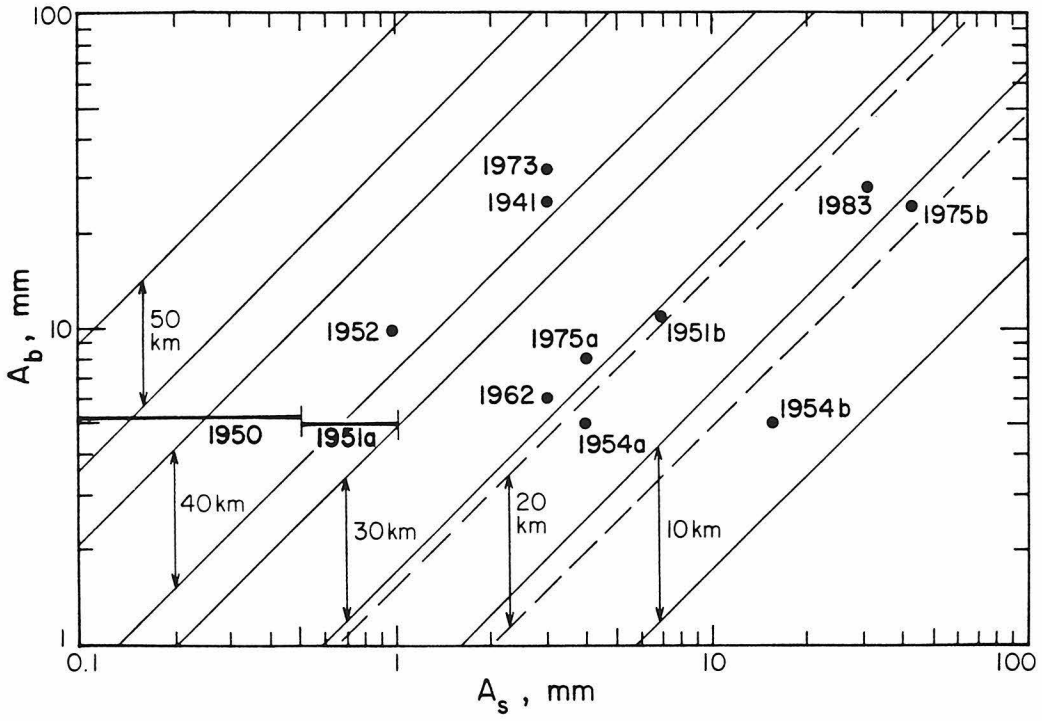

Figure 10. Observed body-wave amplitudes plotted vs observed surface-wave amplitudes for the 12 study events. Bars for the 1950 and 1951a events indicate estimates of very small amplitudes. The bands show where the ranges of the calculated ratios for various source depths fall on this plot.

and 1975 Kalapana earthquakes have crustal depths, as does the larger of the two events near Kalapana in 1954. The 1962 Kaoiki, 1951 Kona, and the foreshocks to the 1954 and 1975 Kalapana events group near a somewhat greater depth, about 25-30 km. Figure 10 suggests a depth gap between the under 30 km depth bands and the rest of the earthquakes. The 1952 and 1941 events fall in the same band as the deep 1973 earthquake, around 45 km. The two events near the volcanic centers, 1950 and 1951a, have estimated depths of $>$40 km and $>$35 km, respectively; the range in A_s values is due to uncertainty in the measurement of very small amplitudes.

For three out of the five instrumentally located events, our estimated depth agrees well with the instrumental depth. For the remaining two events, however, our estimates are about 3 times larger. As Table 1 shows, these two events (the June 1962 Kaoiki earthquake, M_S = 5 3/4, and the November 1975 Kalapana foreshock, M_S = 5.1) have the smallest magnitudes (less than 6). The depth discrepancy can be explained in terms of the difference in the source spectrum. For an earthquake with M_S = 6, empirical relations (e.g., Kanamori, 1977) give a source dimension of 5.7 km (radius of an equivalent circular fault) and a corner frequency of 0.23 Hz (corner period of about 4 s) through Brune's (1970) relation. Our depth estimates are based on the amplitude of "1-s" body waves and "8-s" surface waves. Hence for earthquakes with M_S significantly smaller than 6, the corner period moves toward the body wave period, increasing the ratio of the body wave to surface wave amplitude. This causes an overestimate of depth. Except for these two events, the earthquakes listed in Table 1 are large enough to avoid overestimation.

A few of the preinstrumental depths reported from other sources are in disagreement with the depth estimates. For example, the estimate for the 1951 Kona earthquake is shallow compared with that given by Gutenberg and Richter (1954).

However, a shallow depth is more consistent with the tsunami activity, and the earthquake's association with the Kealakekua fault. The 1941 earthquake appears deep by our method, but the HVO gave it a depth of 11 km; however, the accuracy of an instrumental depth in that era is dubious. Some aftershocks to the 1941 event were given depths of 30 km.

Single Station Versus Global M_S

An indication of the reliability of using surface wave amplitudes from a single station, i.e., Pasadena, can be obtained by comparing M_S values derived from the Pasadena amplitudes alone to those based on many measurements worldwide. Body and surface wave magnitudes determined for the 12 events from the amplitudes on the 1-0.2 and 1-90 seismograms are listed in the last columns of Table 2. The formulas used are

$$m_b = \log(\frac{A}{T}) + Q(\Delta) \tag{3}$$

$$M_S = \log(\frac{A}{T}) + 1.66 \log \Delta + 3.3 \tag{4}$$

where A is the maximum ground amplitude in microns for either the P wave train or the surface wave, T is the period of the maximum in seconds, $\Delta = 36^o$ for Hawaii to Pasadena, and $Q(\Delta) = 6.6$. Equation (4), from Vanek et al. (1962) was used instead of Gutenberg's standard formula because it includes a correction using T for shorter-period surface waves. The values determined from the two instruments were averaged. The M_S values in parentheses are for the earthquakes with a known or suspected deep hypocenter; we did not attempt to correct for depth. For the recent events, the m_b and M_S values agree fairly well with those reported by the National

--

Earthquake Information Service (NEIS) (Table 1), implying that these one-station magnitudes may be representative for the pre-1960 events as well. Note from the m_b values that the two deep earthquakes under the volcanoes may have been smaller than previously reported (6.0 and 5.8 instead of 6 1/4 and 6 1/2). The m_b and M_S for the Kona earthquake (1951b) agreed at 6.4 without a depth correction.

Figure 11 shows a comparison of M_S values based on ground amplitudes at Pasadena with those assigned by NEIS from global readings, for a sample of 70 events in 1973-1974. On the average, the global values are only slightly larger (0.05 of a magnitude unit), and the standard deviation is 0.2 magnitude units. The overall agreement between M_S and $M_{S_{(PAS)}}$ indicates that the Pasadena amplitudes are representative of the global values. This was an implicit assumption in the depth estimates. Even the extreme difference of 0.4 magnitude units between the Pasadena and global magnitudes, implying a surface wave amplitude difference of 2.5, would change the depth estimates by only 10 km (see Figure 8).

Mechanism Dependence of Global m_b

An estimate of the effect of focal mechanism on amplitudes can be found by comparing the m_b-M_S ratios for earthquakes with known focal mechanisms. Body wave amplitudes, and thus m_b, are expected to be much smaller for strike-slip events than for dip-slip events because of the proximity of the ray path direction to the nodal planes. Centroid moment tensor solutions have been routinely determined for most events worldwide with $M_S \geq 5.0$ since 1977 (e.g., Dziewonski et al., 1985) (hereafter referred to as the Harvard catalog). We searched the Harvard catalog, from 1977 to December 1983 for strike-slip and dip-slip events in two depth ranges 0-20 km

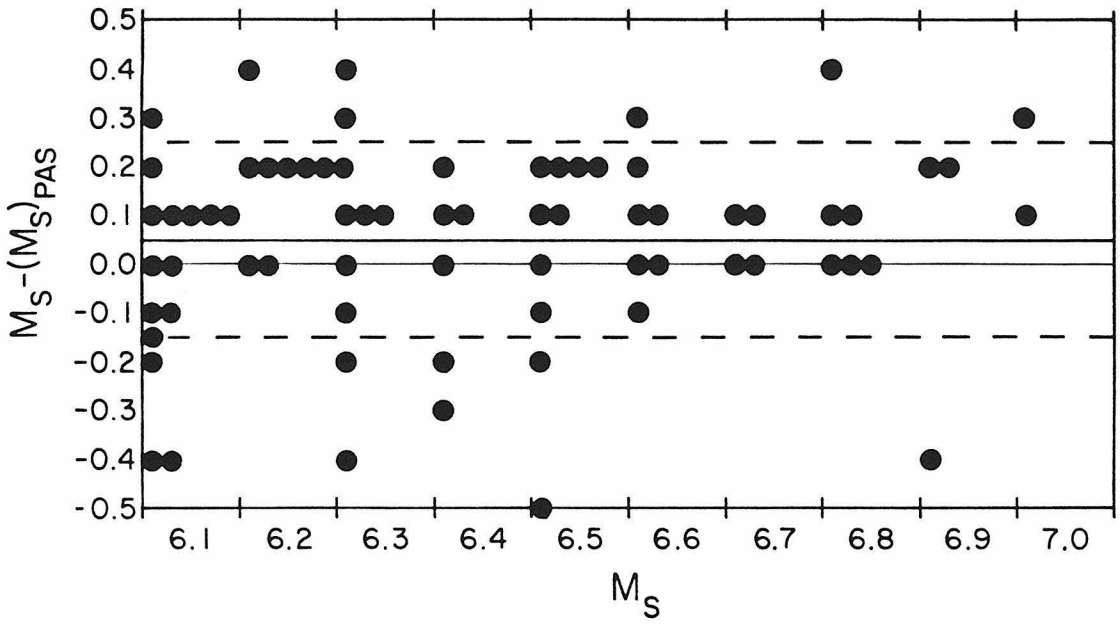

Figure 11. Comparison between values of M_s assigned from many stations, with values assigned from ground amplitude at Pasadena only. The difference between M_s and $M_{s\,(PAS)}$ is plotted vs M_s. The average difference is .05 units, shown by the heavy solid line; the standard deviation is .2 units, shown by the dashed lines.

and 20-40 km, where the depths were taken from the centroid hypocenter. Strike-slip events were defined as having a fault plane dip δ within 10^o of vertical, and a slip angle λ within 10^o of right-lateral or left-lateral (i.e., $\lambda = 0^o \pm 10^o$ or $180^o \pm 10^o$). Dip-slip events were defined as having fault plane dip δ between 25^o and 60^o and slip angle λ within 10^o of thrust or normal ($\lambda = 90^o \pm 10^o$ or $-90^o \pm 10^o$). Figure 12 shows plots of m_b versus M_S for these mechanism groups in the two depth ranges, with a least squares line fit to the distributions. Although widely scattered, there is a marked difference between the m_b-M_S relation for dip-slip and strike-slip events. For events between depths of 0 and 20 km, m_b is 0.31 magnitude units larger for dip-slip events than for strike-slip events at $M_S = 6.0$ (Figures 12*a* and 12*b*). This is equivalent to a factor of 2.1 in amplitude. Between 20 and 40 km, the m_b difference at $M_S = 6.0$ has reduced to 0.12 magnitude units, or an amplitude factor of 1.3 (Figures 12*c* and 12*d*). Recall that the range in the azimuthally averaged, synthetic body wave calculation for the three basic faults was a factor of 2-3. If the mechanism dependence of m_b found in the Harvard catalog is considered in the depth estimates, the largest factor (2.1) would change the estimates by less than 10 km. Note that a factor of 2 is about the size of the bands defined by the azimuthally averaged basic fault calculations (Figure 10).

Thus two different effects have been examined in the last two Sections using global data: (1) the accuracy of using a single station as representative of the surface wave amplitude at short periods, and (2) the mechanism dependence of observed body wave amplitudes. Both tests give an average range in amplitude of a factor of 2 to 2.5, which is the same range previously estimated by the basic fault calculations.

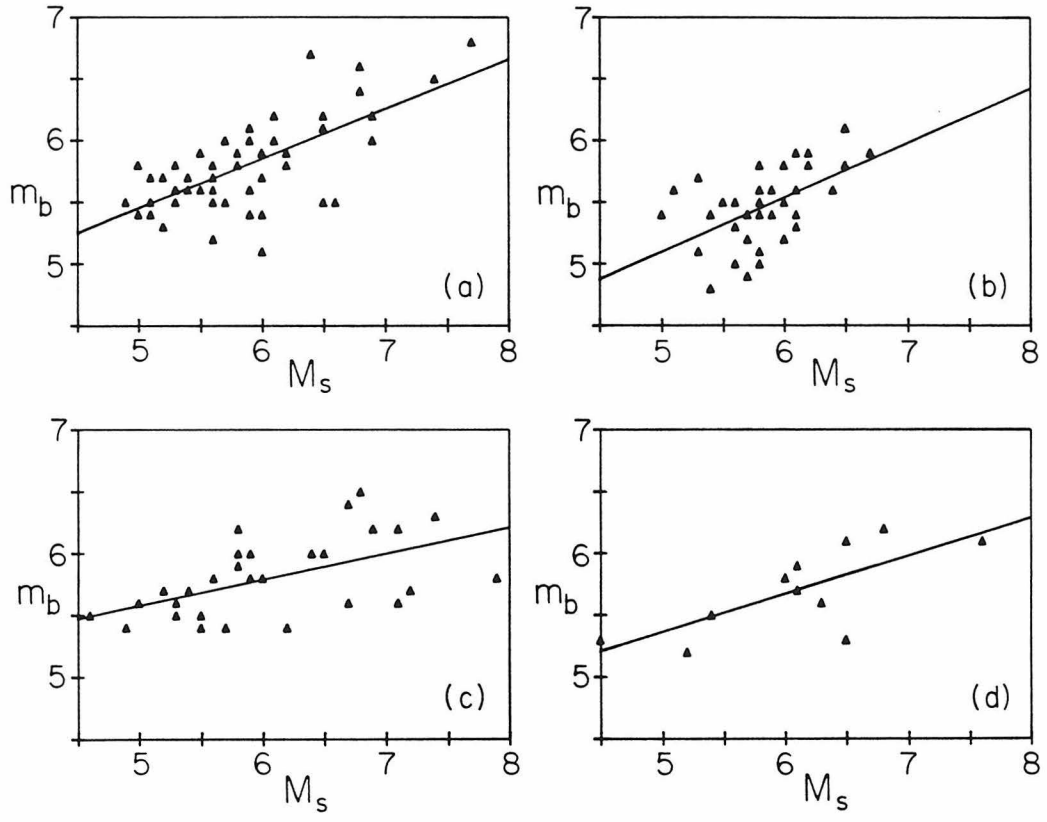

Figure 12. (*a*) m_b vs M_s for all dip-slip events ($n = 53$) with depths between 0 - 20 km found in the Harvard catalog. (*b*) Strike-slip events, $n = 37$, $h = 0$ - 20 km. (*c*) Dip-slip events, $n = 30$, $h = 20$ - 40 km. (*d*) Strike-slip events, $n = 11$, $h = 20$ - 40 km.

4. Discussion

Estimated depths for both the 1951 Kilauea earthquake and the 1950 Mauna Loa earthquake were large ($\geq$ 35 km). The 1950 earthquake was unique among the study events in having undiscernible Rayleigh wave signals on the short-period instrument (Figure 5). Rayleigh waves for the Kilauea earthquake were extremely small. This alone rules out the possibility that the earthquakes were shallow. Note from Figure 5 that if the amplitude of the long-period record of the deep (48 km) 1973 earthquake is reduced by a factor of 2 or 3, to be comparable with the P wave amplitude of the 1950 event, the 20-s Rayleigh waves would still be clear. The lack of 20-s waves for the 1950 earthquake suggests that its depth is well removed from the maximum depth of excitation at 30-45 km. Extrapolating the 20-s excitation (Figure 6), amplitudes an order of magnitude less than those at 40 km would occur at source depths of 90 or 100 km. However, the deepest seismicity reported for Hawaii is at 60 km (Eaton, 1962). Examination of the 1980-1982 HVO catalogs suggests that this limit is actually around 50-55 km for well-located earthquakes. Recent studies have shown that for all oceanic intraplate earthquakes, the maximum depth of seismicity corresponds with the expected location of the 600^o - 800^o C isotherm, beyond which the lithosphere purportedly cannot fail in a brittle mode (Chen and Molnar, 1983; Wiens and Stein, 1983). For Hawaii, this isotherm is put at 55-60 km.

What is the significance that the two events under the volcanic centers and close in time to eruptions have greater depths than most other large earthquakes? Perhaps they have a more fundamental relationship to the eruptive process. Most of Hawaii's large ($M_L \geq 6$) earthquakes are away from the volcanic centers, usually shallow, and frequently involve the flank areas or fault zones. In general, these involve

readjustment of large crustal blocks to stresses caused by the growing load of the volcano or by the influx or outflux of magma at the large crustal reservoirs (Eaton and Murata, 1960). These earthquake can be said to have a secondary relationship to eruptive activity, in that they are events caused by tectonic stresses. The large study events near the flanks of the volcanoes associated with the fault zones are consistent with this model.

Deep seismicity on Hawaii occurs mainly beneath Kilauea and Mauna Loa. Kilauea, in particular, is well-known for intense deep swarms which are frequently related to tilt changes and/or impending eruption. Magnitudes are usually ≤ 3. Deep activity is weaker at Mauna Loa, but seismicity between 35 and 50 km has been observed to increase somewhat before eruptions (Koyanagi et al., 1975; Decker et al., 1983). The cause of the deep activity under the volcanoes is thought to be the entry of magma into the conduit system of the volcano. Intense shallow swarms are observed before and during eruptions at both volcanoes, caused by the opening of cracks as magma breaks to the surface. Both swarm types can be said to have a primary relationship to volcanism; seismic events are directly caused by the movement of magma.

Deep earthquakes with large magnitudes are quite rare. There were only 14 events with $M_L \geq 4$, $h \geq 35$ km from 1965 to 1981 (Figure 13). Except for the large April 1973 study event, all of these were between magnitudes 4 and 5. Note from Figure 10 that only four of these events are spatially related to the volcanic centers. The picture that deep activity is confined to the volcanic centers and that all other seismicity is shallow and associated with fault zones is an oversimplification. Aside from swarms under the summits, subcrustal activity is relatively uniform beneath Hawaii, and its volcanic association is not well understood. The 1973 earthquake has been

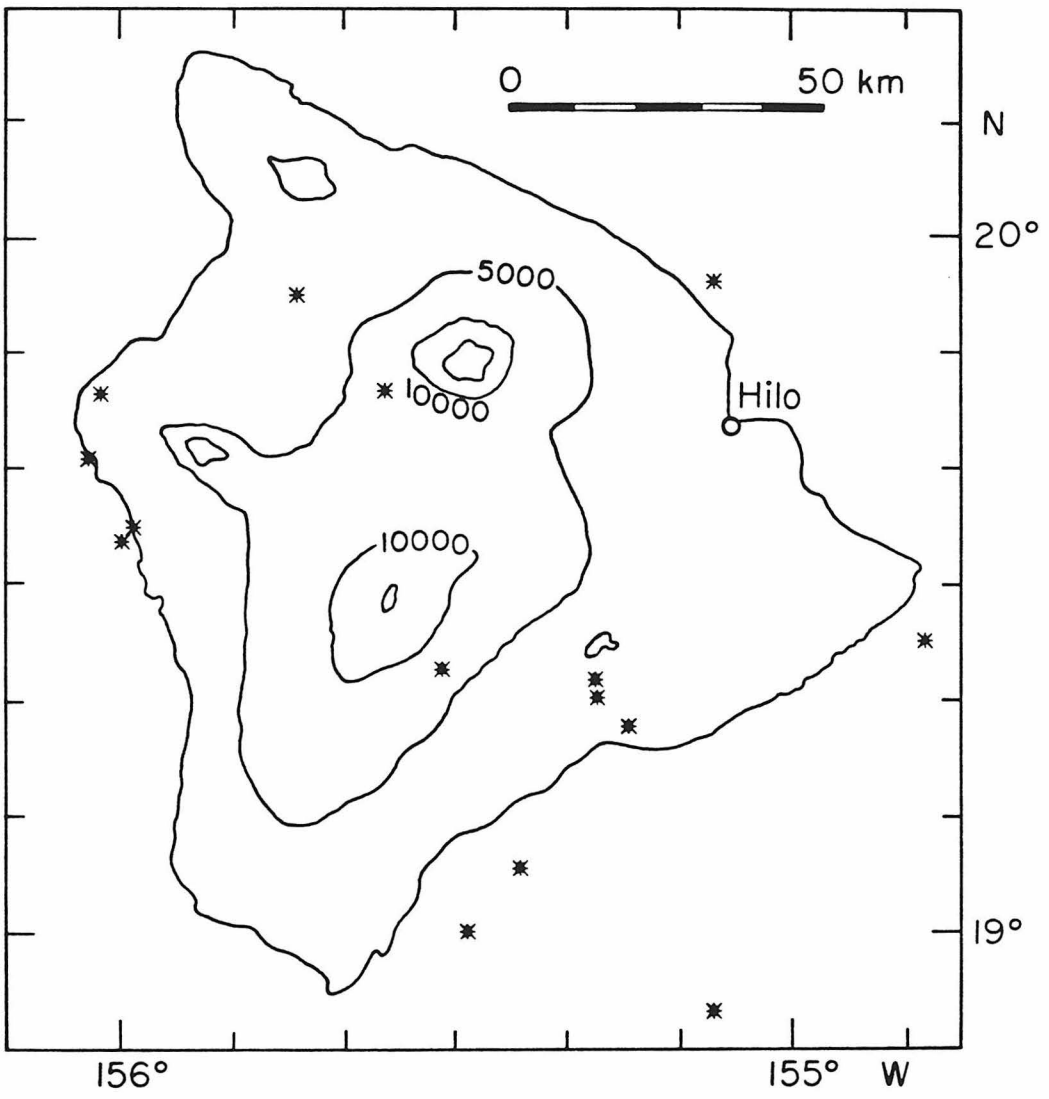

Figure 13. All events with $M_L \geq 4.0$ and deeper than 35 km between 1965 and 1981. Unlike the deep swarms of smaller earthquakes, many events are away from the active volcanoes.

suggested to be due to larger-scale, regional stresses (Unger and Ward, 1979), or a renewal of volcanism under Mauna Kea (Butler, 1982).

The May 30, 1950, deep event under Mauna Loa was clearly associated with the large eruption 3 days later. Likewise, it was suggested that the deep Kilauea earthquake in April 1951 marked a new period of activity for that volcano, which had been quiet since 1934 and which subsequently erupted from its summit in June 1952 (Macdonald, 1959). The specific cause of these earthquakes is unknown. Deep swarms preceding eruptions have been attributed to rock fracturing from magmatic pressure. Although their magnitudes are much larger than those of the swarm events, the temporal relationship of these two events to ensuing eruptive activity suggests that they too signify the motion of magma.

Figure 14 shows a histogram of eruptions with volumes of lava 10^6 m^3 since 1934. Large earthquakes are indicated by a circle. Macdonald (1959) regarded the two events near Kalapana in March 1954 as precursors to the eruption in early 1955, when Kilauea's east rift zone was active along most of its length. Our depth estimates for these events were shallow (20-25 km and $\sim$ 10 km). The 1975 Kalapana earthquake, in the same general area, may have been triggered by a sudden increase in the volume of magma stored in Kilauea's east rift zone (Furumoto and Kovach, 1979). Kilauea had become active in 1952, after a quiet period of 16 years. There were subsequent eruptions in May 1954 and February 1955. Thus it is possible that the March 1954 events were related to a sudden magma increase in the east rift zone reservoir, analogous to the case of the 1975 earthquake. Correlation between other study events and eruptive activity is less obvious. Aside from the cluster of both large earthquakes and eruptions from 1949 to 1955, there is no clear association.

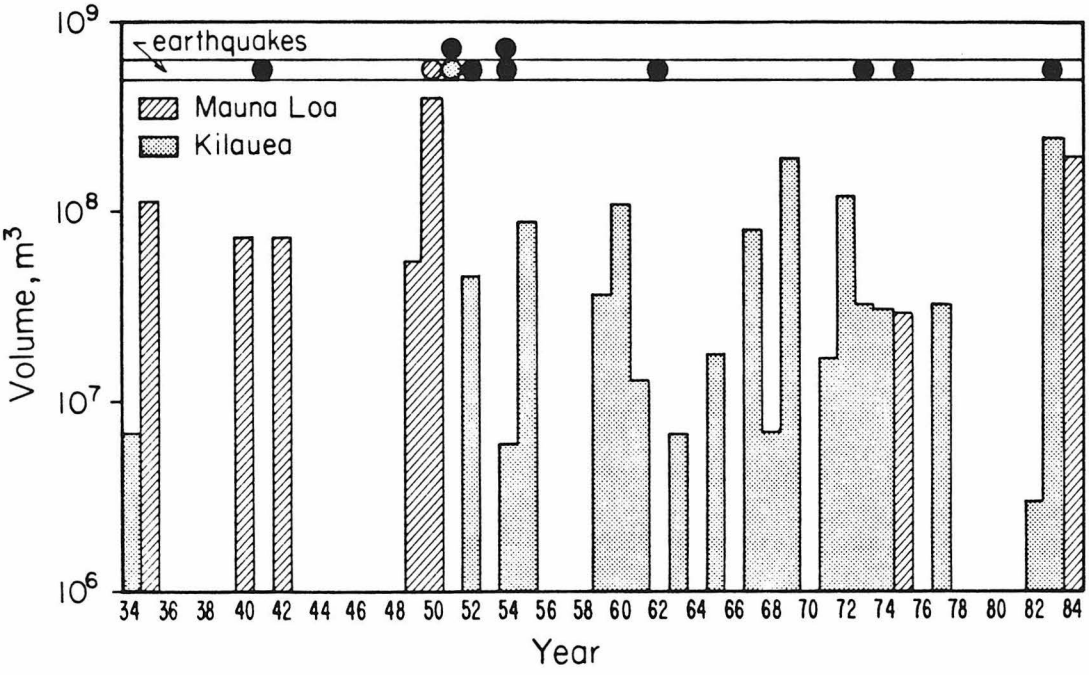

Figure 14. Histogram of eruptions with lava volumes over 10^6 m^3 of Mauna Loa (stipled) and Kilauea (hachured) since 1934. The entire volume is plotted in the year the eruption began. Earthquakes discussed in this study are plotted above as filled circles; the shaded circles indicate the events underneath the volcanic summits. (Eruption volumes from Macdonald et al., 1983; except for the two most recent eruptions of Kilauea and Mauna Loa, from Koyanagi, pers. comm.)

5. Conclusions

Depths estimated for 12 moderate to large Hawaiian earthquakes from the relative excitation of body and surface waves are reasonably consistent with well-determined depths from local data. Further, the results agree with known Hawaiian seismicity patterns. The technique is useful for events before 1960, when instrumental depths were determined only rarely. The results are limited in that we used records from one station only; we attempted to correct for this by doing a general calculation of excitation for the three basic faults and taking the average of the azimuthal radiation pattern. Independent checks with global data were done to determine (1) the reliability of using one station as representative of the surface wave amplitude, and (2) the mechanism dependence of body wave amplitudes. Results suggest that depth estimates made from A_b and A_s observations at one station have an average accuracy of about 10 km. This is roughly equal to the range of the azimuthally averaged, basic fault calculation. Use of whole spectra would yield more precise results than a single amplitude at one period, but a more complete treatment was not justified due to the lack of data for pre-1960 events.

In general, depth estimates of earthquakes associated with the volcanic flanks or fault and rift zones are shallow ($<$20 km). Exceptions to this are the 1941 and 1952 events. Two earthquakes under the volcanic summits, and close in time to eruptions, show large depths, rare for earthquakes of their magnitude. These were the May 1950 event under Mauna Loa and the April 1951 event under Kilauea, estimated to have depths between 40 and 55 km and 35 and 50 km, respectively. Although the mechanism of these earthquakes is not known, it is possible that they have a more direct relation to magma motion, or increased magmatic pressure, than the large, shallow

earthquakes associated with Hawaii's fault and rift zones.

Acknowledgments. I would like to thank Jim Westphal of the California Institute of Technology for first calling my attention to the 1950 Mauna Loa earthquake. I thank Elliot Endo of the Cascades Volcano Observatory and Robert Koyanagi of the Hawaiian Volcano Observatory for discussion of Hawaiian seismicity and preliminary information on the 1983 Kaoiki earthquake and 1984 eruption of Mauna Loa. I am grateful to Robert P. Sharp and the donors to Caltech's 1985 Project Pahoehoe for the opportunity to see the geology of Hawaii firsthand. This research was supported by the Earth Sciences Section, National Science Foundation, grant EAR-8313223.

References

Ando, M., The Hawaii earthquake of November 29, 1975: Low dip angle faulting due to forceful injection of magma, *J. Geophys. Res., 84*, 7616-7626, 1979.

Ben-Menahem, A., M. Rosenman, and D. G. Harkrider, Fast evaluation of source parameters from isolated surface wave signals, I, Universal tables, *Bull. Seismol. Soc. Am., 60*, 1337-1388, 1970.

Bolt, B. A., and J. Dorman, Phase and group velocities of Rayleigh waves in a spherical, gravitating earth, *J. Geophys. Res., 66*, 2965-2981, 1961.

Brune, J. N., Tectonic stress and the spectra of seismic shear waves from earthquakes, *J. Geophys. Res., 75*, 4997-5009, 1970.

Butler, R., The 1973 Hawaii earthquake: A double earthquake beneath the volcano Mauna Kea, *Geophys. J. Roy. Astr. Soc., 69*, 173-186, 1982.

Chen, W., and P. Molnar, Focal depths of intracontinental and intraplate earthquakes and their implications for the thermal and mechanical properties of the lithosphere, *J. Geophys. Res., 88*, 4183-4214, 1983.

Crosson, R. S., and E. T. Endo, Focal mechanisms of earthquakes related to the 29 November 1975 Kalapana, Hawaii earthquake: The effect of structural models, *Bull.*

Seismol. Soc. Am., 71, 713-729, 1981.

Crosson, R. S., and R. Y. Koyanagi, Seismic velocity structure below the island of Hawaii from local earthquake data, *J. Geophys. Res., 84*, 2331-2341, 1979.

Decker, R. W., and R. Koyanagi, Hawaiian earthquake of November 16, 1983, *Earthquake Inf. Bull., 16*, 4-9, 1984.

Decker, R. W., R. Y. Koyanagi, J. J. Dvorak, J. P. Lockwood, A. T. Okamura, K. M. Yamashita, and W. R. Tanigawa, Seismicity and surface deformation of Mauna Loa volcano, Hawaii, *Eos Trans. AGU, 64*, 545-547, 1983.

Dziewonski, A. M., J. E. Franzen, and J. H. Woodhouse, Centroid moment tensor solutions for July-September 1984, *Phys. Earth Planet. Inter., 38*, 203-213, 1985.

Eaton, J. P., Crustal structure and volcanism in Hawaii, in *The Crust of the Pacific Basin, Geophys. Monogr. Ser.*, vol. 6, edited by G. A. Macdonald and H. Kuno, pp. 13-29, AGU, Washington, D. C., 1962.

Eaton, J. P., and K. J. Murata, How volcanoes grow, *Science, 132*, 925-938, 1960.

Eissler, H. K., and H. Kanamori, A single-force source model for the 1975 Kalapana, Hawaii earthquake (abstract), *Eos Trans. AGU, 66*, 307, 1985.

Furumoto, A. S., and R. L. Kovach, The Kalapana earthquake of November 29, 1975: An intra-plate earthquake and its relation to geothermal processes, *Phys. Earth Planet. Inter., 18*, 197-208, 1979.

Geller, R. J., and H. Kanamori, Magnitudes of great shallow earthquakes from 1904 to 1952, *Bull. Seismol. Soc. Am., 67*, 587-598, 1977.

Goodstein, J. R., H. Kanamori, and W. H. K. Lee, Seismicity microfiche publications from the Caltech Archives (announcements), *Bull. Seismol. Soc. Am., 70*, 657-658, 1980.

Gutenberg, B., and C. F. Richter, *Seismicity of the Earth and Associated Phenomena,* Princeton University Press, Princeton, N. J., 1954.

Hill, D. P., Crustal structure of the island of Hawaii from seismic-refraction measurements, *Bull. Seismol. Soc. Am., 59*, 101-130, 1969.

Kanamori, H., The energy release in great earthquakes, *J. Geophys. Res., 82*, 2981-2987, 1977.

Kanamori, H., and G. S. Stewart, Mode of strain release along the Gibbs fracture zone, mid-Atlantic ridge, *Phys. Earth Planet. Inter., 11*, 312-332, 1976.

--

Klein, F. W., and R. Y. Koyanagi, Hawaiian Volcano Observatory seismic network history 1950-79, *U.S. Geol. Surv. Open File Rep., 80-302*, 1980.

Koyanagi, R. Y., H. L. Kivroy, and A. T. Okamura, The 1962 Kaoiki, Hawaii earthquake and its aftershocks, *Bull. Seismol. Soc. Am., 56*, 1317-1335, 1966.

Koyanagi, R. Y., D. A. Swanson, and E. T. Endo, Distribution of earthquakes related to mobility of the south flank of Kilauea volcano, Hawaii, *U.S. Geol. Surv. Prof. Pap., 800-D*, D89-D97, 1972.

Koyanagi, R. Y., E. T. Endo, and J. S. Ebisu, Reawakening of Mauna Loa volcano, Hawaii: A preliminary evaluation of seismic evidence, *Geophys. Res. Lett., 2*, 405-408, 1975.

Lipman, P. W., Rates of volcanic activity along the southwest rift zone of Mauna Loa volcano, Hawaii, *Bull. Volcanol., 43*, 703-725, 1980.

Macdonald, G. A., Activity of Hawaiian volcanoes during the years 1940-1950, *Bull. Volcanol., 15*, 119-179, 1954.

Macdonald, G. A., The activity of Hawaiian volcanoes during the years 1951-1956, *Bull. Volcanol., 22*, 3-70, 1959.

--

Macdonald, G. A., and C. K. Wentworth, The Kona earthquake of August 21, 1951, *Volcano Lett., 513*, 1-4, 1951.

Macdonald, G. A., A. T. Abbot, and F. L. Peterson, *Volcanoes in the Sea,* 2nd ed., 517 pp., University of Hawaii Press, Honolulu, 1983.

Nakamura, K., Why do long rift zones develop in Hawaiian volcanoes (in Japanese), *Kazan, 25*, 255-269, 1980.

Richter, C. F., *Elementary Seismology,* W. H. Freeman, San Francisco, Calif., 1958.

Stearns, H. T., *Geology of the State of Hawaii,* Pacific Books, Palo Alto, Calif., 1966.

Swanson, D. A., W. A. Duffield, and R. S. Fiske, Displacement of the south flank of Kilauea volcano: The result of forceful intrusion of magma into the rift zones, *U.S. Geol. Surv. Prof. Pap., 963*, 39 pp., 1976.

Tanigawa, W. R., J. S. Nakata, and A. H. Tomori, Hawaiian Volcano Observatory summary 82 — Seismic data, January to December 1982, U.S. Geol. Surv., 1983.

Tilling, R. I., R. Y. Koyanagi, P. W. Lipman, J. P. Lockwood, J. G. Moore, and D. A. Swanson, Earthquake and related catastrophic events, Island of Hawaii, November 29, 1975: A preliminary report, *U.S. Geol. Surv. Circ., 740*, 33 pp., 1976.

Tréhu, A. M., J. L. Nábělek, and S. C. Solomon, Source characterization of two Reykjanes Ridge earthquakes: Surface waves and moment tensors; *P* waveforms and nonorthogonal nodal planes, *J. Geophys. Res., 86*, 1701-1724, 1981.

Unger, J. D., and P. L. Ward, A large deep Hawaiian earthquake — the Honomu, Hawaii event of April 26, 1973, *Bull. Seismol. Soc. Am., 69*, 1771-1781, 1979.

U.S. Geological Survey, *The Volcano Letters, 1-530*, 1925-1955.

Vanek, J., A. Zatopek, V. Karnik, N. V. Kondorskaya, Y. V. Riznichenko, E. F. Savarensky, S. L. Solov'ev, and N. V. Shebalin, Standardization of magnitude scales, *Bull. Acad. Sci. USSR Geophys. Ser. 2*, Engl. Transl., 108-111, 1962.

Ward, P. L., and S. Gregersen, Comparison of earthquake locations determined with data from a small network of stations and small tripartite arrays on Kilauea volcano, Hawaii, *Bull. Seismol. Soc. Am., 63*, 679-711, 1973.

Wiens, D. A., and S. Stein, Age dependence of oceanic intraplate seismicity and implications for lithospheric evolution, *J. Geophys. Res., 88*, 6455-6468, 1983.

Chapter 2

A Single-Force Model for the 1975 Kalapana, Hawaii Earthquake

Abstract

A single force mechanism is investigated as the source of long-period seismic radiation from the 1975 Kalapana, Hawaii earthquake ($M_S = 7.1$). The observed Love wave radiation pattern determined from the spectra of WWSSN and HGLP records at 100 s is two-lobed with azimuth, consistent with a near-horizontal (dip $\sim 10^o$) single force acting opposite (strike $\sim 330^o$) to the observed displacement direction of the earthquake; this pattern is inconsistent with the expected double-couple pattern. Assuming a form of the force time history of a one-cycle sinusoid, the total duration of the event estimated from Rayleigh waves at two IDA stations is approximately 180 s. The peak amplitude f_o of the time function is 1 x 10^{20} dyne from amplitudes of Love and Rayleigh waves. The interpretation is that the bulk of the seismic radiation was produced by large-scale slumping of a large area of the south flank of Kilauea volcano. The single force is a crude representation of motion of a large slide mass that is partially decoupled from the Earth. Using the mass estimated from the tsunami generation area (10^{18} – 10^{19} grams), the peak acceleration of the slide block (10 - 100 cm s^{-2}) inferred from the seismic force is comparable with the acceleration due to gravity on a gently inclined plane. The slump model for the Kalapana earthquake is also more qualitatively consistent with the large horizontal deformation (8 m onland) and tsunami associated with the earthquake, which are difficult to explain with the conventional double-couple source model. The single force source has been used previously to model the long-period seismic waves from the landslide accompanying the eruption of Mt. St. Helens volcano, and may explain other anomalous seismic events where the predominant mechanism is massive slumping of sediments or unconsolidated material and not elastic dislocation.

1. Introduction

Non-double-couple mechanisms have been investigated recently as source models for seismic events. The single force was invoked as a viable seismic source by Kanamori and Given (1982) to explain the long-period surface waves associated with the Mt. St. Helens eruption sequence. They interpreted the force as the seismic signature of the massive landslide that occurred on the north slope of the volcano. Along other lines, non-double-couple mechanisms discovered during routine moment tensor inversions of earthquake data are being interpreted in a variety of ways, from complex details of the rupture, to intrinsically different source processes (Sipkin, 1986). As the sensitivity and band range of available seismic instrumentation continue to increase, we will be able to detect seismic signals from geological phenomena other than earthquakes that occur abruptly enough to be seen as seismic events, such as massive sediment slides, or volcanic explosions. Previously such events may have been interpreted, by default, as conventional elastic dislocation earthquakes, but they may have different sources than the double force couple.

In this paper, we show that the long-period seismic radiation from the large 1975 Kalapana, Hawaii earthquake (M_S=7.1) is best explained by a single force model. The observed coseismic deformation and large tsunami amplitude associated with the earthquake are anomalous for an event of this magnitude. Several geologic studies have proposed a large-scale gravitational slump or landslide to explain observations of the earthquake. We propose that during a slump event, the upper slide block becomes essentially decoupled from the Earth, producing an apparent single force. Other seismological studies of the earthquake have assumed the elastic dislocation source, and have not addressed the question of whether the seismic radiation itself could be

produced by massive slumping. Many examples of massive submarine slumps, located offshore systems of normal faults flanking volcanic centers, are found on the Hawaiian Ridge, indicating that large scale slumping can be a common mode of deformation in an oceanic volcanic regime.

This study follows some of the techniques of the Mt. St. Helens analysis (Kanamori and Given, 1982). Due to a limited data set, a study with the rigor of that analysis was not possible for the Kalapana earthquake. In 1975 when the earthquake occurred, the high-gain digital IDA (International Deployment of Accelerometers) and GDSN (Global Digital Seismic Network) networks were still in developmental stages. The analysis presented here uses mainly WWSSN records and some supplemental data from the HGLP (High Gain Long Period) network, a prototype of the present-day ASRO (Abbreviated Seismic Research Observatory) stations of the GDSN network. Two early operating IDA stations provided additional long-period Rayleigh wave data.

Previous Studies of the Kalapana Earthquake

A sketch map of the relevant area of the island of Hawaii, showing the epicenter of the Kalapana earthquake, is given in Figure 1. Note the location of Kilauea crater, its rift zones, and the major faults. An excellent observational summary of the earthquake was provided by Tilling et al. (1976), and deformations have been discussed by Lipman et al. (1985). The accompanying tsunami has been described by Hatori (1976) and Cox (1980). Seismic analyses of surface and body waves and implications were published by Ando (1979) and Furumoto and Kovach (1979).

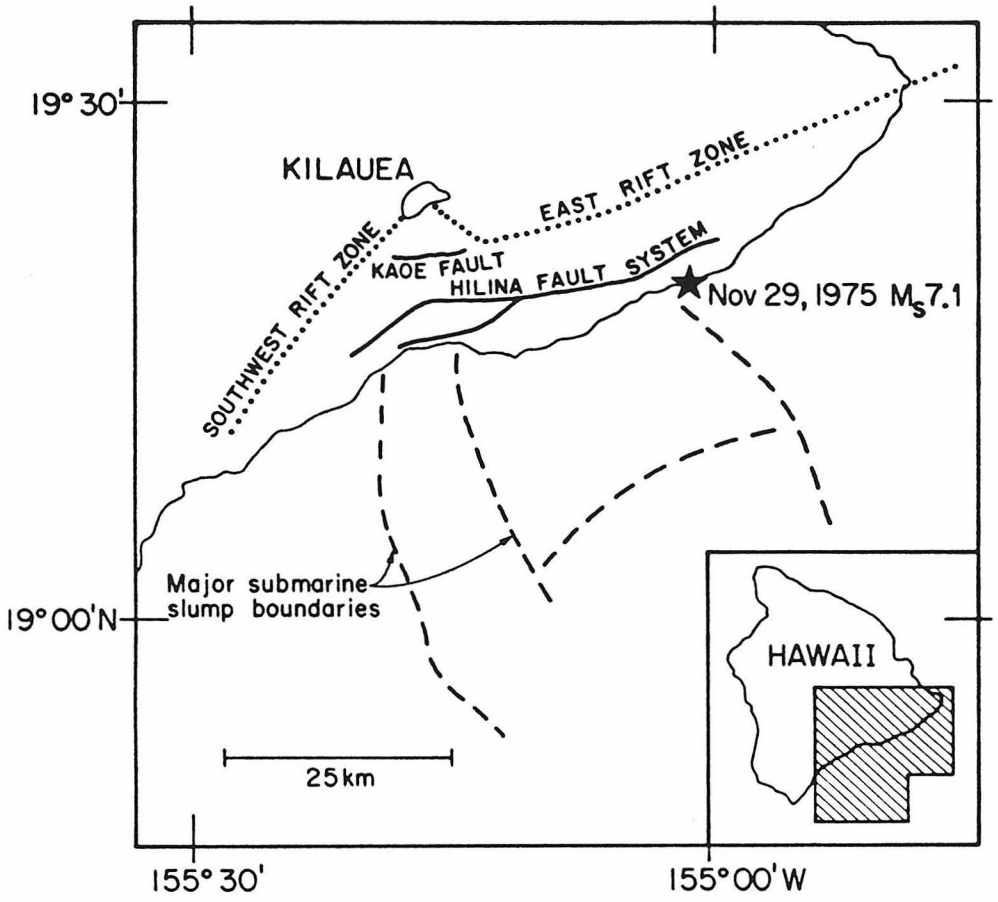

Figure 1. Sketch map of the area of Hawaii involved in the Kalapana earthquake, adapted from Macdonald et al. (1983). Outlines are shown of approximate boundaries of major submarine slumps built up during the extended history of the island.

The essential points of the above studies can be summarized as follows. The earthquake occurred on November 29, 1975, with $M_S = 7.1$ ($M_L = 7.2$), the largest instrumental magnitude reported to date for a Hawaiian earthquake. The epicenter was on the southeast coast of the island of Hawaii, near the small town of Kalapana. Hawaii Volcano Observatory (HVO) gave the location as 19^o 20'N, 155^o 02'W, h = 5-7 km, origin time 14h 47m 40.4s U.T. A foreshock of $M_L = 5.7$ preceded the event. The earthquake affected most of the south flank of Kilauea volcano, between the southwest rift zone and the east rift zone. The large static deformations that were caused by the earthquake are shown in Figure 2. Coseismic subsidence was observed along 50 km of the south coast between the rift zones; the largest subsidence was 3.5 m at Halape beach, about 30 km southwest of the epicenter. Observed horizontal extensions increased steadily seaward over the south flank, from about 1 m at the summit to 8 m at the coast; again, the maximum extension was in the vicinity of Halape beach (Lipman et al., 1985). Ground cracking was observed along 25 km of the Hilina fault system, with a maximum displacement of about 1.5 m down-dropped to the south. A severe tsunami reached a maximum height of 14.6 m at Halape beach, where two campers were killed. A small eruption broke out on the floor of Kilauea caldera half an hour after the origin time, and continued for 21 hours. Similar large earthquakes accompanied by tsunamis previously occurred on this part of the island in 1868 and (less certain) 1823.

Teleseismic P wave fault plane solutions from both of the seismic studies determined one steeply dipping (80^o - 90^o) nodal plane with a strike of about N60^o E (Figure 3). The inferred low-angle nodal plane is the fault plane preferred by these authors, as it is more compatible with the deformation and tsunami observations. The near-horizontal, planar distribution of aftershocks between depths of 5-10 km also

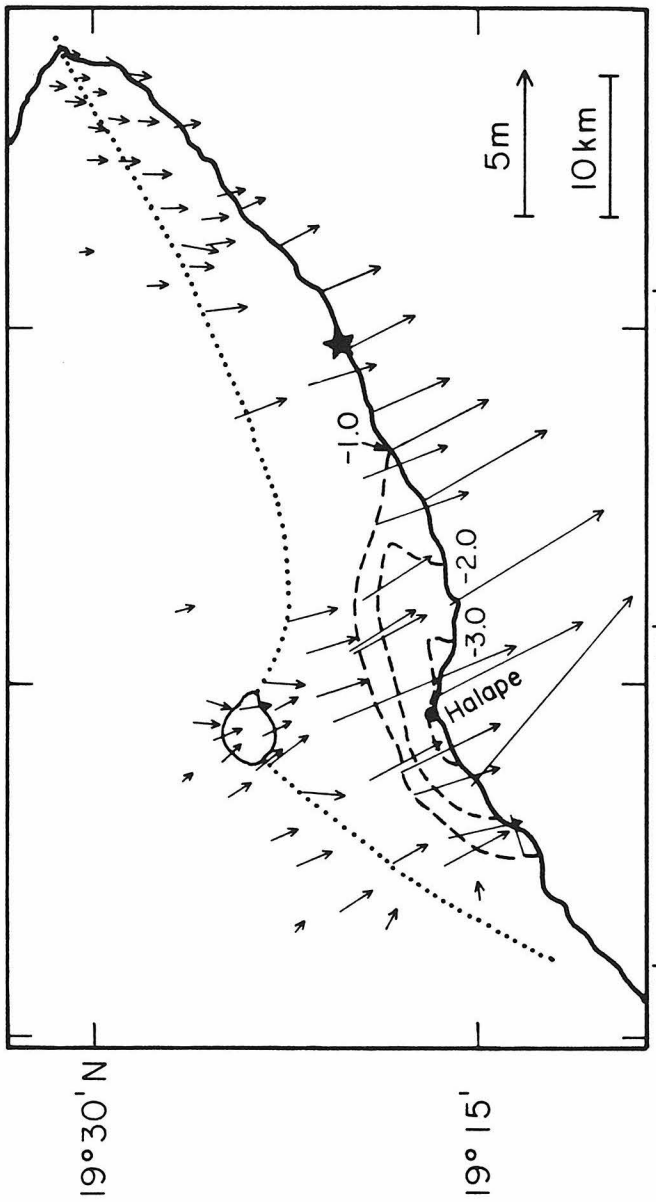

Figure 2. Map of the observed horizontal (vectors) and vertical (dashed contours) displacements associated with the Kalapana earthquake, adapted from Lipman et al. (1985). The maximum displacements occurred in the vicinity of Halape beach, about 30 km southwest of the epicenter (star). Horizontal displacements increase steadily seaward from $\sim$ 1 m at the summit of Kilauea to $\sim$ 8 m at Halape. Contours of vertical displacements are in meters.

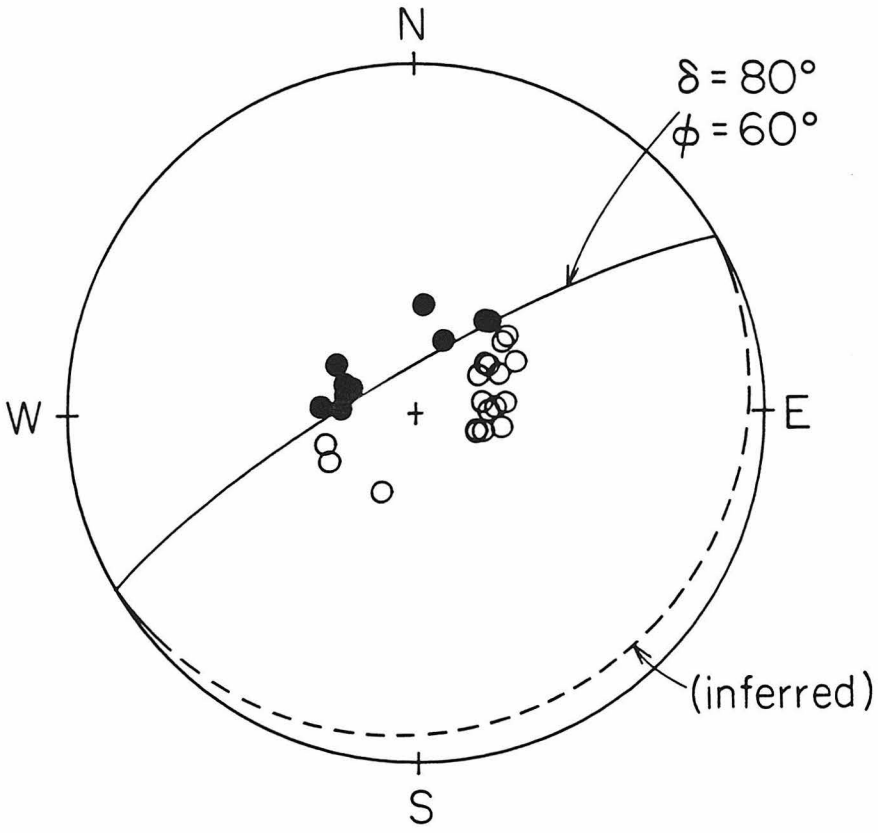

Figure 3. Teleseismic P wave first motion mechanism of the Kalapana earthquake, redrawn from Ando (1979). The low-angle (dashed) nodal plane is inferred.

supports this choice. The inferred slip direction was purely dip-slip, oriented N150^o E. The seismic moment was determined from surface waves to be between 1.2 - 1.8 x 10^{27} dyne cm. The earthquake produced an extremely complex sequence of body waves, indicating a complex source. A strong-motion record at Hilo showed at least 5 sub-events, for a total duration of 75 s (Rojahn and Morrill, 1977).

The observations of the Kalapana earthquake described above indicate seaward displacement of a large block on a near horizontal plane. Previous studies of the earthquake propose either that the event was triggered by a sudden increase in magmatic pressure in the east rift zone which changed the stress regime enough to overcome the locking stress and push the south flank on the slide plane (Ando, 1979; Furumoto and Kovach, 1979; Crosson and Endo, 1981), or that the driving force was the inherent gravitational instability of the poorly consolidated and growing volcanic pile (Nakamura, 1980). Swanson et al. (1976) noted that the entire south flank of Kilauea is essentially mobile, and had undergone extensions of several meters in the last century previous to the 1975 earthquake. The pre-volcanic oceanic crust, located at about 7 km depth and lubricated by a thick accumulation of deep sea sediments, is proposed as the detachment plane. The Hilina fault system (Figure 1) provides a major detachment zone of the mobile block. This fault system consists of a spectacular set of southeast-facing scarps ("pali" in the vernacular), displaced in a normal sense, with a maximum offset of 500 m. Lipman et al. (1985) propose that surface faults such as the Hilina system become listric at depth and join with the volcano-crust interface, providing a locus for block rotations and slumps due to gravitation. Planar seismicity on the volcano-crust interface extends north of the Hilina system to the approximate location of the Koae fault (Figure 1), suggesting that it too serves as a detachment locus. Large submarine slumps about 30 km wide and extending at

least 20 km out from the coast have been mapped offshore the Hilina fault system (Moore and Peck, 1965). The Hilina Pali and the submarine slumps are thought to have been built up by repeated deformation events, some of which involved long-term extensions, and some of which were seismic events such as the Kalapana earthquake.

Double-Couple and Single-Force Radiation Patterns

Ando (1979) constructed radiation patterns from the amplitudes of Love and Rayleigh surface waves from the Kalapana earthquake recorded on the WWSSN network. The observed Rayleigh wave pattern matches the theoretical pattern computed for a double-couple source with the same orientation as the P wave first motion solution ($\delta = 10^o$, $\phi = 60^o$, and $\lambda = -90^o$). The observed Love wave radiation pattern, on the other hand, is problematic. It is distinctly two-lobed, whereas the theoretical pattern for the double couple is four-lobed. Ando (1979) concluded that the expected second node was missing due to a lack of data in the critical azimuth. The two-lobed Love wave pattern is rotated 90^o with respect to the Rayleigh wave pattern.

In this Section we discuss the theoretical radiation patterns generated by a double-couple source and a single force source. We will attempt to show later from surface wave observations that the best model for the long-period source of the Kalapana earthquake is a near-horizontal single force, oriented opposite to the inferred slip direction. This is very similar to the source used to describe the long-period surface waves associated with the May 18, 1980 eruption of Mt. St. Helens. Kanamori and Given (1982) noted that the Love waves had a two-lobed radiation pattern which could not be explained by a double-couple source, and that the Love wave pattern was rotated 90^o with respect to the Rayleigh wave pattern. They resolved a near-

horizontal single force with a long source time function. The force was interpreted as the seismic expression of the voluminous landslide that accompanied the eruption; as the mass slid downslope, its acceleration produced a force on the Earth in the opposite direction (Figure 4, reprinted from Moore and Albee (1981)).

Although the Kalapana earthquake and the Mt. St. Helens eruption are very different types of events, they both involved displacement of a large mass on a subhorizontal plane. Obviously, earthquakes occur that involve faulting on a low-angle plane that can be explained adequately by a double-couple source. The difference between the double couple and the single force is described conceptually in Figure 5. Figure 5*a* shows a map view of the epicenter, strike of the fault plane along the coast, and inferred slip direction of the earthquake (roughly perpendicular to the coast). Figure 5*b* draws, in crossection, the double-couple force system corresponding to a low-angle normal fault. In the double couple model, the blocks on both sides of the fault plane exert a force on each other as they move, and both blocks transmit this effect through to the Earth.

The theoretical spectrum of Love waves at the source for a double couple depends on the fault parameters δ, λ, and ϕ as follows:

$$\hat{V}_{\phi}(\omega)=M_o\,[(\sin\lambda\sin\delta\cos\delta)\sin2\phi P_L^{(1)}(h,\omega)+(\cos\lambda\sin\delta)\cos2\phi P_L^{(1)}(h,\omega) \qquad (1)$$

$$-i\,(\cos\lambda\cos\delta)\sin\phi\, Q_L^{(1)}(h,\omega)+i\,(\sin\lambda\cos2\delta)\cos\phi\, Q_L^{(1)}(h,\omega)]$$

where $P_L^{(1)}$ and $Q_L^{(1)}$ are the real-valued excitation functions given by Kanamori and Given (1981), M_o is the seismic moment, h is the source depth, ω denotes the angular frequency, ϕ is the azimuth of the station measured counterclockwise from the strike of the fault plane, and δ and λ are the fault parameters dip and slip angle (Kanamori and Given, 1981). Note that Equation 1 has a four-lobed dependence on ϕ due to the

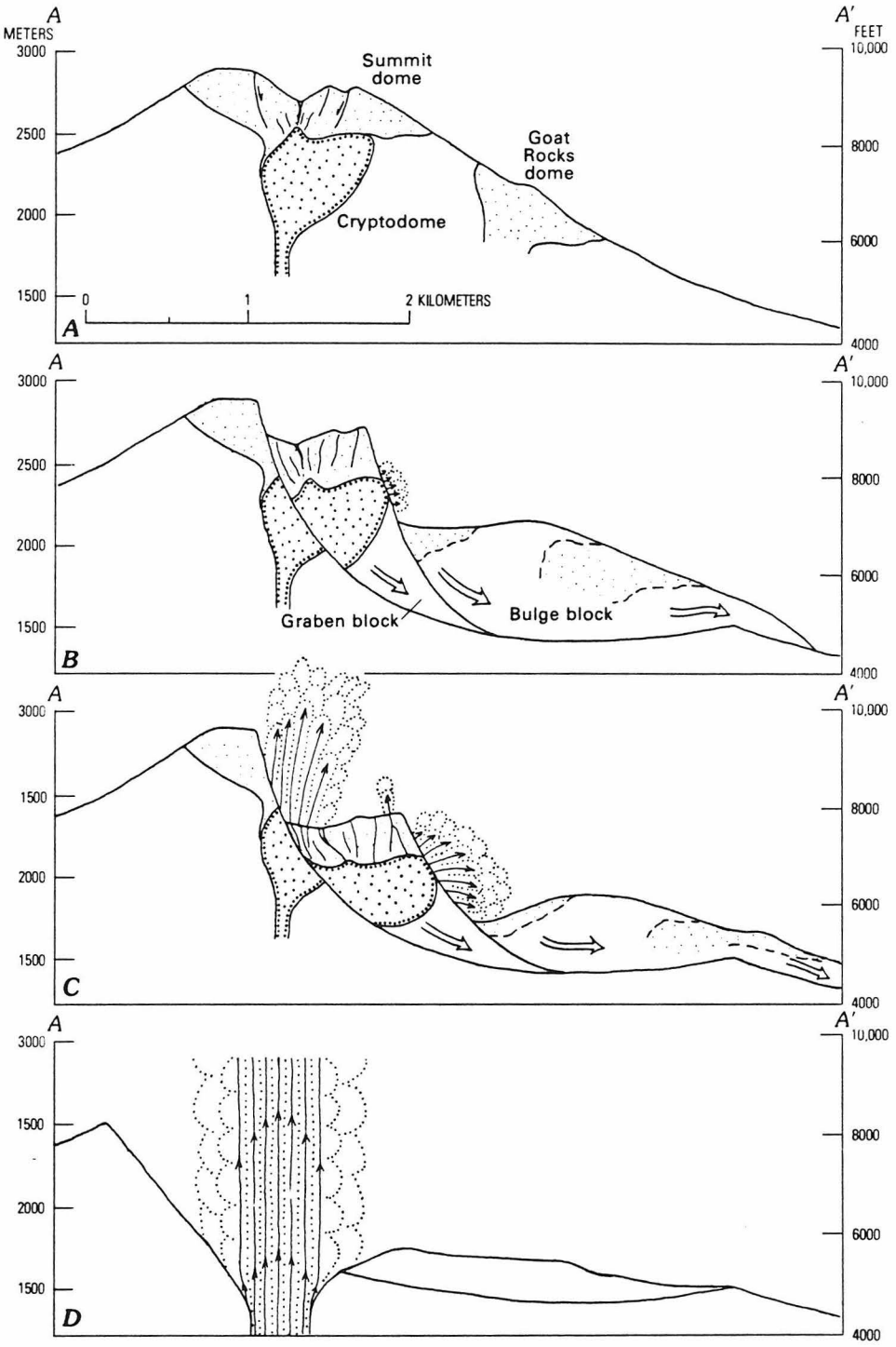

Figure 4. Depiction of the May 18, 1980 landslide/eruption sequence of Mt. St. Helens volcano, Washington, reprinted from Moore and Albee (1981). A massive landslide of the north slope of the volcano accompanied the eruption and produced long-period seismic signals that were observed worldwide.

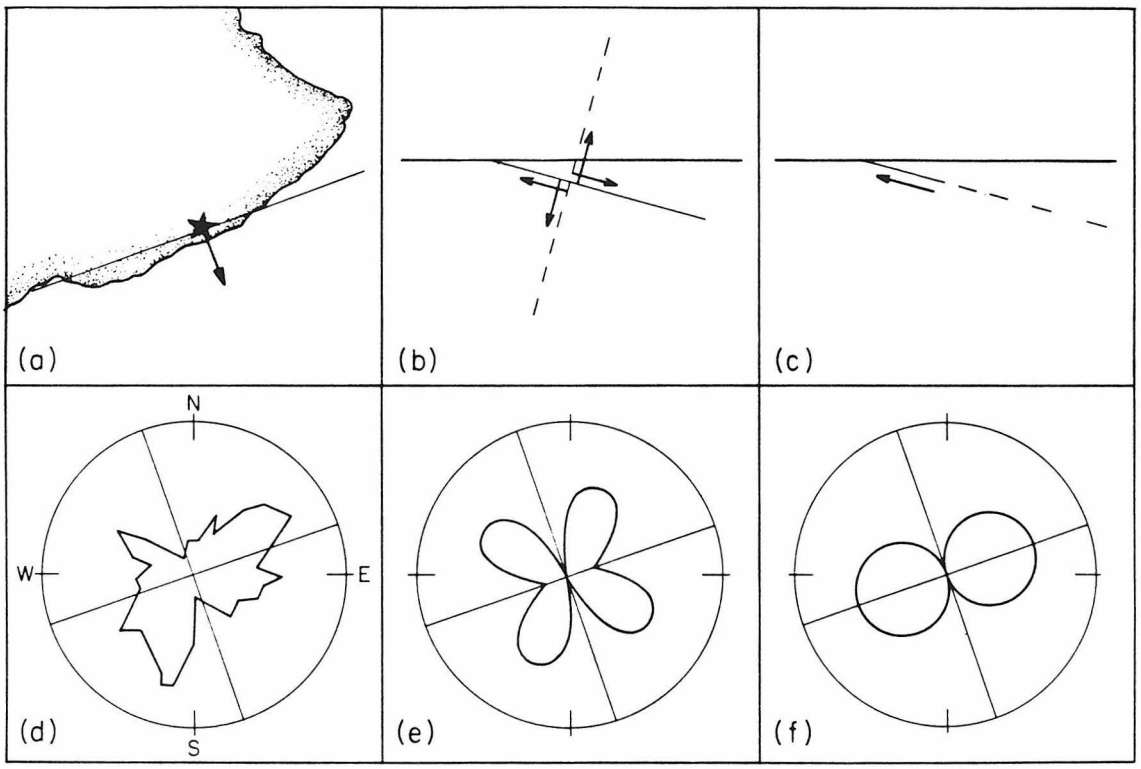

Figure 5. Schematic description of the distinction between the double force couple seismic source and the single force seismic source. (*a*) Epicenter of the Kalapana earthquake, strike of the inferred fault plane approximately parallel to the coast, and direction of the observed maximum displacement (arrow). (*b*) In crossection, double force couple system corresponding to a normal-fault dislocation on a low-angle fault plane. The auxiliary nodal plane is shown by the dashed plane. (*c*) Single force on the Earth produced by decoupled motion of the upper block, which slides in the opposite direction. (*d*) Observed radiation pattern of Love waves from the Kalapana earthquake, redrawn from Ando (1979). (*e*) Theoretical Love wave radiation pattern for a double couple consistent with the focal mechanism of the Kalapana earthquake; the pattern is four-lobed in azimuth. (*f*) Theoretical pattern for the single force (force strike, 330°). The pattern is two-lobed, with the radiation maximum in the azimuth perpendicular to the force direction.

$\cos 2\phi$ and $\sin 2\phi$ factors multiplying $P_L^{(1)}$ for any fault orientation except a purely horizontal fault ($\delta = 0$) or a vertical dip slip fault ($\delta = 0$, $\lambda = 0$), where the coefficients of $P_L^{(1)}$ vanish.

The theoretical Love wave radiation pattern for a double-couple source, oriented to produce the displacement inferred for the Kalapana earthquake, is shown in Figure 5*e*.

Figure 5*c* shows a schematic model of the single force source. The upper block exerts an opposite force on the Earth as it moves. If this block becomes decoupled, as indicated by the dashed line, it will not transmit the effect of the opposite force to the body of the Earth. Seismically, then, only one force is observed. Intuitively, it is essential for the event to be shallow to allow this decoupling effect. A substantial overburden pressure will couple the upper block into the Earth, as in the case of the buried fault (i.e., the double couple).

For a unit single force with dip α (measured positive up from horizontal), the theoretical Love wave source spectrum is given by

$$\hat{V}_\phi(\omega) = -i \cos\alpha \sin\phi \frac{r_s}{N} P_L^{(1)}(h, \omega) \tag{2}$$

where r_s is the distance from the source to the center of the Earth, N is the order number of the mode with angular frequency ω, and ϕ is the azimuth of the station measured counterclockwise from the azimuth of the force (Kanamori and Given, 1982). Note that Equation 2 has a two-lobed dependence on ϕ, with the nodal direction oriented in the direction of the force.

The theoretical Love wave pattern for a single force, oriented to produce the displacement inferred for the Kalapana earthquake, is shown in Figure 5*f*. The force parameters are $\alpha = 10^o$ with an azimuth of 330^o, opposite to the direction of motion

of the upper block.

The observed Love wave pattern is reproduced in Figure 5*d* from Ando (1979). The observed pattern is clearly more consistent with the single force source. Both sources fit the observed node at 150^o. However, where the single force pattern has its maximum at 60^o, the double-couple pattern predicts a minimum. The observed radiation pattern of Love waves will be reexamined in a later Section.

The effect of source depth is included in Equations 1 and 2 through the excitation functions $P_L^{(1)}$ and $Q_L^{(1)}$. Their specific dependence on depth is determined by the eigenfunctions of the torsional modes of free oscillation, which are functions of the elastic properties of the medium. $P_L^{(1)}$ and $Q_L^{(1)}$ are proportional to the tangential particle velocity and stress respectively, evaluated at the source depth. Thus at the free surface (zero source depth) where the surface tractions vanish, the function $Q_L^{(1)}$ goes to zero, while $P_L^{(1)}$ stays finite. Recall from Equation 1, the purely horizontal fault (or equivalently, the vertical dip-slip fault) is the only double-couple orientation that eliminates the 2ϕ dependence, thus producing a two-lobed radiation pattern. However, this geometry contains only the $Q_L^{(1)}$ function. Thus for a shallow, purely horizontal fault, the seismic moment would have to be very large to produce appreciable Love wave amplitudes. Ando (1979) used this to argue against the apparent two-lobed appearance of the Love wave radiation pattern; he showed that as the fault plane dip approaches horizontal, the seismic moment required to produce the observed Love wave amplitudes becomes so large that it is inconsistent with the observed static deformation. He thus concluded that the fault plane must have a moderate dip angle ($10 - 20^o$), that the Love wave pattern must be four-lobed, and that the apparent discrepancy was due to an incomplete data set.

The P wave radiation pattern for a double couple is most simply represented by the quadrant focal mechanism figure (for example, Figure 3). Two nodal planes divide the focal sphere into dilatational and compressional quadrants. A single force in a whole space will have only one nodal plane, perpendicular to the force, separating the focal sphere into two regions of dilatational and compressional motion.

For a double couple corresponding to a low-angle fault, usually only one nodal plane is constrained from teleseismic first motion data because teleseismic stations have take-off angles near the center of the focal hemisphere, whereas the low-angle plane plots near the edge of the diagram. Thus the first-motion data in Figure 3 could be fit either by a double-couple or a single force source. However, first motions from the local HVO network weakly suggest a quadrant distribution (Furumoto and Kovach, 1979; Crosson and Endo, 1981), so that the Kalapana earthquake may have been a standard double-couple source in its initial stage.

2. Long-Period Love Wave Radiation Pattern

Clarification of the azimuthal Love wave amplitude variation proves to be crucial in determining which force system best represents the overall source of the Kalapana earthquake. The previously published Love wave pattern is two-lobed, but this was dismissed as due to an incomplete data set, largely because the single force simply was not recognized as an alternative at the time. Studies of the Mt. St. Helens eruption sequence have shown that the single force can be a viable seismic source, describing large-scale, shallow sliding deformation. In this Section we carefully reexamine the Love wave amplitudes at longer periods, and conclude that the azimuthal

pattern is consistent with a near-horizontal single force.

Because of the moderate size of the earthquake, Love waves of sufficiently long period (i.e., whose amplitudes are unaffected by most lateral velocity heterogeneities) have low amplitudes on the WWSSN instrument. Thus, WWSSN stations with the highest gains were chosen. Lower gain stations were included if they were located in critical azimuths. Seven of the 12 WWSSN stations chosen had been used by Ando (1979). In addition, Love wave data from 5 HGLP stations were used. Station data are listed in Table 1. Although Ando (1979) used amplitudes of G_1, G_2, and G_3 waves, we limited the data set to the G_2 passage only. In some cases, G_1 was contaminated by multiple S phases, and the G_3 passage was at noise level for most of the stations.

For each station, the two horizontal-component seismograms were windowed between velocities of 4.6 km s^{-1} and 4.0 km s^{-1} for the G_2 distance, digitized, and rotated into transverse seismograms. The rotated HGLP seismograms are shown in Figure 6, and the WWSSN seismograms are shown in Figure 7. The maximum peak-to-peak record amplitudes in millimeters, equalized to an instrument gain of 1000, are shown above the waveforms. Although each record shows a clear G_2 wavetrain, the maximum amplitudes can occur at different periods, or different parts of the wavetrain. This is particularly true for the WWSSN records. Note that Ando (1979)'s radiation pattern was made from the maximum time-domain amplitudes. For a more precise measure of signal amplitude, each wavetrain was Fourier transformed, and the amplitudes examined as a function of period.

The observed source amplitude spectrum $|\hat{V}_\phi(\omega)|$ can be obtained from the spectrum of the seismogram by correcting for propagation effects and the instrument response. This can be written as

$$| \hat{V}_{\phi}(\omega) | = \hat{S}(\omega)\sqrt{\sin\Delta}\, \exp(\frac{\omega\Delta_{km}{}'}{2QU})/\hat{I}(\omega) \qquad (3)$$

where $\hat{S}(\omega)$ is amplitude spectrum of the observed transverse seismogram, Δ is the source-to-station distance, $\Delta_{km}{}'$ is the G_2 propagation distance in km, Q the attenuation factor, U the group velocity, and $\hat{I}(\omega)$ represents the amplitude response of the instrument. Values for Q and U were taken from Kanamori (1970).

Given the limited band of the WWSSN instrument, 100 s was the longest period at which the spectra could be read with confidence. Values of $| \hat{V}_{\phi} |$ at a period of 100 s are listed in Table 2; Figure 8 shows $| \hat{V}_{\phi} |$ at 100 s plotted vs azimuth. The solid line shows the theoretical azimuthal dependence ($\sin\phi$) for the single force source.

The observed pattern is two-lobed in azimuth, with a clear radiation maximum at 60^{o} and a node at 150^{o}. Both the static deformation pattern and the teleseismic focal mechanism of Kalapana earthquake imply a slip direction with azimuth 150^{o}. The single force on the Earth resulting from this slip direction would be oriented in the opposite azimuth, 330^{o}. The observed Love wave radiation pattern is consistent with that of a single force oriented at 330^{o}; nodes lie along the force direction, and maxima lie in the perpendicular directions. The two-lobed nature of the observed pattern itself precludes any realistic double-couple source; in addition, the observed maxima and nodes are located as expected for a single force source that is consistent with the field observations. The radiation pattern from the spectral amplitudes of long-period Love waves thus supports the single force model.

Table 1

Station List, Love Wave Analysis

Station Name	Gain	Distance, Deg.	Azimuth, Deg.
HGLP Stations:			
CHG Chiengmai, Thailand	2800	98.1	293
CTA Charters Towers, Australia	2500	69.6	239
KON Kongsberg, Norway	2100	100.3	8
TLO Toledo, Spain	2100	115.2	24
ZLP Zongo Valley, Bolivia	3600	92.4	106
WWSSN Stations:			
BAG Baguio, Philippines	3000	79.6	284
CTA Charters Towers, Australia	3000	69.6	239
ESK Eskdalemuir, Scotland	750	101.9	16
IST Istanbul, Turkey	750	119.8	357
MAL Malaga, Spain	1500	117.7	26
MAT Matsushiro, Japan	3000	60.3	302
NUR Nurmijarvi, Finland	1500	100.4	0
RIV Riverview, Australia	750	73.6	225
SHL Shillong, India	3000	101.1	302
SJG San Juan, Puerto Rico	750	83.2	73
TAB Tabris, Iran	1500	119.5	341
TAU Tasmania University, Tasmania	750	81.5	219

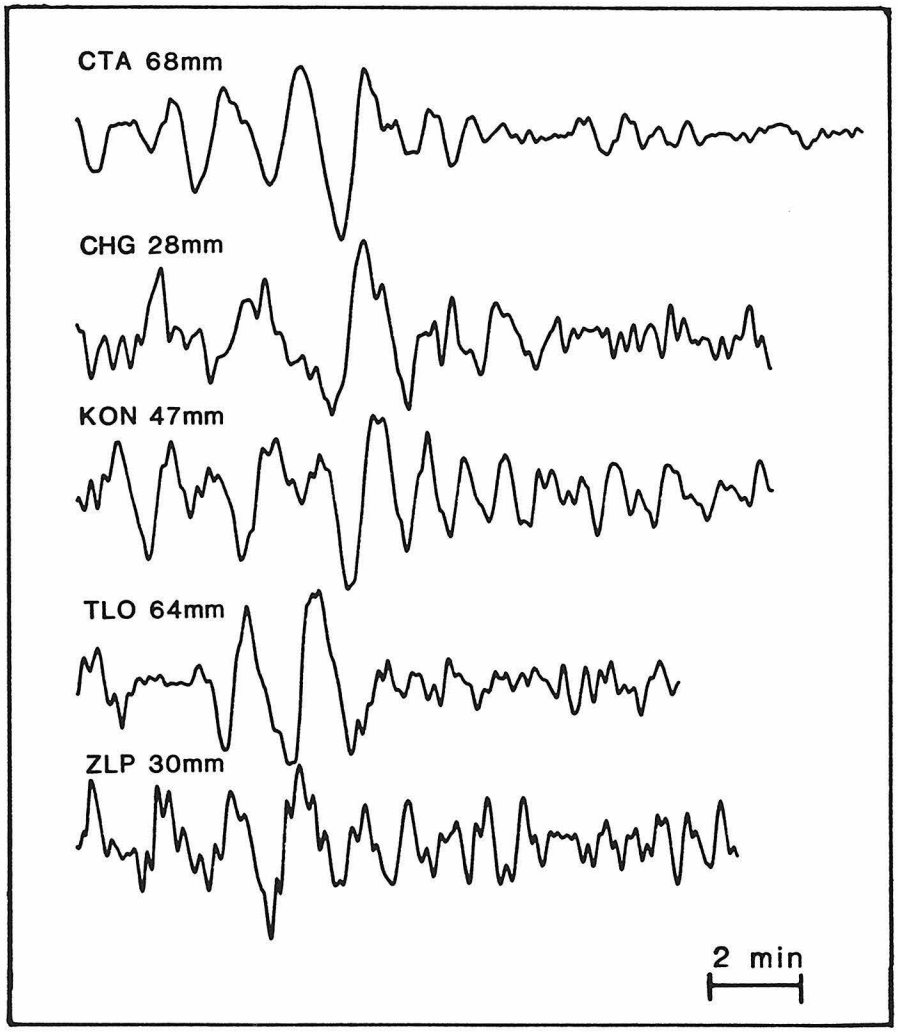

Figure 6. Observed G_2 passages of Love waves from HGLP stations. The maximum peak-to-peak amplitudes (mm of paper record) are shown above the traces.

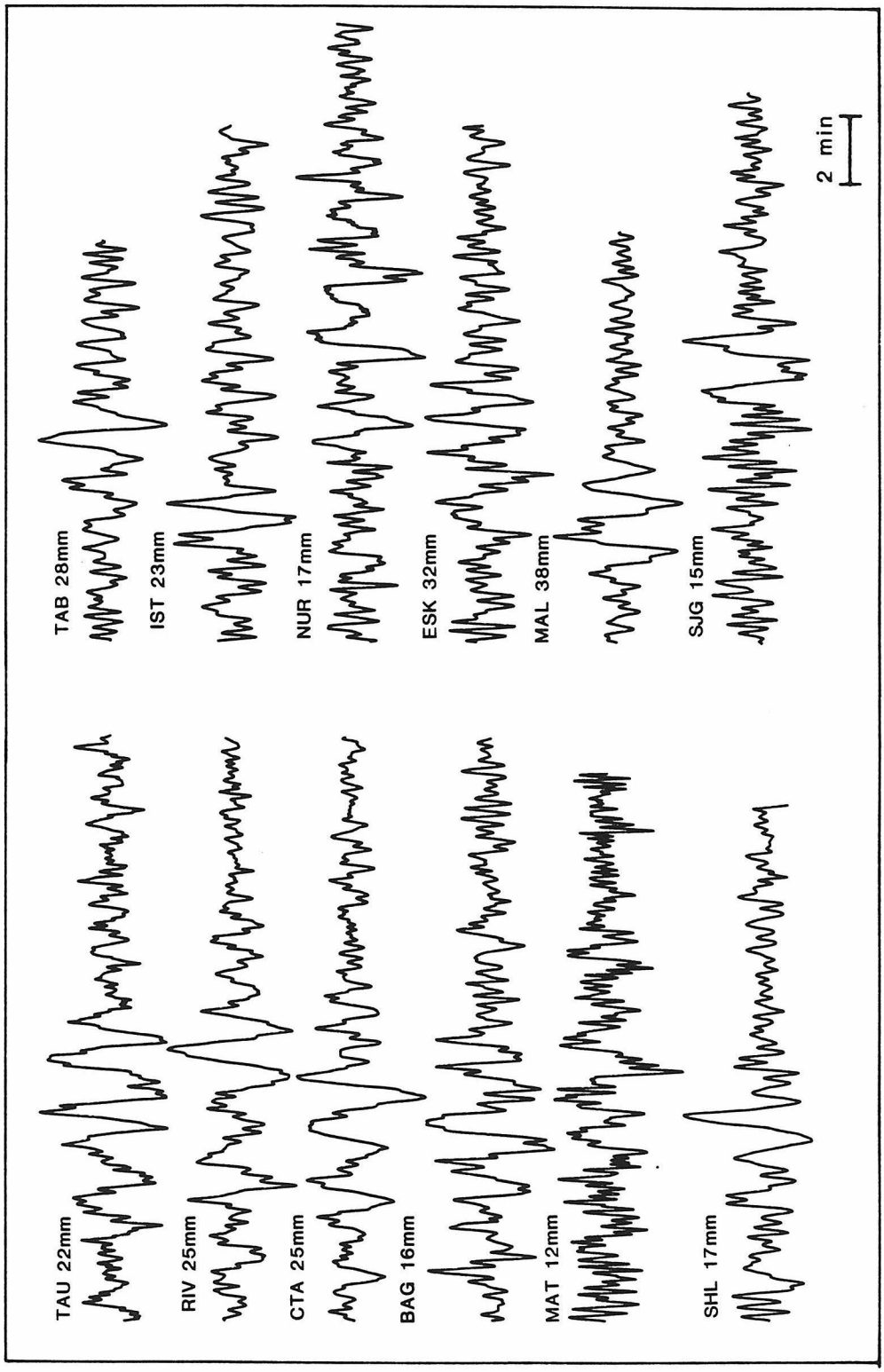

Figure 7. Observed G_2 passages of Love waves from WWSSN stations.

Table 2

Amplitude Spectra of G_2 Waves,
Corrected to Source

Station Name	G_2 Distance, Deg.	G_2 Azimuth, Deg.	Amplitude at 100 s, cm s
HGLP Stations:			
CTA	290.4	59	2.6
CHG	261.9	113	0.8
KON	259.7	188	0.9
TLO	244.8	204	1.7
ZLP	267.6	286	0.6
WWSSN Stations:			
TAU	278.5	39	2.1
RIV	286.4	44	2.9
CTA	290.4	59	3.0
BAG	280.4	104	1.7
MAT	299.7	122	1.2
SHL	258.9	122	1.0
TAB	240.5	161	0.9
IST	240.2	177	0.8
NUR	259.6	180	0.8
ESK	258.1	196	2.3
MAL	242.3	206	2.1
SJG	276.8	253	1.7

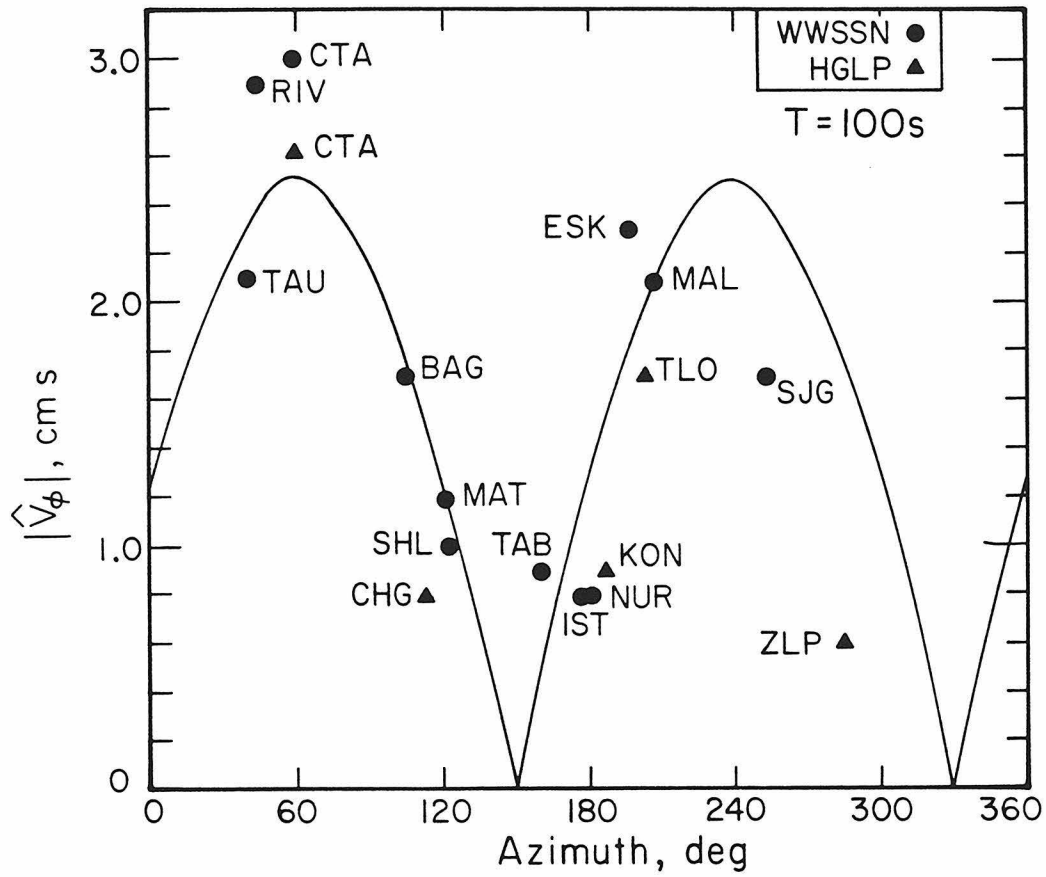

Figure 8. Observed source spectrum amplitudes vs. azimuth of Love waves at a period of 100 s. There is a clear maximum at 60^o, which is a predicted maximum for the single force source but a minimum for the double couple source. Both sources predict the observed node at 150^o.

3. Rayleigh Wave Analysis

Long-period Rayleigh wave data from two IDA stations that were operating at Canberra, Australia and Naña, Peru provide additional information on the source of the Kalapana earthquake. In particular, by forward modeling of the waveforms assuming a single force source, the time history and the amplitude of the force can be estimated. The R_2 and R_3 phases at both stations were used; R_1 was offscale. Unfortunately, CAN is very near to the node of the Rayleigh wave radiation pattern for the force orientation determined above (16^o from the node), and NNA is somewhat better, 45^o from the node (Table 3).

Vertical-component synthetic Rayleigh wave seismograms can be calculated by summing over spheroidal oscillations excited by a single force, as described by Kanamori and Given (1982). The ground motion is given by

$$U_r(\vec{r},t)=\sum_N r_s K_2 \left[-\frac{y_1(r_s)}{y_3(r_s)}\sin\alpha\, P_N{}^o - \cos\alpha\,\cos\phi P_N{}^1\right]\cos\omega_N t \qquad (4)$$

where α and ϕ define the force geometry, K_2 is the excitation function defined in Kanamori and Cipar (1974), $P_N{}^o$ and $P_N{}^1$ are Legendre functions, y_1 and y_3 are factors proportional to displacements specified by the order number N, r_s denotes the distance from the center of the Earth to the source, and ω_N is the eigenfrequency of the mode with order number N. Equation 4 assumes a step function source in time. The calculated seismogram $S_r(t)$ for a delta function source in time is then given by $\frac{d}{dt}U_r(t)$ convolved with the IDA instrument response.

The R_2 and R_3 phases at both stations seemed to be depleted in energy at periods less than about 100 s, and thus synthetic seismograms for a delta function

Table 3

Station List, Rayleigh Waves

Station	Phase	Distance, Deg.	Azimuth, Deg.	Observed Peak-to-Peak Amplitude, counts	Peak Force Size, dynes
NNA	R_2	227.0	285.1	915	1.1×10^{20}
NNA	R_3	443.0	105.1	678	1.5×10^{20}
CAN	R_2	284.1	44.4	441	2.0×10^{20}
CAN	R_3	436.0	224.4	193	1.6×10^{20}

time dependence were too short period to explain the data. In modeling the Mt. St. Helens landslide, Kanamori and Given (1982) originally assumed a smooth, half-cosine time function with a peak force f_o and a time constant τ:

$$f_o s(t) = \begin{cases} 1/2 f_o (1-cos(\pi t/\tau)) & 0 \leq t \leq 2\tau \\ 0 & t > 2\tau \end{cases} \quad (5)$$

They found that this time function generally fit both the time-domain waveforms and the source spectra retrieved from the data for $\tau \sim 75$ s. Note that the quantity $f_o s(t)$ is always positive for this time function. Subsequent work was done using intermediate period data from Mt. St. Helens (i.e. SRO and ASRO R_1 and G_1 waves), where the time history of the force was obtained by direct deconvolution over a limited frequency band (Kanamori et al., 1984). This revealed an "overshoot," or negative portion to the time function, which can be interpreted as deceleration of the slide mass. The total time duration of the Mt. St. Helens source with the overshoot included is 200 s.

The sampling rate of the IDA network at the time of the Kalapana earthquake was 20 s, which makes it difficult to stably resolve signal at periods of 50 - 100 s by direct deconvolution. Instead, we estimate the time history of the source by assuming a time function similar in form to that resolved from the Mt. St. Helens deconvolution, a simple one-cycle sine wave with half-period τ:

$$f_o s(t) = \begin{cases} f_o \sin(\pi t/\tau) & 0 \leq t \leq 2\tau \\ 0 & t > 2\tau \end{cases} \quad (6)$$

Figure 9 shows a suite of synthetic seismograms made for this time history with varying values of τ for the R_2 phase at NNA, with the observed waveform at the top of the Figure. The best fit of the overall period content of the data occurs for $\tau \sim 90$ s, so that the total duration of the source with the deceleration phase is 180 s. Figure 10

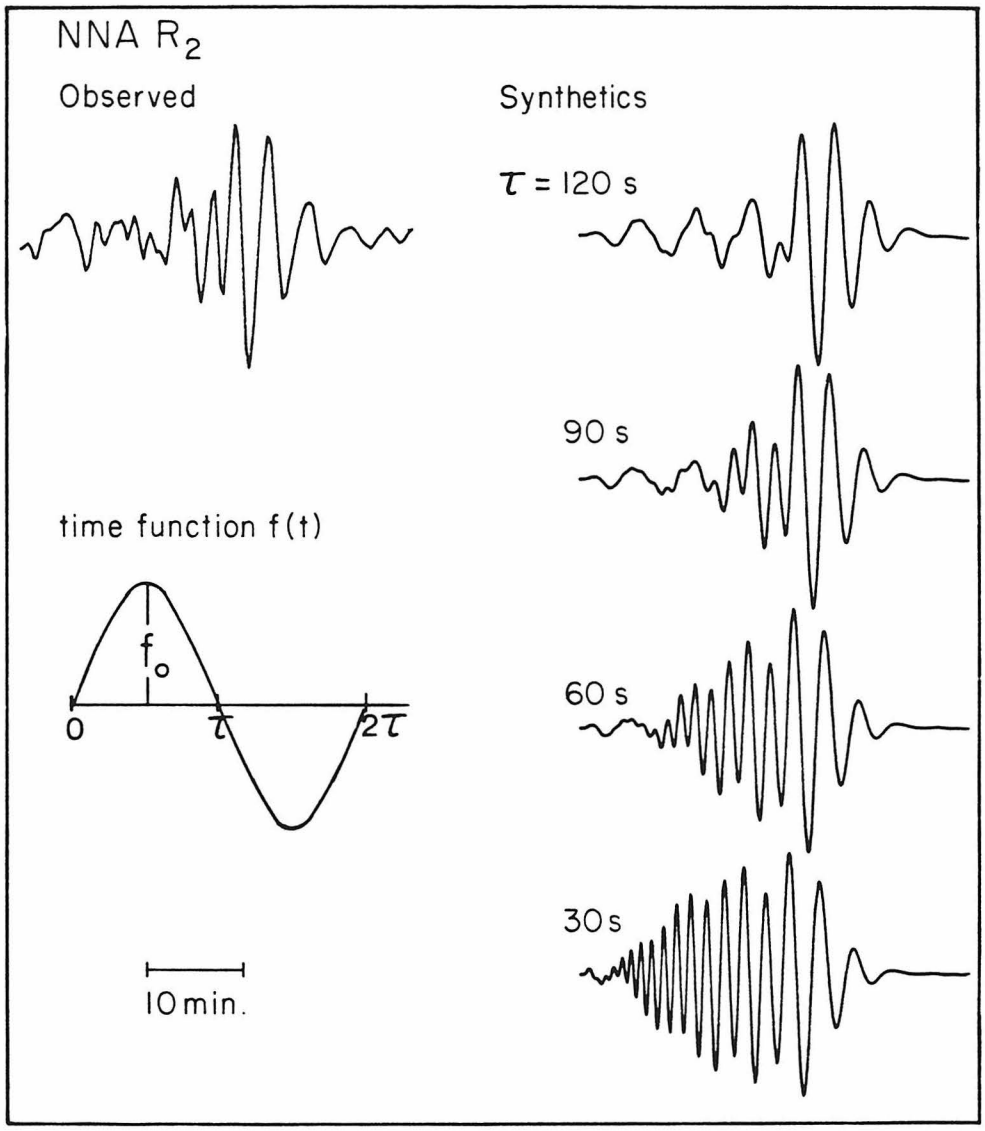

Figure 9. Comparison of the observed Rayleigh wave (R_2 passage) at the IDA station NNA, with a suite of synthetic seismograms made with the force time function shown, for varying values of the time constant τ. The best match occurs at $\tau = 90$ s.

shows that the assumed time history, with $\tau = 90$ s, is successful in matching the other observed Rayleigh waveforms as well. The peak force amplitude f_o can be obtained by comparing the amplitudes of the synthetic seismograms, made for a reference force size, to those of the observed records. The peak force amplitudes determined from the 4 waveforms are given in Table 3. The force sizes range from 1.1 x 10^{20} dyne to 2.0 x 10^{20} dyne. The average value is 1.6 x 10^{20} dyne, with a standard deviation of 0.3 x 10^{20} dyne. The higher values of f_o were obtained from the CAN phases, which is very close to the node, because the synthetic amplitudes are very small there; the values from NNA are considered more accurate. Note that this value of f_o is valid only if the event has the specific time dependence $s(t)$ assumed in the calculation; if the actual time history were different the estimate of f_o would change accordingly.

An independent estimate of f_o can be obtained from the observed Love wave spectral amplitudes found in the previous Section. The theoretical source spectrum of Love waves, $\hat{V}_\phi(\omega)$, for a unit force and a step time dependence is given by Equation 2. The theoretical spectrum for a source with a different time dependence will be given by the product of Equation 2 with the transform of the time function. The Fourier transform of the Kalapana time function (Equation 6) is given by

$$\hat{s}(\omega) = 2\pi i \tau \frac{\sin\omega\tau}{\pi^2 - (\omega\tau)^2} e^{-i\omega\tau} \qquad (7)$$

Equation 2 was evaluated for a period of 100 s, a source depth of 10 km, a time constant τ of 90 s, and the geometry inferred for the single force. The modulus was then multiplied by the modulus of Equation 7 with $\tau = 90$ s to arrive at the theoretical source amplitude of 100 s waves for a source with the time history in Equation 6. (A factor of ω is needed to convert Equation 2 into a delta function time dependence).

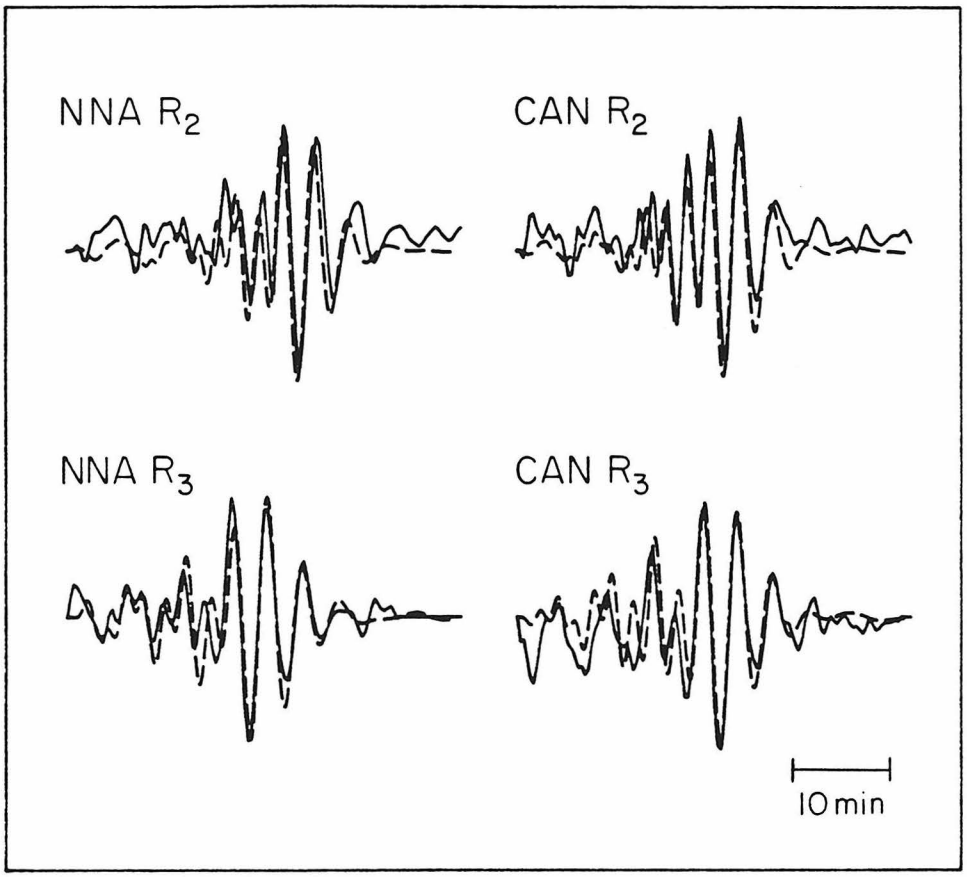

Figure 10. Synthetic (dashed) and observed seismograms for R_2 and R_3 passages at both IDA stations with $\tau = 90$ s. The vertical scale is arbitrary.

We compare the theoretical value at the radiation maximum (.027 cm s at 60^o for an assumed unit force size of 1 x 10^{18} dyne) with that from the observed Love wave pattern (approximately 2.5 cm s at 60^o ; see Figure 8). The resultant peak force size f_o is 9.3 x 10^{19} dyne, in good agreement with the average value of 1.6 x 10^{20} dyne determined from the Rayleigh wave data. The force estimates from the Rayleigh wave data were biased upward because the stations were preferentially distributed near the node, whereas the Love wave estimates are derived from a more uniform azimuthal distribution, so that we prefer the lower value of $\sim$ 1 x 10^{20} dyne as the more reliable estimate of the peak force size. Thus from the long-period surface wave data, the peak force size involved in the Kalapana event can be constrained to be of the order 1 x 10^{20} dyne, with an overall duration of about 3 minutes. In comparison, the peak force from the Mt. St. Helens event was $\sim$ 1 x 10^{18} dyne.

The source spectrum for Rayleigh waves excited by a single force source with time function $f_o\, s(t)$ is given by

$$\hat{V}_r(\omega) = \frac{ir_s}{N} P_R{}^{(1)} \omega f_o\, \hat{s}(\omega) \left[\frac{\sin\alpha}{N} \frac{y_1(r_s)}{y_3(r_s)} + i\cos\alpha\cos\phi \right] \tag{8}$$

where $P_R{}^{(1)}$ is the excitation function given in Kanamori and Given (1981). For the Kalapana earthquake the force is near horizontal ($\alpha \sim 0$), so

$$\hat{V}_r(\omega) \approx -\frac{r_s}{N} P_R{}^{(1)} \omega f_o\, \hat{s}(\omega)\cos\phi \tag{9}$$

Thus the amplitude spectrum of the time function is given by

$$| f_o\, \hat{s}(\omega) | \approx | \frac{\hat{V}_r(\omega) N}{\omega r_s P_R{}^{(1)}} \frac{1}{\cos\phi} | \tag{10}$$

We can check the assumption for the time function of the Kalapana earthquake by comparing the right hand side of Equation 10 with the modulus of Equation 7. The factor $| \hat{V}_r(\omega) |$ is obtained from the observed spectra as shown in Equation 3, with the values of Q and U now being those of the spheroidal modes. We calculated $| f_o \hat{s}(\omega) |$ from Equation 10 using the NNA R_2 and R_3 phases. These are shown with the amplitude spectrum of the assumed force time history at $\tau = 90$ s in Figure 11. The CAN record was not used due to its nodal nature. Although the R_2 and R_3 curves are plotted on the same vertical scale, and should be equal since all propagation effects are removed, the vertical scale for the assumed force spectrum is arbitrary. The observed spectra generally match the shape of the assumed spectrum, which varies with ω as $\frac{\sin\omega\tau}{\pi^2-\omega^2\tau^2}$. However, even within the extended band range of the IDA data (Figure 11 shows spectra from periods of 105 s to 628 s), we see only a limited portion of the amplitude spectra of the assumed force history. Theoretically, because the slide mass has no final velocity, the time integral of the force $f_o s(t)$ over the duration of the event should equal zero. The time function need not have the simple form assumed in the modeling to meet this criterion; for example, the deceleration phase could have a longer duration and smaller peak amplitude. In any case, however, the source spectrum should go to zero at zero frequency. This is not the case for the double-couple source, where the source spectrum has a non-zero value at zero frequency, which is the seismic moment M_o.

A trend toward zero at long periods is difficult to see in Figure 11 because the spectrum of the assumed force with $\tau = 90$ s is so broad; for example, the spectral amplitude does not fall to 1/3 its maximum value until T $\sim$ 900 s. However, the observed spectra suggest the beginning of a downward trend at longer periods, and the overall match with the assumed spectrum in general corroborates the choice of

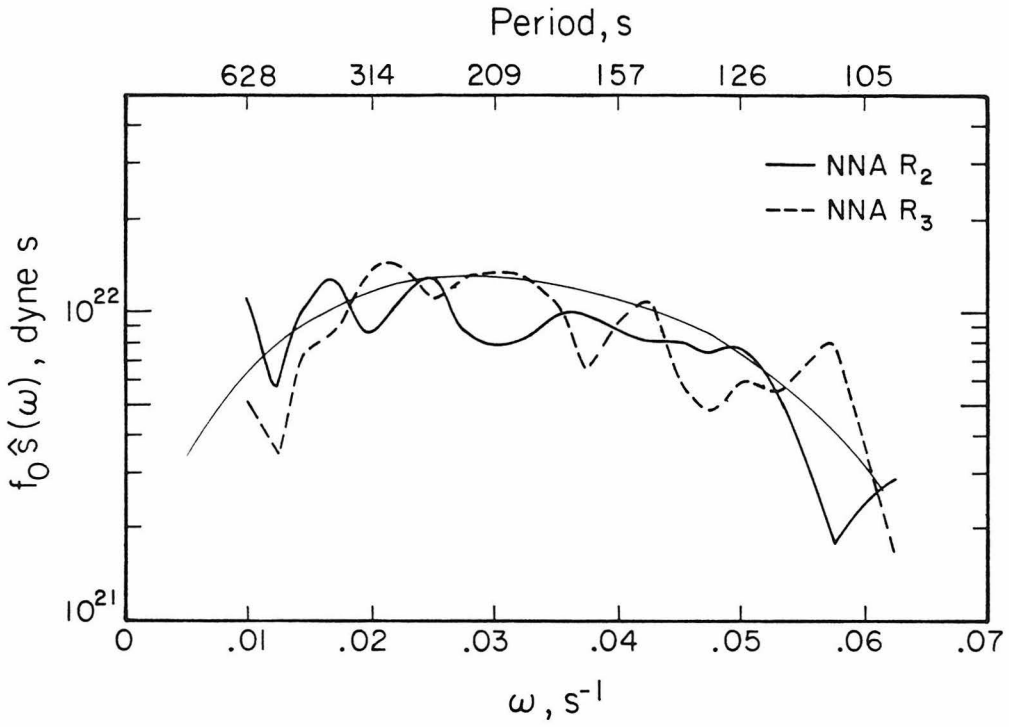

Figure 11. Amplitude spectra of the force time history retrieved from the R_2 (solid) and R_3 (dashed) passages at NNA, compared with the amplitude spectrum of the force time history assumed in the modeling (thin line).

the time dependence in Equation 6. The peak value achieved by the observed force spectra is $\sim$ 1.3 x 10^{22} dyne s. Kanamori and Given (1982) found a peak spectral amplitude for the Mt. St. Helens landslide of 5 x 10^{19} dyne s, approximately 260 times smaller.

4. Discussion

Geologic Evidence for Repeated Slumping on the Hawaiian Ridge

The occurrence of very large-scale seaward slides of unbuttressed volcanic slopes has been generally acknowledged for many years by geologists working on Hawaii, even before the example of the Kalapana earthquake (for example, Stearns, 1966; Moore and Fiske, 1969; Swanson et al., 1976; Tilling et al., 1976; Fornari et al., 1979; Lipman, 1980; Macdonald et al., 1983). The fault systems that flank the Hawaiian volcanoes are thought to mark the heads of large slump blocks that extend into the sea. On Hawaii, bathymetric mapping reveals submarine slumps several tens of kilometers wide offshore both the Hilina fault system of the south flank of Kilauea and the Kealakekua fault system of the west flank of Mauna Loa (Moore and Peck, 1965; Normark et al., 1978). The normal-fault systems together with the volcanic rift zones provide partial detachment of the lower slope block from the rest of the volcanic edifice. The Kaoiki normal-fault system on the southeast flank of Mauna Loa shows well-developed pali, some of which are draped by lava flows several thousand years old, suggesting that the Kaoiki pali were built predominantly by the same slumping process before the development of Kilauea when the Mauna Loa slope was still

unbuttressed (Lipman, 1980). Moore (1964) reported two giant submarine landslides offshore other islands of the Hawaiian Ridge, the first off the northeast slope of Oahu, 50 km wide by 160 km long, and the second off Molokai, 50 km wide by 80 km long.

Slumping as a Seismic Event

We raise the question of whether the events that build the massive slump features observed on the Hawaiian Ridge happen on the timescale of seismic events, or by slower, non-seismic creeping or flowing deformation. After the Kalapana earthquake, several researchers asked whether a standard "tectonic" (i.e., elastic dislocation) event could have produced the large tsunami and observed displacement, or whether they were actually produced by landsliding motion triggered by an earthquake. To our knowledge, no study previously addressed the question of whether the seismic radiation itself was caused by landsliding motion, i.e. whether the event could be represented by a different force system at the source. Apart from arguments about the scale of coseismic displacement or time durations possible in a moderate sized double-couple elastic dislocation source, the distinguishing criteria between the single force and double couple sources must come from the dynamic wave fields. The Love wave excitation is one of the best discriminators. The Love wave radiation pattern found above shows that the long-period waves are inconsistent with the double-couple source but fit the single-force source, and that the force is near-horizontal and northwestward, the expected orientation for seaward motion of the south flank on a low-angle plane. Further, the same force magnitude explains both the Love and Rayleigh wave amplitudes, and as we show later, this magnitude is roughly consistent with the estimated mass involved in the slump event. The source time function of the

Kalapana earthquake may have an acceleration and deceleration phase, as was discovered for the Mt. St. Helens landslide. The teleseismic focal mechanism shows one high-angle nodal plane, which is consistent with a near-horizontal single force, indicating that the initial motion could be due to spontaneous slumping. On the other hand, the fault plane solution from the local network may indicate a double-couple solution, but this is not necessarily inconsistent with an overall, long-period single-force source. In the first seconds of the event, a confining stress exists locally and the elastic properties of the upper block are initially important in the seismic radiation.

From their estimates of seismic moment, Ando (1979) calculated a fault slip of 3.7 - 5.5 m, and Furumoto and Kovach (1979) calculated a smaller fault slip of 1.4 m. The observed coseismic surface displacements were 3 m subsidence and 8 m horizontal seaward extension (Lipman et al., 1985). However the horizontal value increased steadily over the south flank from 1 m at the summit of Kilauea to 8 m at the coast and probably reached its maximum undersea, as implied by the accompanying tsunami. It would be difficult to produce the observed surface deformations, especially the horizontal value, by elastic response to a fault offset of a few meters, particularly if the extension continued to grow offshore.

Studies of the tsunami associated with the Kalapana earthquake also provide evidence for the single force source. Cox (1980) inferred, from differential arrival times of the tsunami throughout the Hawaiian Islands, that the seafloor displacement did not reach its maximum until several minutes after the origin time of the earthquake, consistent with the long time constant found from the surface wave modeling. The displacement occurring from a conventional earthquake of this magnitude would take place in several seconds, not minutes. Ando (1979) found that the maximum seafloor uplift resulting from the fault model is .5 m, which is too small to explain the

observed tsunami amplitude. Hatori (1976) also noted that the tsunami magnitude was anomalously large compared to the earthquake magnitude. These observations imply that a process other than the seafloor deformation caused by motion on a buried fault was involved in the generation of the tsunami.

The 1929 Grand Banks, Canada Earthquake

The magnitude 7.2 earthquake that occurred in 1929 on the Atlantic continental slope near Grand Banks, Newfoundland, Canada is well known for causing breaks in ocean bottom communication cables up to 450 miles seaward of the epicenter. The delay time between the earthquake origin time and the cable breaks systematically increased with distance from the epicenter, leading to the conclusion that the cable breaks were caused by a large turbidity current (suspension flow) induced by the earthquake (Heezen and Ewing, 1952). However within a distinct area up to 100 km seaward of the epicenter, the cable breaks occurred within one minute of the earthquake. Heezen and Drake (1964) differentiated the breaks in this region as being due to sediment slumps and landslides and not the turbidity current. The area experiencing the quick breaks is about 100 km x 150 km. With seismic reflection profiling, they found several subsurface inclined disrupted boundaries in this region, with a major surface that they identified as the primary sole of the slump about 1 km under the ocean bottom. Hasegawa and Kanamori (1986) are currently investigating seismic records from the earthquake. Their initial results support a near-horizontal single force source with an azimuth opposite the direction of slumping. Their estimate of the force size is the same order of magnitude as the source of the Kalapana event. The single force may also be a more appropriate source model for events designated

"tsunami earthquakes", whose long-period seismic radiation and associated tsunamis are anomalously large compared with their M_S magnitudes (Kanamori, 1972).

Inferred Source Parameters for the Kalapana Earthquake

From the seismic force time history found above, the acceleration of the slide block with mass M is

$$a(t) = \frac{f_o}{M}\left(\sin\frac{\pi t}{\tau}\right) \tag{11}$$

where f_o is approximately 1 x 10^{20} dyne. The velocity and displacement functions are then

$$v(t) = \frac{f_o \tau}{M\pi}\left(1-\cos\frac{\pi t}{\tau}\right) \tag{12}$$

$$x(t) = \frac{f_o \tau}{M\pi}\left(t-\frac{\tau}{\pi}\sin\frac{\pi t}{\tau}\right) \tag{13}$$

The forms of these functions are shown in Figure 12. If the deceleration phase of $a(t)$ has a more trailing form than the sine function, shown by the dotted line in Figure 12*a*, then $v(t)$ and $x(t)$ will also change as shown.

A range of the mass M of the slide block can be estimated from the dimensions of the tsunami source areas, which vary from 2200 km^2 (Hatori, 1976) to 700 km^2 (Cox, 1980). Ando (1979) estimated a range between 800 km^2 - 2000 km^2. If a wedge-shaped volume V extending to a slide plane at 7 km depth is assumed, with an effective density ρ_e of 1.7 g cm^{-3} to account for the buoyancy effect of the water, M ranges from 4 x 10^{18} g to 1.3 x 10^{19} g. If the slide is a more superficial feature with a

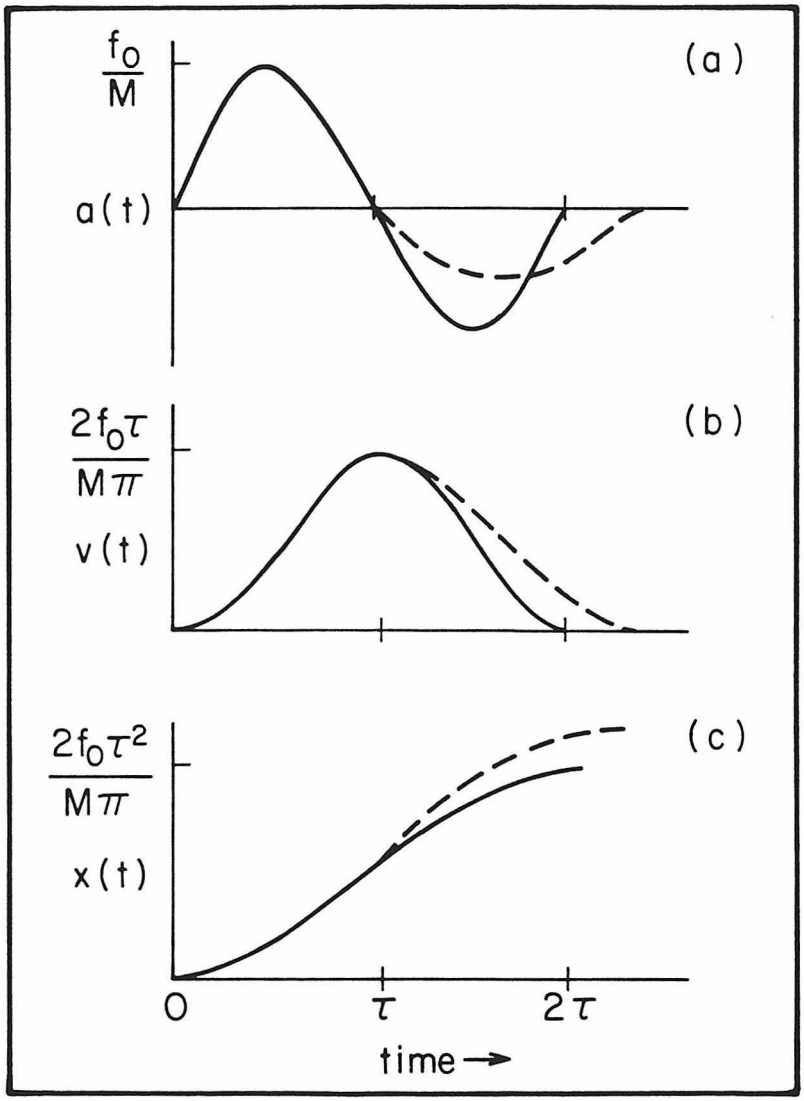

Figure 12. (*a*) Acceleration history of the slide mass corresponding to the assumed force time history. The dashed line indicates an alternative time history, where the deceleration phase is longer than the acceleration phase but the peak deceleration is smaller, so that the net time integral is zero. (*b*) Velocity function inferred from (*a*). (*c*) Displacement function inferred from (*b*).

thickness of 1 km, the mass range decreases to 6 x 10^{17} g - 1.9 x 10^{18} g. For comparison, the estimated mass of the Mt. St. Helens landslide was much smaller, 5 x 10^{15} g.

Using a mass range of 10^{18} - 10^{19} g, the peak acceleration for the slide mass inferred from the seismic force is 10 cm s^{-2} - 100 cm s^{-2}. This is comparable with the acceleration due to gravity on a gently inclined plane (85 cm s^{-2} for α=5^o). Assuming the functions for velocity and displacement in Equations 12 and 13 with τ = 90 s, the maximum velocity v_{max} of the slide is 5.7 - 57 m s^{-1} achieved at $t = \tau$. The final displacement x_{max} is 520 - 5200 m. The final displacement depends on the time constant τ as τ^2, so that if τ is somewhat smaller, say 50 s, the displacement for the larger mass estimate reduces to 160 m. These values imply that the bulk of the displacement took place undersea, and that the coseismic observations observed onland are a small manifestation of the larger downslope processes. The observed subaerial horizontal displacement increased from 1 m at the summit of Kilauea to 8 m at the coast and likely continued to increase undersea as the slide block deteriorated into a massive sediment slump. Although the entire event may have been initiated by a small tectonic earthquake caused by magmatic stresses, the bulk of the seismic radiation was produced by the gravitationally driven slumping process. The epicenter and aftershocks indicate that the initial event took place on the volcano - crust interface, which is lubricated with deep sea sediments to afford easy sliding and some decoupling. However, once the process developed, there was probably no longer one single slide plane. The south flank is composed of several kilometers thickness of bedded lava flows, affording many subsidiary slump planes. In the later stages of the event, we envision that the slide block, originally moving on the major detachment plane at 7 km depth and partially decoupled, loses its coherency as a unit and experiences internal failure on many

planes, eventually disintegrating into a massive rubble slide or flow to produce a complex and sustained seismic event.

5. Conclusions

The observed long-period seismic radiation associated with the Kalapana earthquake can be adequately modeled by assuming a single force for the seismic source as opposed to the double force couple. The force orientation determined by modeling the Love and Rayleigh surface waves is near-horizontal ($\alpha \sim 10^o$) with an azimuth of 330^o, opposite to the displacement direction observed onland. The time history of the force inferred from Rayleigh waves has a total duration of about 3 minutes. The peak force f_o determined from the surface wave amplitudes is about 1 x 10^{20} dyne. The force is interpreted to represent seaward slumping of a large massive partially decoupled block of the south flank of Kilauea on a shallow and near-horizontal plane.

The single force slumping model explains many of the observations of the Kalapana earthquake that are difficult to reconcile with the double-couple model, such as the following:

1. The observed Love wave amplitude radiation pattern is two-lobed in azimuth, not four-lobed as expected for the double-couple source. The theoretical Love wave pattern for the single force is two-lobed with its nodal direction perpendicular to the force direction.

2. The coseismic deformations observed onland are extremely large for an earthquake of this magnitude (3 m of subsidence and 8 m of seaward extension). The observed extension increased steadily seaward over the subaerial portion of the south

flank and must have continued to do so undersea. The single force predicts motions of tens to hundreds of meters, depending on the mass assumed and the time history of the source.

3. The amplitude of the tsunami associated with the Kalapana earthquake is large for the earthquake magnitude, and requires a larger seafloor uplift than would result from reasonable values of fault slip inferred from the double couple seismic moment. The tsunami source may have lasted several minutes, consistent with the single force time history.

4. The long period end of the observed source spectra suggest a trend toward zero at zero frequency as expected for the single force model because the slide block eventually comes to rest. The long-period end of spectra from elastic dislocation earthquakes should approach a static value, the seismic moment.

Geological studies of the Kalapana earthquake published to date basically accept the large scale slump model of the earthquake. In this study we have shown that most of the seismic radiation was produced by the slumping as well, and not by an elastic dislocation on a fault plane. From geological observations, large-scale slumping off volcanic slopes is a common mode of deformation for the Hawaiian Ridge, and could frequently take place as large-scale, single-force seismic events. Although the Kalapana seismic event may have been initiated by a small double-couple earthquake resulting from stresses associated with magmatic pressure in the east rift zone or an adjacent buried dike complex, the overall process was inherently gravitational. The single force may be applicable as a source model to other earthquakes as well, such as massive sediment slides on passive continental margins that are otherwise expected to be zones of low seismicity, or tsunami earthquakes.

--

Acknowledgements. We thank John Hoffman of the Albuquerque Seismological Laboratory of the U.S. Geological Survey for preparing a data tape of the Kalapana earthquake upon request. This research was supported by the Earth Sciences Division, National Science Foundation, grant EAR-8313223, and the Engineering Division, National Science Foundation, grant ECE-8303647.

References

Ando, M., The Hawaii earthquake of November 29, 1975: Low dip angle faulting due to forceful injection of magma, *J. Geophys. Res., 84*, 7616-7626, 1979.

Cox, D. C., Source of the tsunami associated with the Kalapana (Hawaii) earthquake of November 1975, *Hawaii Inst. Geophys. report 80-8*, 46 pp., University of Hawaii, Honolulu, 1980.

Crosson, R. S., and E. T. Endo, Focal mechanisms of earthquakes related to the 29 November 1975 Kalapana, Hawaii earthquake: The effect of structural models, *Bull. Seismol. Soc. Am., 71*, 713-729, 1981.

Fornari, D. J., J. G. Moore, and L. Calk, A large submarine sand-rubble flow on Kilauea volcano, Hawaii, *J. Volc. Geothermal Res., 5*, 239-256, 1979.

Furumoto, A. S., and R. L. Kovach, The Kalapana earthquake of November 29, 1975: An intra-plate earthquake and its relation to geothermal processes, *Phys. Earth Planet. Inter., 18*, 197-208, 1979.

Hasegawa, T., and H. Kanamori, Source mechanism of the magnitude 7.2 Grand Banks earthquake of November 1929: Double couple or submarine landslide?, in preparation, 1986.

Hatori, T., Wave source of the Hawaii tsunami in 1975 and the tsunami behavior in Japan (in Japanese), *Zisin, 2(29)*, 355-363, 1976.

Heezen, B. C., and C. L. Drake, Grand Banks slump, in *Geological Notes, Bull. Amer. Assoc. Petrol. Geol., 48*, 221-225, 1964.

Heezen, B. C., and M. Ewing, Turbidity currents and submarine slumps, and the 1929 Grand Banks earthquake, *Amer. J. Sci., 250*, 849-873, 1952.

Kanamori, H., Synthesis of long-period surface waves and its application to earthquake source studies — Kurile Islands earthquake of October 13, 1963, *J. Geophys. Res., 75*, 5011-5027, 1970.

Kanamori, H., Mechanism of tsunami earthquakes, *Phys. Earth Planet. Int., 6*, 346-359, 1972.

Kanamori, H., and J. J. Cipar, Focal process of the great Chilean earthquake May 22, 1960, *Phys. Earth Planet. Inter., 9*, 128-136, 1974.

Kanamori, H., and J. W. Given, Use of long-period surface waves for rapid determination of earthquake source parameters, *Phys. Earth Planet. Inter., 27*, 8-31, 1981.

Kanamori, H., and J. W. Given, Analysis of long-period seismic waves excited by the May 18, 1980 eruption of Mount St. Helens — A terrestrial monopole?, *J. Geophys.*

Res., 87, 5422-5432, 1982.

Kanamori, H., J. W. Given, and T. Lay, Analysis of seismic body waves excited by the Mount St. Helens eruption of May 18, 1980, *J. Geophys. Res., 89*, 1856-1866, 1984.

Lipman, P. W., The southwest rift zone of Mauna Loa: Implications for the structural evolution of Hawaiian volcanoes, *Amer. J. Sci., 280-A*, 752-776, 1980.

Lipman, P. W., J. P. Lockwood, R. T. Okamura, D. A. Swanson, and K. M. Yamashita, Ground deformation associated with the 1975 magnitude-7.2 earthquake and resulting changes in activity of Kilauea volcano, Hawaii, *U.S. Geol. Surv. Prof. Pap., 1276*, 45 pp., 1985.

Macdonald, G. A., A. T. Abbot, and F. L. Peterson, *Volcanoes in the Sea,*, 2nd ed., 517 pp., University of Hawaii Press, Honolulu, 1983.

Moore, J. G., Giant submarine landslides on the Hawaiian Ridge, *U.S. Geol. Surv. Prof. Pap., 501-D*, D95-D98, 1964.

Moore, J. G., and W. C. Albee, Topographic and structural changes, March-July 1980 — Photogrammetric data, in Lipman, P. W., and D. R. Mullineaux, editors, *The 1980 Eruptions of Mount St. Helens, Washington, U.S. Geol. Surv. Prof. Pap., 1250*, 844 pp., 1981.

Moore, J. G., and R. S. Fiske, Volcanic substructure inferred from dredge samples and ocean-bottom photographs, Hawaii, *Geol. Soc. Am. Bull., 80,* 1191-1202, 1969.

Moore, J. G., and D. L. Peck, Bathymetric, topographic, and structural map of the south-central flank of Kilauea volcano, Hawaii, *U.S. Geol. Surv. Misc. Geol. Invest., Map I-456,* 1965.

Nakamura, K., Why do long rift zones develop in Hawaiian volcanoes (in Japanese), *Kazan, 25,* 255-269, 1980.

Normark, W. R., P. W. Lipman, J. P. Lockwood, and J. G. Moore, Bathymetric and geologic maps of Kealakekua Bay, Hawaii, *U.S. Geol. Surv. Misc. Field Studies, Map MF-986,* 1978.

Rojahn, C., and B. J. Morrill, The Island of Hawaii earthquakes of November 29, 1975: Strong-motion data and damage reconnaissance report, *Bull. Seismol. Soc. Amer., 2,* 493-515, 1977.

Sipkin, S. A., Interpretation of non-double-couple earthquake mechanisms derived from moment tensor inversion, *J. Geophys. Res., 91,* 531-547, 1986.

Stearns, H. T., *Geology of the State of Hawaii,* Pacific Books, Palo Alto, Ca., 1966.

Swanson, D. A., W. A. Duffield, and R. S. Fiske, Displacement of the south flank of Kilauea volcano: The result of forceful intrusion of magma into the rift zones, *U.S. Geol. Surv. Prof. Pap., 963*, 39 pp., 1976.

Tilling, R. I., R. Y. Koyanagi, P. W. Lipman, J. P. Lockwood, J. G. Moore, and D. A. Swanson, Earthquake and related catastrophic events, Island of Hawaii, November 29, 1975: A preliminary report, *U.S. Geol. Surv. Circ., 740*, 33 pp., 1976.

Chapter 3

Investigation of Global Seismic and Atmospheric Signals Associated with Explosive Volcanic Eruptions

Abstract

Far-field seismograms were searched for signals associated with recent large volcanic eruptions to examine whether models of the volcano as a seismic source derived from the Mt. St. Helens data set are applicable to other explosive volcanoes. Except for Mt. St. Helens, very few of the explosive eruptions that have occurred since deployment of improved instrumentation in the late 1970's have been large enough to produce globally recorded seismic signals. We found that the 1982 eruption of El Chichón in Mexico produced long-period Rayleigh waves and body waves that were marginally recorded at IDA and SRO stations less than 40^{o} from the volcano. Still, several characteristics of the eruption can be inferred from the seismic waves: the third explosive phase of three at El Chichón was the largest, but an order of magnitude smaller than Mt. St. Helens as a seismic source; seismic radiation was azimuthally symmetric, unlike Mt. St. Helens; and all three phases involved about 30 min of sustained explosive activity. Near-field seismograms of smaller explosive eruptions at Mt. Asama, Japan were examined. These explosions were comparable in size to the smaller secondary eruptions of Mt. St. Helens, and appear to have a more complicated seismic source, which may involve concurrent tectonic stress release. Atmospheric waves recorded on barographic instruments from the explosive eruptions of Krakatau (1883), Bezymianny (1956), and Mt. St. Helens (1980) are compared and show differences in signal duration, amplitude, and characteristic period that are indicative of the overall size of the eruption. A preliminary model of air wave excitation from a volcanic eruption where the source strength is proportional to the outflow of volcanic products was applied to air waves from Mt. St. Helens, and is successful in explaining some aspects of the observed record.

1. Introduction

With the eruption of Mt. St. Helens volcano in Washington in May 1980, it became apparent that new high-gain long-period instrumentation developed in the 1970's could record seismic signals from an explosive volcano at teleseismic distances ($\Delta \geq 30^{o}$). Two important realizations were immediately made by the seismological community following this event: first, a kinematic source for the seismic radiation from an explosive volcano could be developed from the Mt. St. Helens data set, perhaps leading to a better understanding of the actual physical source; and second, far-field seismic recordings could serve as a potential quantification tool for explosive volcanic eruptions. Toward the first end, seismic records of the eruption of Mt. St. Helens were extensively analyzed by Kanamori and Given (1982, 1983), Kanamori et al. (1984), and Burger and Langston (1985). A surprisingly simple picture of the kinematic source emerged: the seismic radiation could be explained by a combination of a single horizontal force, caused by the landslide that accompanied the eruption, and a series of shorter-period vertical forces describing the volcanic blasts or explosions. By specifying a source model, in this case the vertical single force, the researchers also specified parameters such as force magnitude and duration that could be retrieved from seismic data and used to quantify, or at least relatively rank, different explosive volcanic eruptions.

Previously, volcanological observations had fallen into two basic groups: classical descriptive geological field studies of volcanic ejecta such as air fall tuff, volcanic bombs, and lava flows, which provide evidence for the total mass of erupted products, eruption rates, and ejecta velocity; and petrological studies of eruption products, which give clues about initial conditions in the magma chamber such as temperature

and pressure. Seismic observations of volcanoes are common, but aside from Mt. St. Helens, they consist of very near-field, short-period ($\sim$ 1 Hz) recordings. Frequently, the recorded seismic signal is "volcanic tremor", a fairly monochromatic signal with an unclear beginning or end that can endure steadily for many hours while an eruption is taking place, or even without a surface eruption. Volcanic tremor is thought to be the signature of magmatic motion or unrest within the magma chamber. This type of signal is seen with both explosive and non-explosive eruptions, such as the Hawaiian volcanoes. Another near-field seismic signal associated with volcanoes has created the term "volcanic earthquakes". These are different from volcanic tremor in that, like conventional earthquakes, they have a short duration and clearer onset, but they are unusual in that they are longer period than tectonic earthquakes in the same region and show depleted S wave radiation, presumably indicating wave propagation through a highly fractured or partially molten region, or failure in a region with lower shear strength. Atmospheric waves (basically, pressure waves of very low frequencies) have been seen globally in concurrence with the largest, most explosive eruptions; they are usually noted as an oddity on weather barographs, and only rarely analyzed quantitatively.

The size or energy of a volcanic eruption has been approached by considering potential and kinetic energy of the ejecta, the thermal energy of eruption products, including gas expansion, the volume or mass of erupted material, and less frequently, the energy involved in radiated seismic, atmospheric, and tsunami waves (e.g., summaries include Yokoyama, 1956, 1957; Gorshkov, 1960; and Hedervari, 1963; there are also many other energy estimates published in studies of individual eruptions). One problem encountered in the study of explosive volcanoes is that they often occur in extremely remote areas, and unlike earthquakes, there are few remote quantification

methods for volcanic explosions. Observations can be further impaired by inaccessibility to the area immediately following an eruption due to the danger imposed by mudflows, pyroclastic ash flows or nueé ardentes, or impending explosions. Further, the volcano can be masked from observers by heavy ash fall or severe weather conditions.

In this chapter, we describe work undertaken to expand the methods developed for Mt. St. Helens to other volcanoes, and to explore the possibility of quantification of explosive volcanic eruptions via their radiated seismic and atmospheric waves. Although we test the applicability of the vertical single-force source to other explosive volcanoes, we do not attempt to devise alternative source models. A large part of the work was simply to attempt to compile a data set by searching for long-period far-field seismic signals from large explosive eruptions, which was frequently a frustrating process. The last eruption of comparable explosivity to Mt. St. Helens occurred in 1956, before the advent of even the WWSSN seismic network. Table 1, compiled from information in Simkin et al. (1982) and the *SEAN Bulletin*, shows recent volcanic eruptions with a "Volcanic Explosivity Index" (VEI) of 4 or greater. The VEI scale was concocted by Newhall and Self in 1982, and was meant to be a crude measure of explosive power as inferred from observations such as volume of ejecta, eruption column height, inferred muzzle velocity, and overall violence or destructive potential. Many of the larger (VEI = 4) eruptions in Table 1 occurred before standardized operation of the GDSN (Global Digital Seismic Network, including SRO, ASRO, DWWSSN, and RSTN stations) and IDA (International Deployment of Accelerometers) networks that recorded Mt. St. Helens. Mt. St. Helens was recorded on some WWSSN stations, which are lower gain and shorter period than GDSN stations, but not at distances beyond 40^o (Burger and Langston, 1985). Eruptions with VEI = 3

Table 1

Recent Large Explosive Volcanic Eruptions

Volcano Name	Location	Eruption Date	VEI[1]
Bezymianny	Kamchatka	March 30, 1956	5
Fernandina	Galapagos Islands	June 11, 1968	4
Tiatia	Kurile Islands	July 14, 1973	4
Fuego	Guatemala	October 10, 1974	4
Plosky Tolbachik	Kamchatka	July 6, 1975	4
Augustine	Alaska	January 22, 1976	4
Bezymianny	Kamchatka	February 11, 1979	4
Mt. St. Helens	Washington,USA	May 18,1980	5
El Chichón	Mexico	April 4, 1982	4
Galunggung	Indonesia	April 8,1982	unassigned
Mt. Asama	Japan	March 10, 1973	3
Ngauruhoe	New Zealand	January-March 1975	3
Negra	Galapagos Islands	November 13, 1979	3
Mt. Asama	Japan	April 25, 1982	unassigned

[1] Volcanic Explosivity Index, from Newhall and Self (1982).

are listed in Table 1 only if they are very close ($\Delta \leq 6^o$) to a station. Unfortunately, only two eruptions in Table 1 aside from Mt. St. Helens generated recognizable seismic signals: El Chichón in Mexico was recorded because of its occurrence after the availability of higher quality data, but only with very small amplitudes; and Mt. Asama in Japan, due to its fortuitous location 33 km from a WWSSN station.

In the following Sections, we discuss seismic investigations of Mt. St. Helens, El Chichón in 1982, and Mt. Asama, in 1973 and 1982. In addition, we discuss implications of the atmospheric waves arising from explosions of Krakatau (1883), Bezymmiany (1956), El Chichón, and Mt. St. Helens. This study is by no means meant to be a complete work on the source of waves associated with volcanic blasts. Aside from presenting preliminary results of our investigations, our primary goal is to establish a foundation that can be used by other researchers as higher quality data become available in the future, eventually leading to a better understanding of the seismic source of and quantification of volcanic explosions.

2. Proposed Source of Seismic Radiation

As the source of seismic radiation from a volcanic explosion, we assume the single force used by Kanamori et al. (1984) and Kanamori and Given (1983) to successfully model seismograms from the eruption of Mt. St. Helens. The model is shown schematically in Figure 1. The basic mechanism of this source is the sudden removal of a lid from a pressurized magma chamber and the ensuing relaxation of the sides and walls of the chamber due to the release of pressure. Before the lid is removed, forces are exerted on the sides, top, and bottom of the chamber by the fluid or gas

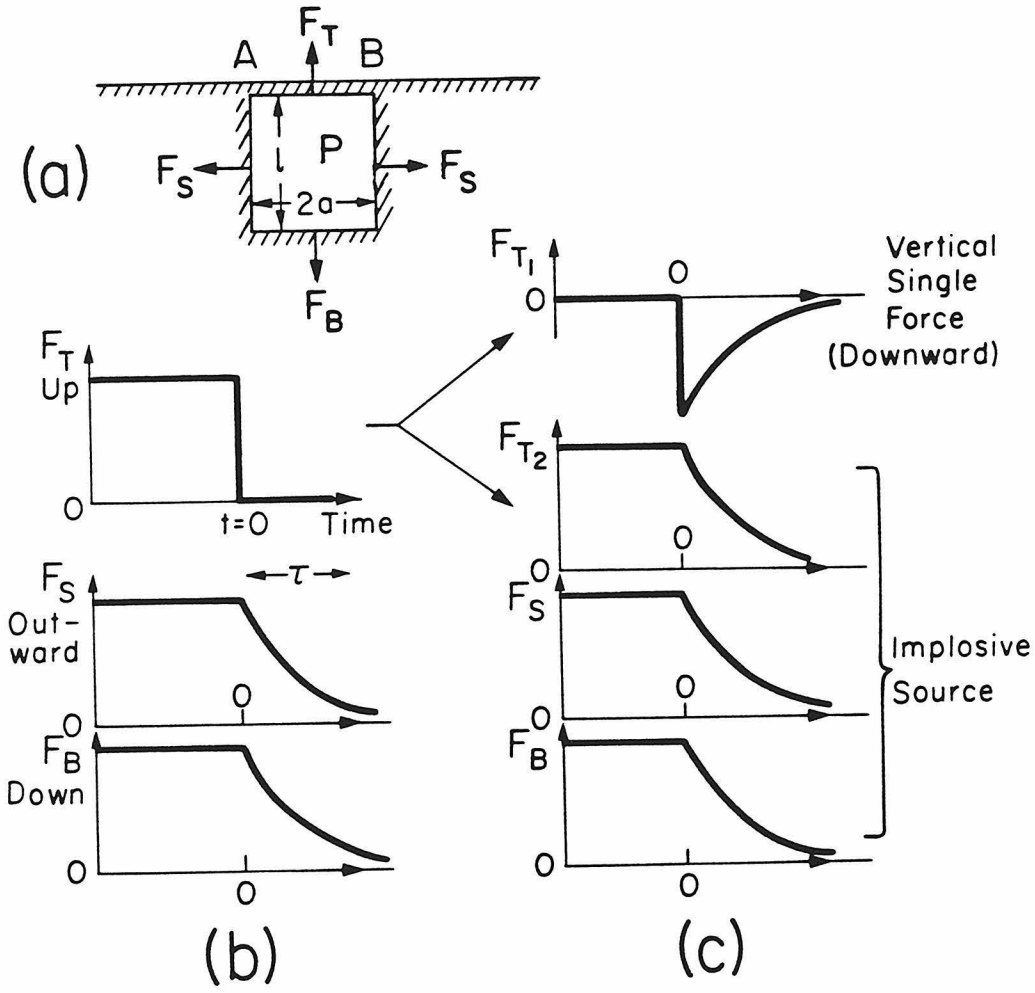

Figure 1. Equivalent force system used to represent an explosive volcanic eruption, from Kanamori et al. (1984). (*a*) Chamber with forces acting on the walls due to a gas or fluid under pressure. (*b*) Decay of forces to zero upon removal of lid AB. (*c*) Decomposition of forces in (*b*) to a vertical single force representing the thrust of the eruption and an isotropic implosive source.

under pressure (Figure 1*a*). While the upward force on the lid goes to zero instantaneously at the time of the explosion, the outward and downward forces on the sides and bottom of the chamber decrease to zero more slowly as the volcanic products exit (Figure 1*b*). The time constant is roughly l/v, where l is the characteristic length of the chamber and v is the exit velocity of the gas or fluid. The instantaneously vanishing upward force can be decomposed into two components, as shown in Figure 1*c*, such that the total force system can be viewed as a downward (vertical) single force representing the thrust of the eruption, and an isotropic source of three equal orthogonal force dipoles, representing implosion of the cavity. Kanamori et al. (1984) show that in the far field, the amplitude of seismic radiation from the implosive source is small compared with that from the single force as long as the exit velocity v is small compared to the seismic wave velocity of the elastic medium. Since a realistic minimum far-field seismic velocity is about 3 km s^{-1} for S waves, and estimates of exit velocity of volcanic products are on the order of 100 - 400 m s^{-1}, the contribution of the implosive source can be ignored. Similarly, in the near field, the isotropic-vs-single force seismic wave amplitude ratio scales as l/r, where l is the chamber dimension and r is the source-to-station distance. Thus as long as the observer is several chamber dimensions from the volcano, the single force representation is appropriate.

Body Wave Radiation Pattern From a Single Force

Using the spherical coordinate system of Kanamori et al. (1984), the displacement field in a whole space from a single force of arbitrary orientation with time history $h(t)$ is given by

$$\begin{bmatrix} U_r \\ U_\theta \\ U_\phi \end{bmatrix} = \frac{1}{4\pi\rho r\,\alpha^2} h\left(t-\frac{r}{\alpha}\right) \begin{bmatrix} \sin\theta\cos\delta\cos\phi - \cos\theta\sin\delta \\ 0 \\ 0 \end{bmatrix} \tag{1}$$

$$+ \frac{1}{4\pi\rho r\,\beta^2} h\left(t-\frac{r}{\beta}\right) \begin{bmatrix} 0 \\ \cos\delta\cos\theta\cos\phi - \sin\delta\sin\theta \\ -\sin\phi\cos\delta \end{bmatrix}$$

where α, β, ρ, and r are the compressional velocity, shear wave velocity, density, radial coordinate respectively; δ is the dip of the force from horizontal, downward positive; and θ and ϕ are the angular coordinates where ϕ describes the azimuth between the force strike and observer. This equation describes the body wave radiation pattern, where U_r is the P wave response, and U_θ and U_ϕ are the SV and SH response respectively. For a purely vertical force (δ=90^o), the P wave radiation pattern is symmetric in azimuth and entirely compressional, and there is no radiation of SH waves. Thus the P and SH radiation patterns and relative amplitude ratios provide a discriminant for the force orientation. Although we expect 90^o to be the force dip for a volcanic explosion, occasionally a preferred geometry can develop such that the explosion is somewhat directed. This was observed at Mt. St. Helens, where the landslide failure uncapped the chamber asymmetrically, and for Bezimianny in Kamchatka in 1956 (Gorshkov, 1963). In this case, the single force is used as the seismic source by specifying a dip angle and direction. However if the dip angle deviates too much from vertical, the intuitive interpretation of the source in terms of the simple model in Figure 1 becomes unclear.

Surface Wave Radiation Pattern

Equations governing the surface wave radiation pattern for a single force of arbitrary orientation were given in Chapter 2. Figure 2 shows a schematic depiction of the radiation patterns of fundamental mode surface waves for two force orientations, purely horizontal and purely vertical. Theoretically for the vertical force, which we take to represent a volcanic blast, there are no radiated Love waves, and the Rayleigh wave pattern is azimuthally symmetric. Figure 2 also shows that an isotropic source (three orthogonal force couples) is basically indistinguishable from the vertical force in terms of fundamental-mode excitation. The isotropic source was eliminated from consideration in the Mt. St. Helens analysis because it predicts the excitation of higher-mode Rayleigh waves that were not observed.

Near-Field Radiation

Lamb (1904) showed that the response of a homogeneous elastic half space to a transient surface single force is dominated by a large pulse showing Rayleigh-like motion, preceded by small pulses traveling at the P and S velocities. This sequence is collectively called the Lamb pulse. In the near field, the largest amplitude phase observed from the single force source is the free-surface Rayleigh wave, preceded by much smaller P and S arrivals. As discussed below, Kanamori and Given (1983) observed Lamb pulses from secondary eruptions of Mt. St. Helens with a long-period digital seismograph $\sim$ 70 km from the volcano.

Impulse of Force

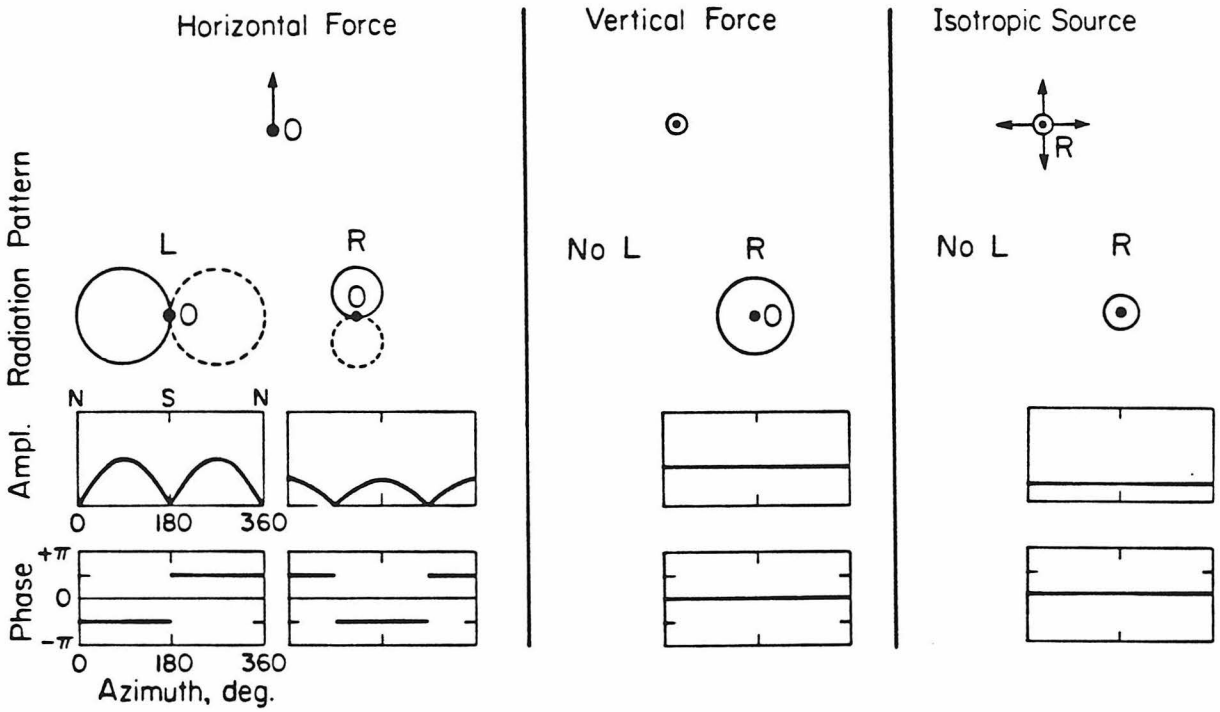

Figure 2. Sketch of azimuthal radiation patterns of fundamental-mode Rayleigh and Love waves from a horizontal force, vertical force, and isotropic source of three orthogonal force couples; from Kanamori and Given (1982).

In addition to the force geometry, we attempt to retrieve the amplitude and time dependence of the force to determine a ranking for the "size" of the explosive eruption as well as information about the timing of the eruption sequence. The source described above is for an instantaneous explosion. If a series of discrete explosions occurs, the force will have a time dependence $f(t)$. In this case the total contribution is the impulse $K = \int f(t)\, dt$. One parameter we will discuss is the peak magnitude f_o of the force time history achieved during the event; however two events can have the same f_o value with different time histories and thus different overall "sizes". The impulse is useful in source quantification because it includes the effect of duration or multiple events, and by mechanics can be related to the momentum of ejecta, $K = Mv_o$, and thus kinetic energy, $E_k = 1/2Mv_o{}^2$, where M is the ejecta mass and v_o the ejecta velocity.

3. Summary of Results from Mt. St. Helens

Far-Field Analysis

Long-period ($T > 200$ s) Rayleigh surface waves, and P and S body wave phases as well as shorter period Rayleigh and Love waves generated by the May 18, 1980 eruption sequence of Mt. St. Helens were globally recorded on ultra-long-period vertical instruments of the IDA network and three-component long-period instruments of the GDSN network respectively. This constituted the first teleseismic data set of an explosive volcanic eruption. Instruments of the WWSSN network, the dominant seismic network until the late 1970's, were not sensitive enough to record this

large volcanic event at teleseismic distances. In addition, atmospheric pressure waves from the explosion were recorded on weather barographs up to 400 km from the volcano, and globally on more sensitive microbarographs.

The seismic signals from this eruption have been analyzed by Kanamori and Given (1982, 1983), Kanamori et al. (1984), and Burger and Langston (1985). In the first study, Kanamori and Given (1982) found that the radiation pattern of long-period surface waves from the IDA network was unexplainable by any double-couple (earthquake) source, but could be explained by a single force with a near-horizontal dip and near-surface depth, striking approximately opposite in azimuth to the landslide that occurred simultaneously with the eruption on the north face of the volcano. This was the first well-documented observation of a single force seismic source in nature with modern global instrumentation, and was interpreted as the force produced on the Earth by the landslide block (see Chapter 2). Burger and Langston (1985)'s analysis reached the same conclusion using regional data between 8^o and 40^o recorded by the WWSSN network.

The first reports of the Mt. St. Helens eruption sequence reported that the landslide and ensuing eruption were initiated (triggered) by a $M_L = 5.2$ earthquake. Kanamori et al. (1984) studied body waves recorded at teleseismic distances to determine if an earthquake source could be separated from the longer-period landslide signals. They found that P waves at GDSN stations at widely distributed azimuths had the same (compressional) polarity, and that the SH/P amplitude ratio at all stations was very small, both of which are difficult to explain with either a double-couple source or the horizontal landslide source. A vertical single force was adopted to explain these observations, although the authors found that the force angle could be somewhat less, 70^o–80^o. The vertical force is taken to represent the seismic effect of

the volcanic blast on the Earth as discussed in Section 2. A time history of two groups of subevents roughly two minutes apart was resolved from the short period records, and was interpreted as two groups of explosions, consistent with infrared satellite recordings described by Moore and Rice (1983). Figure 3, from Kanamori et al. (1984) shows the time history and amplitudes of the vertical force (explosions) and horizontal force (landslide), together with the observed sequence of events.

Near-Field Observation of Lamb Pulse

One of the best examples of how a relative ranking of explosive size can be established from seismic records is that of the Lamb pulse observed from the major eruption of Mt. St. Helens compared with several of its smaller subsequent eruptions. Figure 4 shows records of the Lamb pulse from the main eruption with that from three secondary eruptions recorded by a long-period vertical DWWSSN seismograph at Longmire, Washington, 70 km away. The record from the main event is clipped and further complicated by the eruptive time history. As discussed above, the large pulse at the beginning of the records is Rayleigh wave motion. The large, long-period signal several minutes after the Rayleigh pulse is the air wave, recorded on the seismograph via buoyancy of the instrument mass as the local air density changes transiently during the passage of the wave. Figure 4 also shows the peak-to-peak amplitudes of the traces in digital counts; the trace amplitude of the main event is much larger than that of the secondary eruptions. By modeling the amplitudes, Kanamori and Given (1983) found a range in peak force amplitude from $\sim$ 1 x 10^{15} dyne for the smallest eruption to 2.6 x 10^{17} dyne for the main eruption. Table 2, from Kanamori and Given (1983), shows results from the analysis of Lamb pulses from the Mt. St. Helens

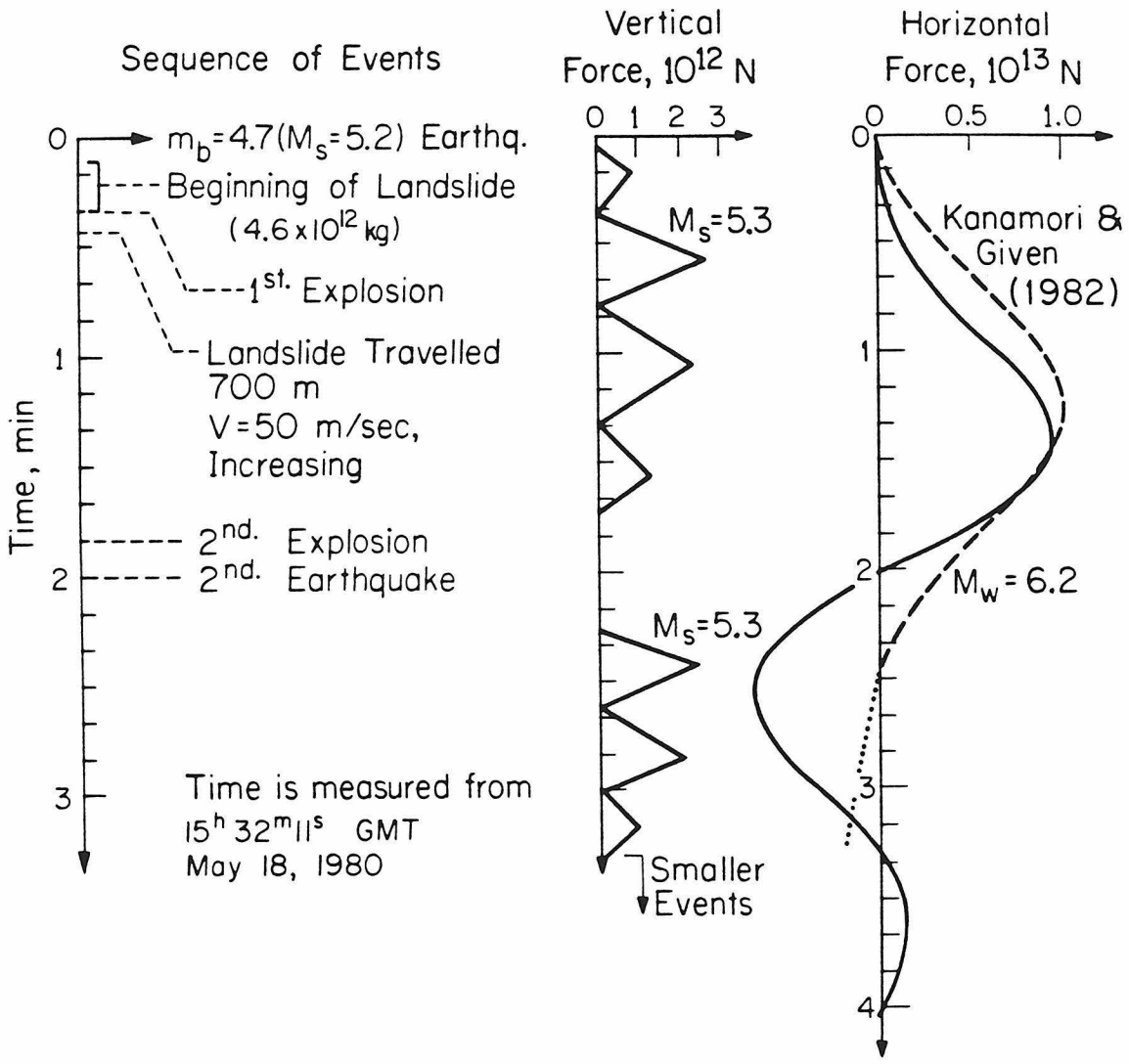

Figure 3. Histogram of events observed with the May 18, 1980 eruption of Mt. St. Helens, shown together with the time history of the vertical force inferred from teleseismic body waves, and the longer period horizontal force, which was caused by the large landslide that accompanied the eruption (taken from Kanamori et al., 1984).

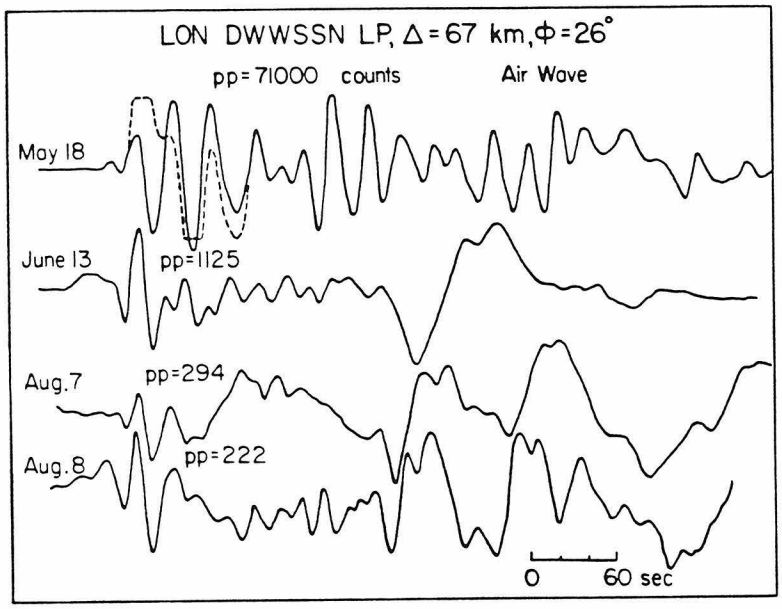

Figure 4. Seismograms of the main (top) and secondary eruptions of Mt. St. Helens recorded on the long-period vertical DWWSSN instrument at Longmire, Washington, 67 km from the volcano. The signal from the main event was retrieved from the intermediate-period channel where the long-period channel (dashed line) went offscale. The large pulse at the beginning of the records is the Rayleigh portion of the Lamb pulse. The signal from the main eruption has more complexity due to the time history of the source. The peak-to-peak amplitude in digital counts of the Rayleigh pulses are shown for each trace.

Table 2

Force Magnitude and Impulse Determined From
Lamb Pulse for Eruptions of Mt. St. Helens

Eruption	Peak Force, f_o, Dyne	Impulse, K, Dyne sec	Duration, τ, Sec
May 18	2.6×10^{17}	1.4×10^{19}	25
June 13	5.6×10^{15}	1.4×10^{16}	5
August 7	1.5×10^{15}	3.7×10^{15}	5
August 8	1.1×10^{15}	2.8×10^{15}	5

eruptions.

4. Seismic Observations of El Chichón, Chiapas, Mexico

Introduction

The volcano El Chichón, located at 17.33° N, 93.20° W in the southeastern state of Chiapas, Mexico, began an eruptive sequence with an initial explosion on March 29, 1982 and produced two equivalently large or larger episodes of sustained explosions on April 4. Incandescent ash avalanches completely buried two towns lying in valleys 6 and 8 km from the volcano and damaged others; estimates of casualties were at least 200 dead and 800 injured (Medina, 1982). The ash flows occurred in valleys at all directions around the volcano, indicating a symmetric eruption. Following the initial eruption on March 29, scientists from the National University of Mexico (UNAM) were in the area and provided ground observations of the two subsequent large eruptions on April 4 (De la Cruz Reyna, 1982). A six-station, short-period vertical regional seismic network had been operated in the area by the Federal Power Commission since 1980; the station nearest to El Chichón was 27 km. In addition, UNAM scientists deployed a field network around the volcano immediately after the first eruption (Haskov et al., 1983).

Little is known about the geologic history of El Chichón. Before the 1982 eruption, the volcanic cone was a heavily vegetated, relatively inconspicuous feature only 1300 m high. The first scientific survey to the area in 1930 reported fumarole activity and local seismicity, and fumarole activity and chemical alterations of groundwater

were again reported in 1981 (Medina, 1982); yet there are no reported historic eruptions of El Chichón in the Smithsonian Institution catalog of world volcanoes (Sipkin et al., 1981). The geological consensus is that the last eruptive activity was at least several hundred years ago and perhaps as much as hundreds of thousands of years ago (Medina, 1982).

Atmospheric Impact of 1982 Eruptions

Initial descriptions of the 1982 eruption implied that El Chichón was as large or larger than the climactic eruption of Mt. St. Helens, partially based on ground observations of violent explosions, but primarily from assessment of the atmospheric cloud associated with the eruption, as summarized by Pollack et al. (1983). The eruption columns from all three explosive phases penetrated the tropopause and introduced gas and particulate matter into the stratosphere, as observed clearly by NOAA weather satellites. The largest stratospheric effect was caused by the second April 4 eruption. Mt. St. Helens also penetrated the stratosphere to a roughly equivalent height (20-25 km). The stratospheric cloud from El Chichón was ranked as one of the most massive in this century, and was one order of magnitude denser than the Mt. St. Helens cloud. This is largely because the El Chichón cloud initially contained more sulfur, and sulfur-bearing particles and gas convert to sulfuric acid in the stratosphere, which is very stable there due to its small size and low sedimentation rate. It was estimated that the El Chichón cloud would cause a 2-3 % decrease globally in solar radiation at the Earth's surface, and would increase the temperature in the stratosphere by 3.5 K (Pollack and Ackerman, 1983).

Eyewitness and Near-Field Seismic Observations of Eruptive Sequence

The 1982 eruption consisted of three main explosive phases, beginning on March 29 at Approximately 05:32 GMT, April 4 at approximately 01:30 GMT, and April 4 at approximately 11:20 GMT. Reported times of eruption onset vary and are summarized in Table 3. In the gross sense, the three phases were of comparable size; they each impacted the stratosphere and caused widespread ashfall deposits. Descriptive observations generally hold that the last eruption on April 4 was the most powerful. The first eruption on March 29 only partially destroyed the summit cone, and local towns were impacted by air fall debris (De la Cruz-Reyna, 1982). The second eruption on April 4 began sharply with a series of violent explosions that endured for over 30 minutes. This eruption generated channeled hot ash flows in valleys with velocities of approximately 50 m s^{-1} that destroyed the towns of Francisco León and El Naranjo (Figure 5; Medina, 1982). Observers at Ostuacán, 12 km from the summit, reported that the lower part of the eruption column sustained by the explosions eventually collapsed to feed the flows (De la Cruz-Reyna, 1982). The third phase on April 4 occurred through a much widened vent and had the heaviest ash fall and largest eruption column, and also generated ash and pyroclastic flows. The Ostuacán observers reported sustained explosions and heavy bombardment with lithic pieces, although visible and audible observations were masked by the heavy ash fall. Table 4 compares gross parameters inferred for the three eruptions with those of Mt. St. Helens.

The third eruptive phase (April 4, $\sim$ 11:20 GMT) was deemed the largest from near-field short-period seismic observations (Haskov et al., 1983). Figure 6 compares portions of the short-period records of the three explosive phases from station CH3,

Table 3

Observed Start Times, Durations, and Near-Field Seismic Amplitudes of the Three Main Eruptions of El Chichón

Code	Date	Start Time, GMT	Duration, Min.	Peak-to-Peak Amplitude, mm.		Ratio to Event 94B
				Maximum	Average	
88	March 29	05:15[1] 05:32[2] 05:32[3]	32	60 (CH3) 28 (TPN)	20 (CH3) 9 (TPN)	0.45 (TPN)
94A	April 4	01:39[1] 01:35[2] 01:32[4]	31 30	70 (CH3) 32 (TPN)	25 (CH3) 6 (TPN)	0.30 (TPN)
94B	April 4	11:10[1] 11:30[2] 11:22[3] 11:20[5]	65 ~75	Clipped (CH3) 50 (TPN)	Clipped (CH3) 20 (TPN)	1.00

[1] Start time of near-field seismic signal, Haskov et al. (1983).

[2] Medina (1982); from ground reports.

[3] *SEAN Bulletin.*

[4] De la Cruz-Reyna, observer at Ostuacán (pers. comm.).

[5] Weintraub (1982).

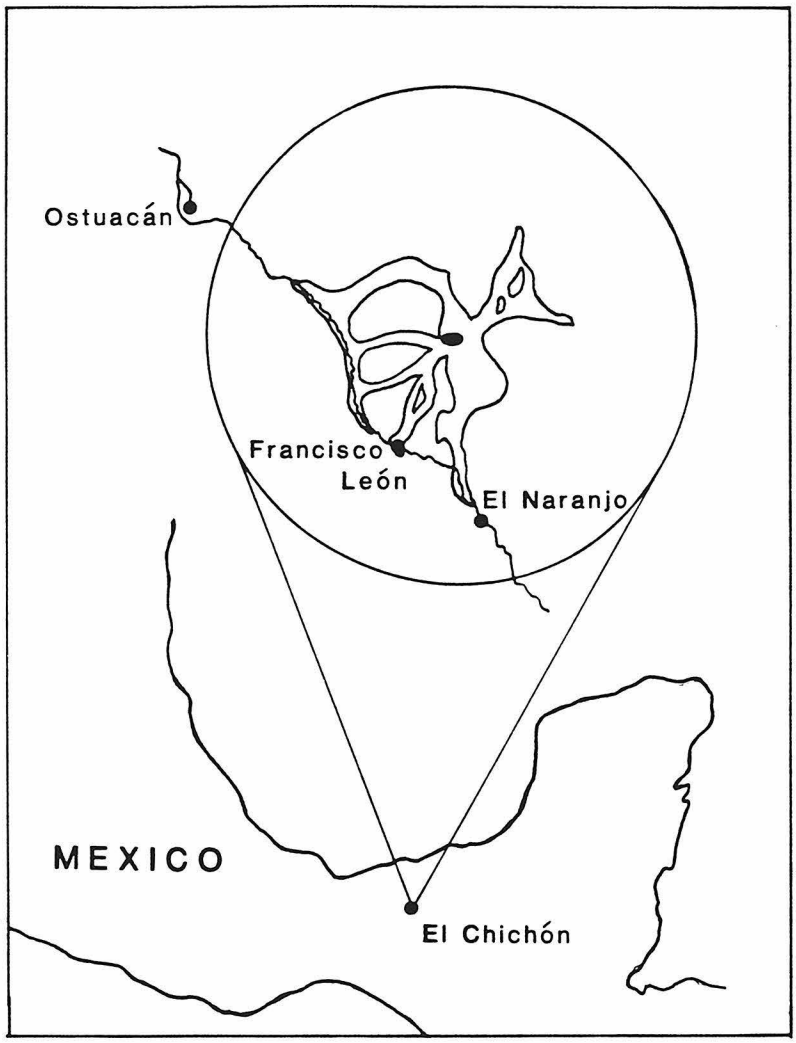

Figure 5. Location of El Chichón in Chiapas, Mexico, with a blow-up of the area (10 km radius) showing locations of ash flows following the third eruption, adapted from Weintraub (1982). Francisco León and El Naranjo were completely destroyed by the flows, Ground observers were located at Ostuacań, 12 km from the volcano on the Magdalena River, after the initial eruption.

Table 4

Comparison of Inferred Parameters of
the Three Eruptions of El Chichón and the Main Eruption of Mt. St. Helens

Eruption	Erupted Mass	Column Height
March 29 (88)	1.8×10^{11} kg	19.7 km
April 4 (94A)	1.2×10^{11} kg	21.2 km
April 4 (94B)	3.0×10^{11} kg	18.8 km
Mt. St. Helens	$\sim 6 \times 10^{11}$ kg	$\sim$ 20 km

[1] El Chichón values from Medina (1982).

[2] Mt. St. Helens values from Christiansen and Peterson (1981).

62 km from the volcano. The seismic signal accompanying the third eruption clearly has the longest duration. Table 3 compares peak and average trace amplitudes from Haskov et al. (1983) from the three eruptions at two near-field stations: CH3 and TPN, 27 km from the volcano but lower gain than CH3. The third eruption has the largest amplitude, the second eruption has the second largest, and the first eruption is smallest in terms of the short-period records.

Analysis of Far-Field Seismograms

Digital GDSN and IDA records were searched for seismic signals in time windows around the observed times of the three major eruptions. Signals associated with all three events were found at the stations listed in Table 5. Although each eruption was clearly recorded on at least a few stations, the data is far inferior to the Mt. St. Helens recordings in terms of seismic wave amplitude. We adopt the nomenclature of event 88 (after the Julian day), event 94A, and event 94B for the March 29, April 4 01:30, and April 4 11:20 eruptions respectively. Of the three events, we found that 94B had the largest far-field seismic wave amplitudes.

Long-period Rayleigh and air waves observed from event 94B. As an example of the far-field seismic signals from El Chichón, Figure 7 shows a record section compiled for event 94B. Records from three different instruments are shown in Figure 7, accounting for the difference in the character of the waveforms. Note that the distance axis of the record section is broken before and after the PFO record, and that the first two traces, ANM and ALQ, are from the same recording site (Albuquerque, New Mexico). The SRO and DWWSSN stations, which run at a sampling rate of one

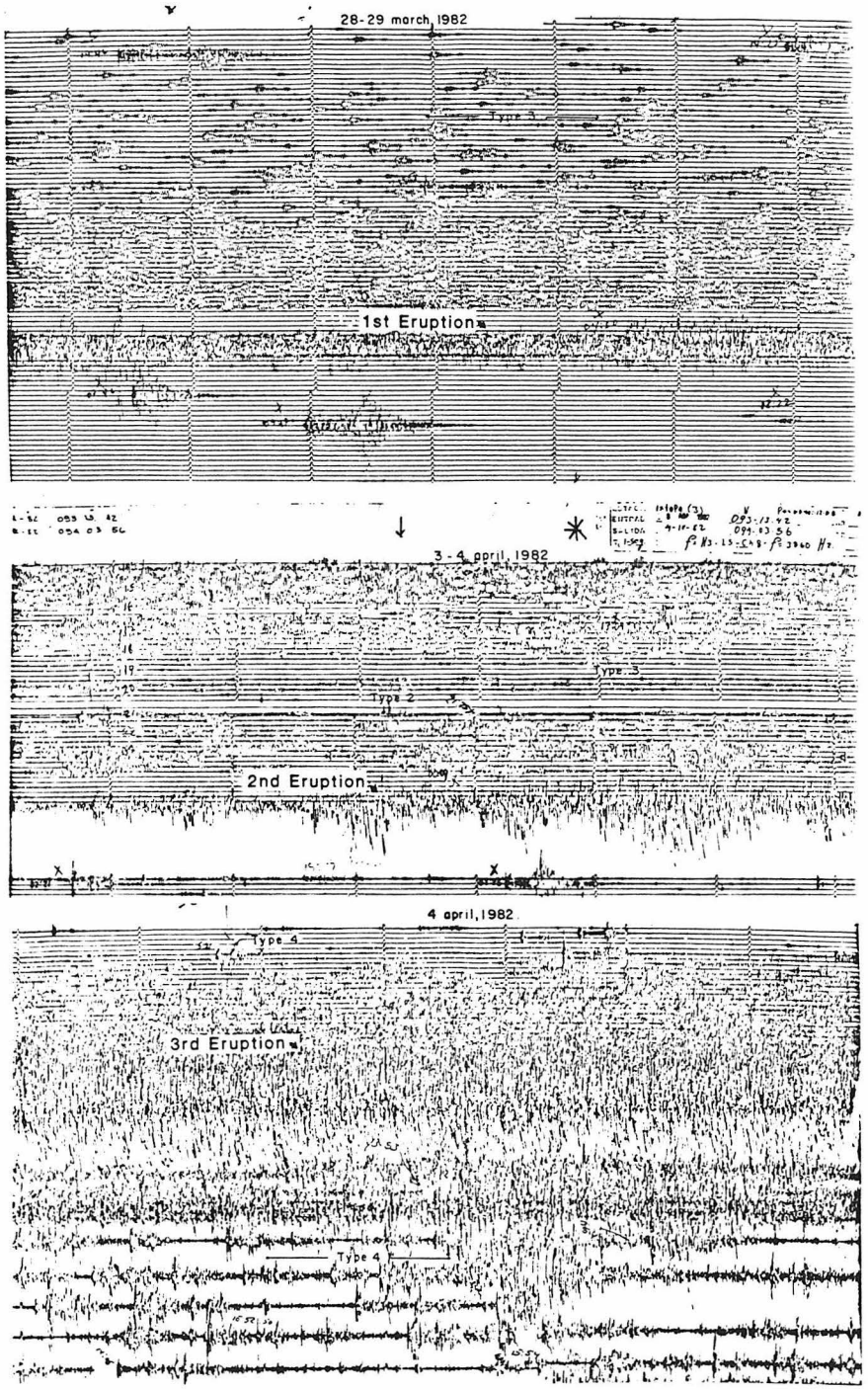

Figure 6. Portions of short-period vertical seismograms from station CH3, 62 km from El Chichón, showing seismic signal associated with the three eruptions. The instrument was shut off for a few hours following the second eruption, and was saturated for several hours following the third eruption, which was clearly the largest in terms of short-period seismic signal.

Table 5

Long-Period Far-Field Seismic Stations
Recording the Three Main Eruptions of El Chichón

Station	Network	Location	Distance, Deg.	Azimuth, Deg.	Phases Recorded: 94B	94A	88
ANM	SRO	Albuquerque, New Mexico	21.16° 2354 km	329°	*P,R*	*P,R*	-
ALQ	DWWSSN	Albuquerque, New Mexico	21.16° 2354 km	329°	*A* [1]	*A*	-
BOC	SRO	Bogota, Columbia	22.64° 2520 km	122°	*P ,R*	*P ,R*	-
PFO	IDA	Piñon Flats, California	26.43° 2940 km	312°	*R*	*R*	*R*
NNA	IDA	Naña, Peru	33.31° 3708 km	150°	*R*	*R*	*R*
HAL	IDA	Halifax, Canada	36.85° 4098 km	36°	*R*	*R*	*R*
LON	SRO	Longmire, Washington	37.67° 4189 km	327°	*A*	*A*	*A*

[1]Air wave.

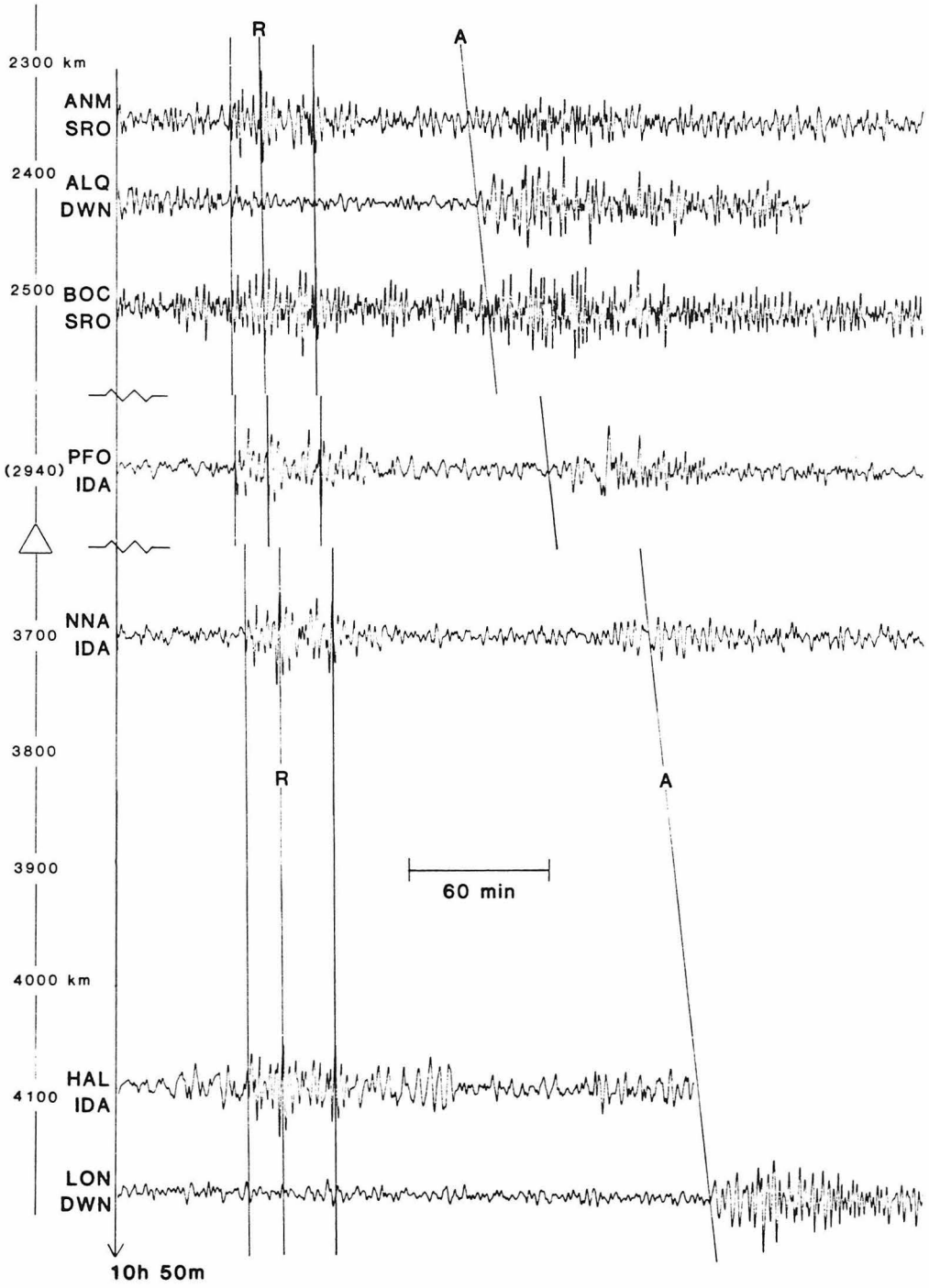

Figure 7. Record section compiled from SRO, DWWSSN, and IDA stations for the third eruption of El Chichón. The distance axis is broken before and after the PFO record. A wavetrain travelling with a Rayleigh velocity is apparent on the SRO and IDA instruments; the lines designated *R* are meant to show coherent features in the waveform that can be identified at each station. The long-period arrival later in the record marked *A*, most apparent on the DWWSSN records, is the air wave. The event was not recorded beyond LON.

point per second, have been low-pass filtered with a filter cutoff of 40 s period and decimated to a sample rate of one point per 10 s. The IDA records, whose sample rate is one point per 10 s, were high-pass filtered with a very large cutoff period (1 hr) to remove Earth tides. Because of the low sample rate and low-pass filtering, body waves are not apparent on the records in Figure 7.

There are two clear arrivals that correspond to an origin time around the reported time of the eruption. The first is a wavetrain enduring about 50 min and traveling with a Rayleigh wave velocity ($\sim$ 3.5 km s^{-1} for periods of $\sim$ 200 s). This wavetrain is extremely clear on the IDA records and apparent on SRO records but less obvious on the DWWSSN records. The lines designated R in Figure 7 are meant to show features in the Rayleigh wavetrain that can be correlated throughout the record section. The signal is very low amplitude, and not clear on DWWSSN records because these instruments are not as quiet as IDA and SRO instruments, which are longer period or deployed in 6 m deep boreholes. The Rayleigh signal was not seen at stations farther than HAL (Δ=36.9^o).

Line A on Figure 7 designates an arrival defined mainly by the DWWSSN records which has a much slower velocity of approximately .3 km s^{-1}. This is the expected velocity of the air wave (acoustic-gravity wave). The air wave is most apparent on the DWWSSN instrument because it is a surface instrument exposed to the atmosphere. Like the surface wave, the air wave from this eruption is extremely coherent at ALQ and LON and has a long duration ($\sim$ 1 hr). Although properties of air waves will be discussed in more detail in Section 6, the El Chichón records are presented here to give a qualitative comparison of the three eruptions.

Figure 8 shows sections of the Rayleigh and air wavetrains from event 94B in more detail. The IDA records have been equalized to the propagation distance of the

nearest record (PFO at Δ=26.4^o), and the HAL and NNA instrument responses were corrected to simulate the PFO response, so that the traces can be directly compared in terms of amplitude and waveform. The Rayleigh waveforms are remarkably similar; each shows a fairly long ($\sim$ 50 min) signal of predominantly 170-200 s waves with distinct features that can be identified at all three stations. Although the stations lie at different azimuths from the volcano, there is no indication of an amplitude variation with azimuth as there would be for a double-couple or non-vertical single force source.

The air waves recorded on the two DWWSSN instruments are also remarkably coherent, particularly in the first 30 min of signal. The traces were not equalized with distance for comparison because the atmosphere is largely non-dispersive at these periods (Press and Harkrider, 1962). The amplitude difference between ALQ and LON can be explained by the $1/\sqrt{\sin\Delta}$ factor that describes spreading of a cylindrical wave propagating over a sphere. The two stations lie in the same direction from El Chichón, and thus do not give any information regarding an amplitude variation with azimuth.

The origin time of the event that generated the Rayleigh and air wave signals can be inferred from their arrival time by assuming a propagation velocity. For air waves, we assume a velocity of .310 km s^{-1} from dispersion curves of Press and Harkrider (1962). The arrival picks are shown in Figure 8. The origin times inferred from the air wave arrivals, to the nearest 0.5 minute, are 11:20 (ALQ) and 11:22 (LON) (see Table 6). From the IDA records, the inferred origin time of the Rayleigh wave signal is somewhat later (11h 28m) if the beginning of the first large trough is taken as the arrival (Figure 8). However, if the arrival of a small but correlatable peak somewhat earlier in the record is used, shown by the arrow in Figure 8, the inferred

Table 6

Origin Times of Far-Field Seismic Signals
Associated with the Three Main Eruptions of El Chichón

Station	Phase	Arrival Time,[1] GMT	Travel Time,[1] GMT	Origin Time,[1] GMT
Event 94B:				
ALQ	*A*	13:26.0	126.5 min	11:20.0
LON	*A*	15:07.0	225.0	11:22.0
PFO	*R*	11:41.0	13.5	11:27.5
		11:33.0[2]		11:19.5
NNA	*R*	11:45.0	17.0	11:28.0
		11:36.5		11:19.5
HAL	*R*	11:47.0	19.0	11:28.0
		11:38.5		11:19.5
ANM	*P*	11:23.8	288 s[3]	11:19.0
BOC	*P*	11:24.0	301 s	11:19.0
Event 94A:				
ALQ	*A*	03:51.0		01:44.5
LON	*A*	05:30.0		01:45.0
PFO	*R*	02:00.0		01:46.5
ANM	*P*	02:03.6		01:58.6
Event 88:				
LON	*A*	09:13.0		05:28.0

[1] Times are to nearest 0.5 min for *R* and *A* phases.

[2] Second times for IDA stations indicate an alternate arrival pick (see Figure 8).

[3] *P* travel times from Herrin (1968).

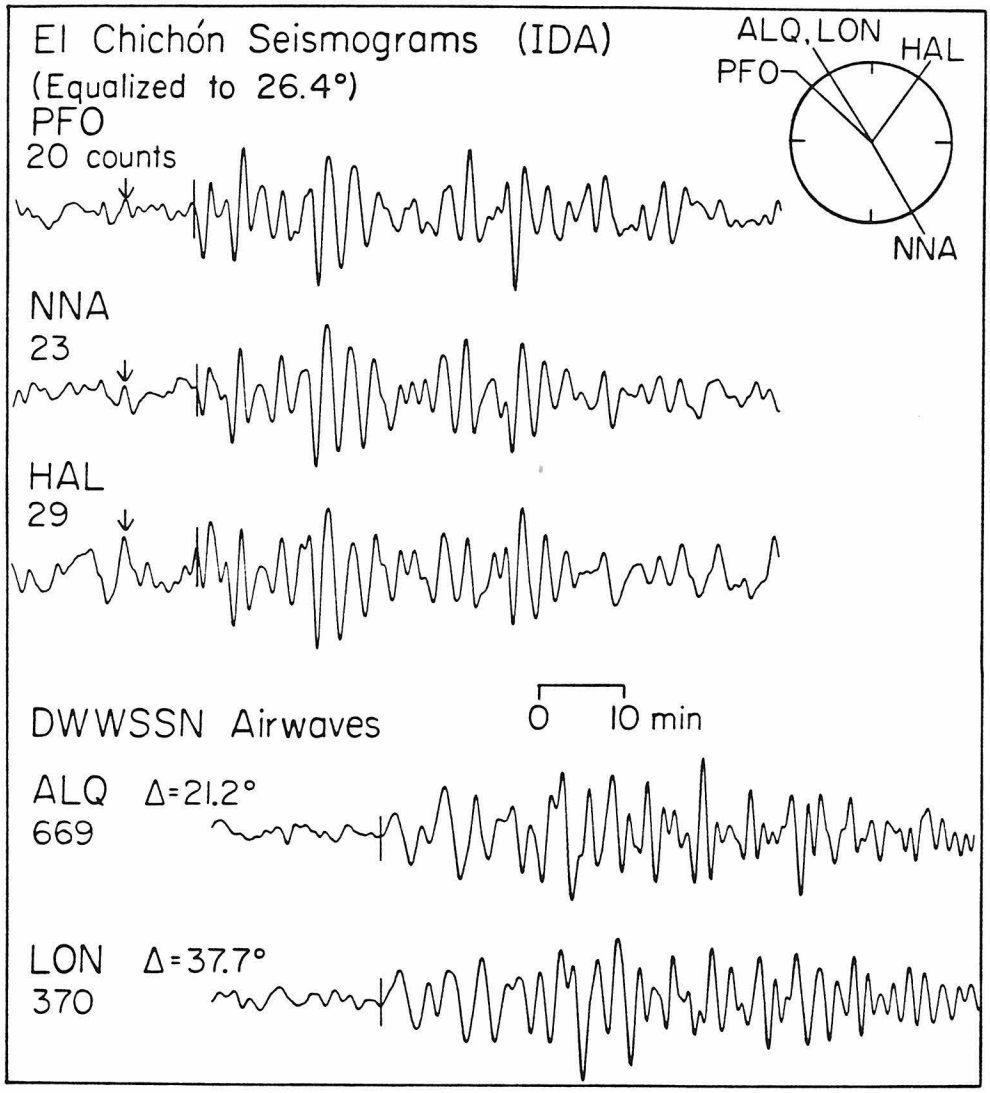

Figure 8. Detail of Rayleigh and air wavetrains from the third eruption. The circle at the upper right indicates the station azimuths. The NNA and HAL records were equalized to the PFO distance and corrected to the PFO response, so that the amplitudes and waveforms are directly comparable for source effects. Maximum peak-to-peak trace amplitudes in digital counts are given above the waveforms. Note the similarity of the Rayleigh and air waveforms. The lines indicate arrivals picked to determine the origin time of the event.

origin time concurs with that from the air wave at 11h 20m. A group velocity of 3.6 km s^{-1} was assumed for the Rayleigh waves, corresponding to waves of period $T \sim$ 200 s. Ground observers at Ostuacán reported the start of rumblings from event 94B at 11h 32m, but the local seismic network began recording signal associated with the event at 11h 10m (Haskov et al., 1983), and the *SEAN Bulletin* reported an observation of the onset of eruption at 11h 22m (Table 3; *SEAN Bulletin*). The accuracy of field reports of the onset of explosive activity is uncertain for event 94B, because the volcano was masked by heavy ash fall that had been continuous since the onset of eruption 94A ten hours earlier.

The velocities and inferred origin times of the arrivals in the record section confirm that these events were caused by events at El Chichón at the time of the eruption. Obviously, the atmospheric wave is a direct consequence of disturbances of the atmosphere during the eruption. A precise specification of the source of the ground motion, however, is not so obvious, and a representation in terms of an equivalent force system cannot be retrieved directly from the seismic records because they are so limited in number and barely above the recording threshold. The Rayleigh wavetrain has the same overall duration and origin time as the air wave signal, and thus appears to have at least a related source. Also, the duration of both types of signals are consistent with field reports of the duration of explosive activity (Table 3). Experience shows that transient air waves of this type are not associated with the steady-state gas-streaming Plinian stage of eruptions; for example, although the Plinian eruption column of Mt. St. Helens endured for 9 hours (Christiansen and Peterson, 1981), air waves were only generated by the initial explosion. Thus it is not actually the overall eruptive source but irregularities in the eruptive source that generate transient waves. If these irregularities are explosions or abrupt releases of

pressure, the source model described in Section 2 is directly applicable. If they are caused by phenomena unrelated to pressure release, the explosive model may not be accurate.

Long-period observations of events 88 and 94A. The first and second eruptive phases of El Chichón, events 88 and 94A, were also recorded by IDA and GDSN stations (Table 5). Overall, in terms of the long-period far-filed seismic and air wave amplitudes, event 94B was largest eruption, 94A the second largest, and 88 the smallest. Figure 9 shows the Rayleigh wavetrains for the three eruptions recorded at the IDA station PFO (26.4^o from El Chichón) together with the Rayleigh wave from the main eruption of Mt. St. Helens recorded on an IDA station at a similar distance (Δ=23.4^o). The records are shown on the same vertical scale. The records from the first two El Chichón eruptions have roughly the same duration (25-30 min) and amplitude, which are both smaller than the duration and amplitude of event 94B. The events are similar to 94B in that the signal endures for tens of minutes, and features within the overall signals are very coherent at the other IDA stations HAL and NNA (not shown), located at different azimuths from the source. As discussed in Section 2, the large, compact Rayleigh wave pulse in the Mt. St. Helens record was caused by the near-horizontal force associated with the landslide; the duration of the force was approximately 3 minutes. Following this signal in the Mt. St. Helens record are over 30 minutes of a signal that appears similar to, but somewhat smaller than, the El Chichón IDA signals.

Air wave signals on the DWWSSN instruments from the three eruptions are shown in Figure 10. There is a clear arrival at both stations from event 94A, at station LON for event 88 (arrow in Figure 10). There is no obvious air wave arrival for

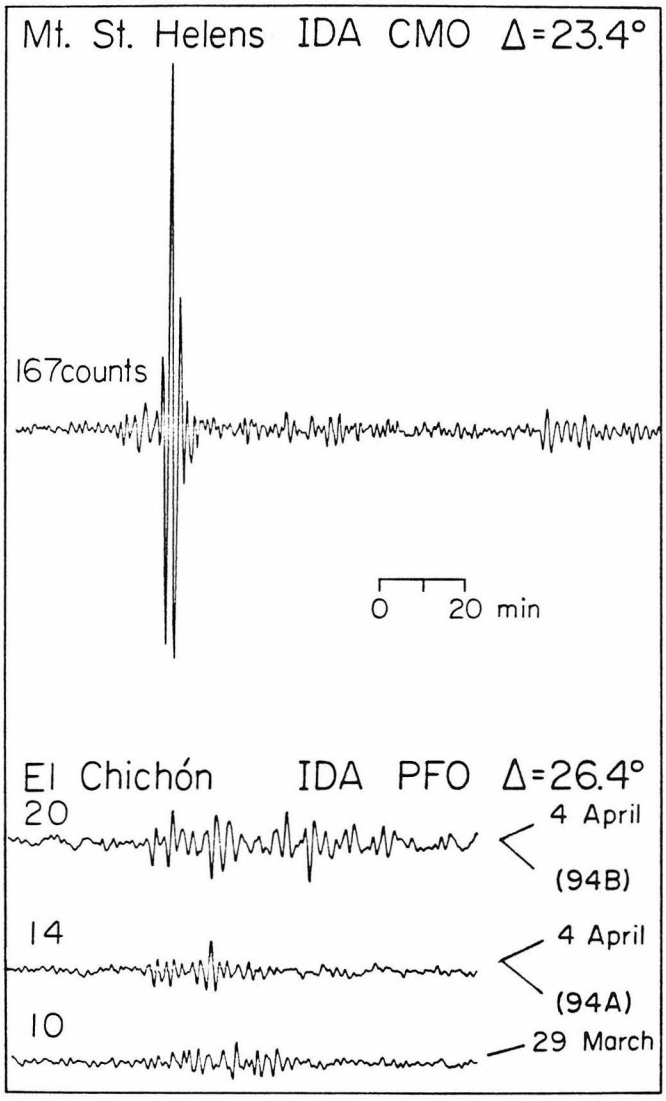

Figure 9. PFO records from the three eruptions of El Chichón shown with a record of the major eruption of Mt. St. Helens from an IDA station at a comparable distance, with the vertical scale preserved. The Rayleigh wave from the Mt. St. Helens eruption was caused by the large landslide accompanying the event. Maximum peak-to-peak trace amplitudes in digital counts are shown above the traces.

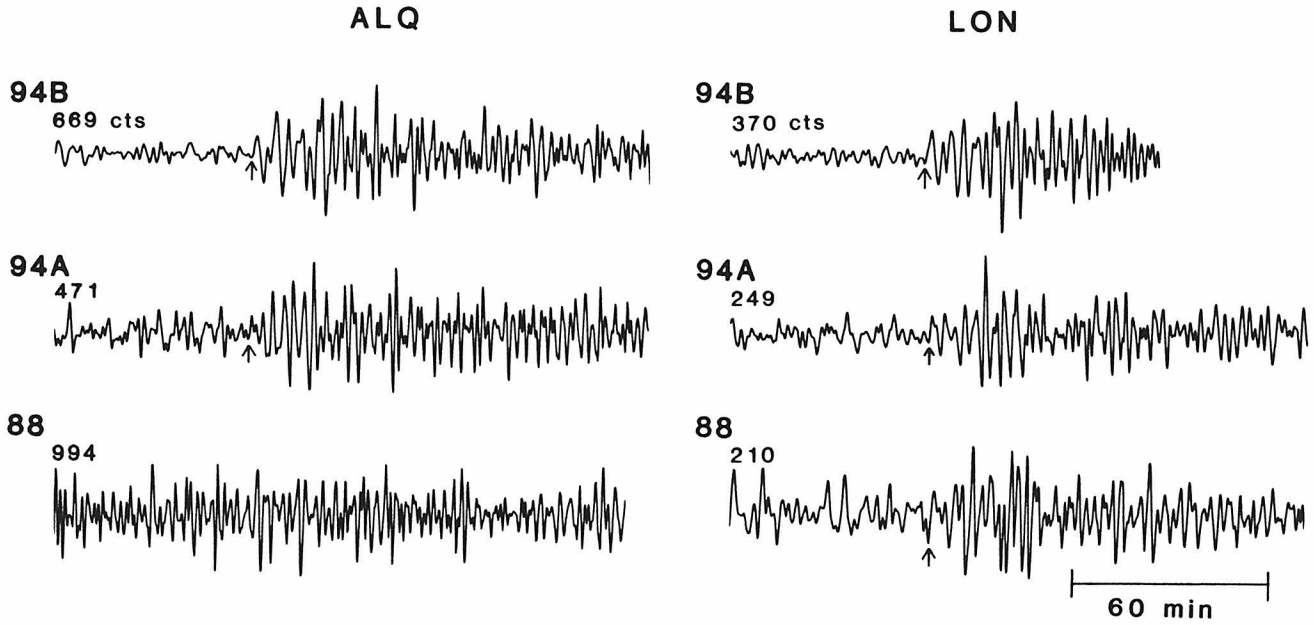

Figure 10. Air waves recorded on the two DWWSSN instruments from the three eruptions of El Chichón. Arrows indicate arrival picks. No arrival was seen at ALQ from event 88, although the background count was larger than that of the other air waves.

event 88 at ALQ, although the background count is higher during the expected arrival window than during the actual airwave arrivals associated with the other two eruptions, probably due to a more local seismic disturbance. The origin times of the air wave signals generally correspond to the observed eruption times (Tables 3 and 6). The inferred origin time of the air wave signal from event 94A (01:45) is somewhat later than the abrupt explosion onset reported by ground observers (01:32 with an estimate of two minutes maximum inaccuracy (De la Cruz-Reyna, pers. comm.). However, this event was reported to have had continuous explosive activity for at least 30 minutes. The origin time inferred from the Rayleigh wave signal at IDA station PFO (11:46.5) is in better agreement with the air wave origin time than with the ground observation, although it is difficult to pick the precise arrival due to low signal amplitude. If the ground reports are accurate, these results imply that the largest explosions of the second eruption occurred about 10 minutes into the event. The air wave from the first eruption, event 88, had an inferred origin time of 05:28, roughly coincident with the ground observation of eruption at 05:32. This ground report may have less timing accuracy than the other eruptions because event 88 was the first (and thus less expected) eruption, and scientific personnel were not yet in the area. Haskov et al. (1983) reported that the near-field short-period seismic signal associated with event 88 began at 05:15.

The peak signal amplitudes of long-period Rayleigh and air waves achieved during the three eruptions are compared in Table 7. Event 94B had the largest surface and air wave amplitudes at all stations except HAL. With this exception, the ratio of signal amplitudes between events is fairly consistent from station to station. Amplitudes from event 94A are .67-.70 times the 94B amplitudes, and event 88 amplitudes are .50-.57 times event 94B amplitudes. This ranking (94B, 94A, 88) is in agreement

Table 7

Amplitudes of Far-Field Seismic Signals
Compared for the Three Main Eruptions of El Chichón

Station	Phase	Event 94B	Event 94A	Event 88	$\frac{94A}{94B}$	$\frac{88}{94B}$
ALQ	*A*	669[1]	471	-	0.70	-
LON	*A*	370	249	210	0.67	0.57
PFO	*R*	20	14	10	0.70	0.50
NNA	*R*	24	16	glitched	0.67	-
HAL	*R*	15	18	13	1.20	0.87
ANM	*P*	764	1205	-	(1.58)	-
BOC	*P*	842	-	-	-	-

[1] All amplitudes are peak-to-peak in digital counts.

with the relative size of the three eruptions as qualitatively described by ground observers (De la Cruz-Reyna, 1982) and as described by the associated near-field seismic signal (Table 3; Haskov et al., 1983).

Teleseismic body waves from events 94B and 94A. Records from SRO and DWWSSN stations (sampling rate of one point per second) were searched for body phases during the eruption windows in an attempt to find signals that could be clearly associated with a vertical single force source, as was observed from the major eruption of Mt. St. Helens. The DWWSSN instruments were too noisy to record body phases, but signals were observed for the two larger eruptions 94B and 94A at the two SRO stations closest to El Chichón, ANM and BOC. These stations are approximately opposite in azimuth and at nearly the same distance from El Chichón within the P wave upper-mantle triplication range where the amplitudes are amplified. Unlike Mt. St. Helens where P waves were seen on SRO stations up to 80^{o} from the source, body phases from the El Chichón eruptions could not be seen at stations beyond triplication distance. From the observations of the sustained, longer-period surface and air wave signals discussed above, one would expect to see a clear sequence of individual sources lasting for several minutes in the body waves, but this was not observed. Instead, the predominant body-wave signal from both the 94B and 94A eruption appears to be caused by a single pulse source. The observed P arrival from event 94B corresponds to the same inferred origin time as the longer-period air and Rayleigh waves from the event (Table 6). For event 94A, the predominant P arrival has a much later ($\sim$ 10 min) origin time that the longer-period signals. Further, the 94A ANM and BOC seismograms are longer period than the corresponding records for event 94B. On closer inspection, lower-amplitude signals that may be from El

Chichón can be found preceding the obvious P arrival of event 94A; these would bring the inferred origin time into better agreement with the estimates obtained from the surface and air waves. These observations are illustrated with several Figures as discussed below.

Figure 11 shows vertical, radial, and transverse seismograms of event 94B from the SRO stations ANM and BOC. The vertical display scale is different for the two stations because the shorter-period surface waves at BOC are greatly enhanced relative to ANM, probably due to the unusual travel path to BOC, which lies directly along the axis of the Mid-America subduction zone. The predominant sharp arrival at ANM on the vertical and radial traces is taken to be P, and the corresponding S time (from Jeffreys-Bullen tables) is shown. Note that there is SV motion on the vertical and radial components but no substantial SH arrival on the transverse component, which is consistent with the radiation pattern for a vertical force. The latter part of the records show the beginning of the surface wave. The P wave is much clearer at ANM, where it is compressional on both components. The P wave is compressional on the BOC vertical component but not clear on the radial. The P wave amplitudes are comparable at the two stations, which is again consistent with the azimuthally symmetric radiation pattern of the vertical single force. Station BOC also shows little SH radiation. The origin time corresponding to the P arrivals is 11:19.0, the same as the estimates from the surface and air waves. Figure 12 shows a detail of the beginning of the BOC record.

Figure 13 shows the same records for the second eruption, 94A. The records are similar overall to event 94B but all phases are notably longer period, and there may be some SH energy at ANM. Further, the P arrival at BOC is not clear. The origin time inferred from the ANM P arrival is later than that estimated from the IDA

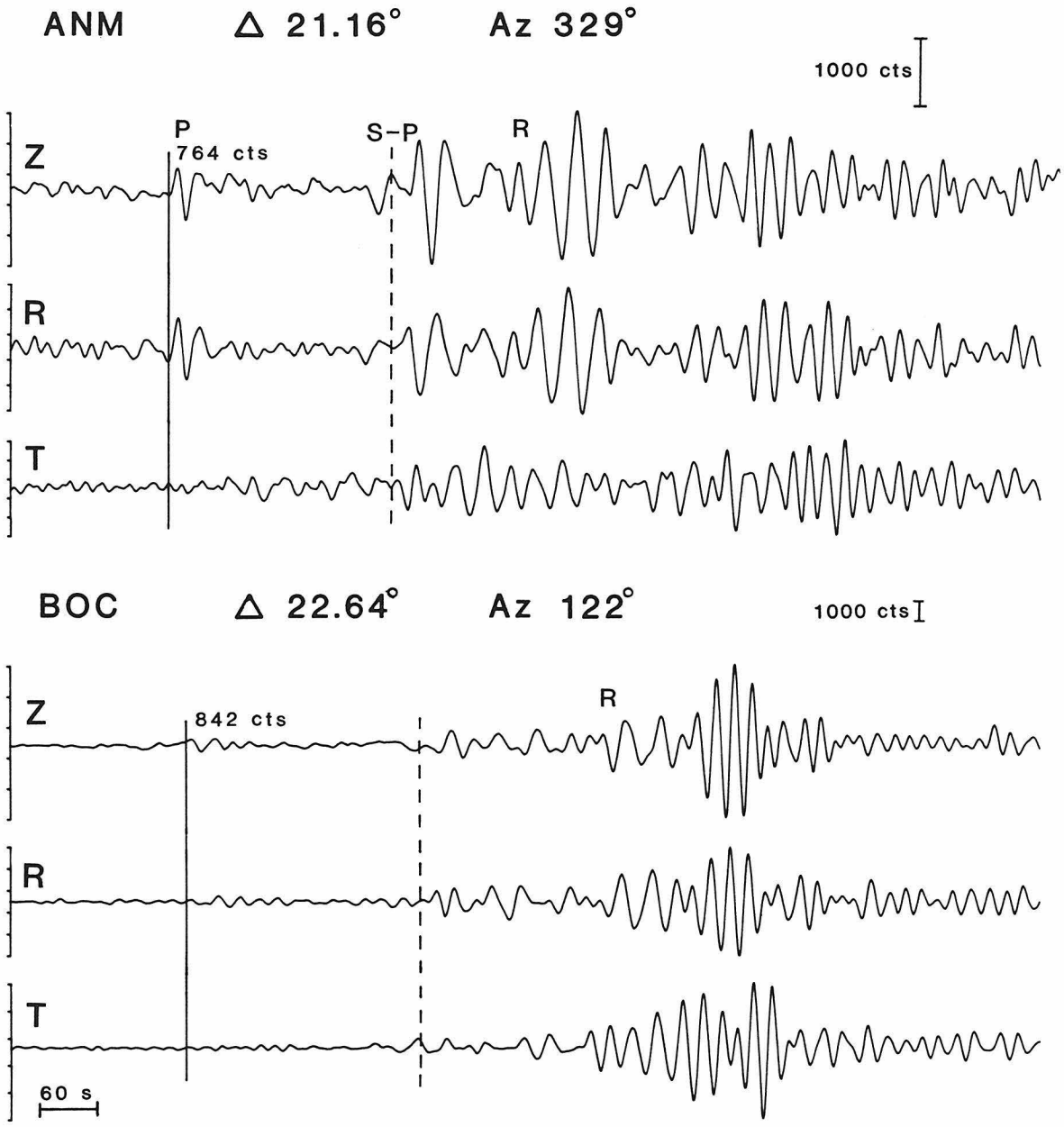

Figure 11. Vertical, radial, and transverse long-period seismograms of event 94B recorded at SRO stations ANM and BOC in opposite azimuths. Record start time is 11:21. *P*, *SV*, and Rayleigh wave arrivals are observed. Higher-frequency Rayleigh waves are enhanced at BOC by the travel path. The origin time of the signals agrees with the origin time of the IDA Rayleigh and DWWSSN air waves, and is close to the eruption onset time reported by ground observers.

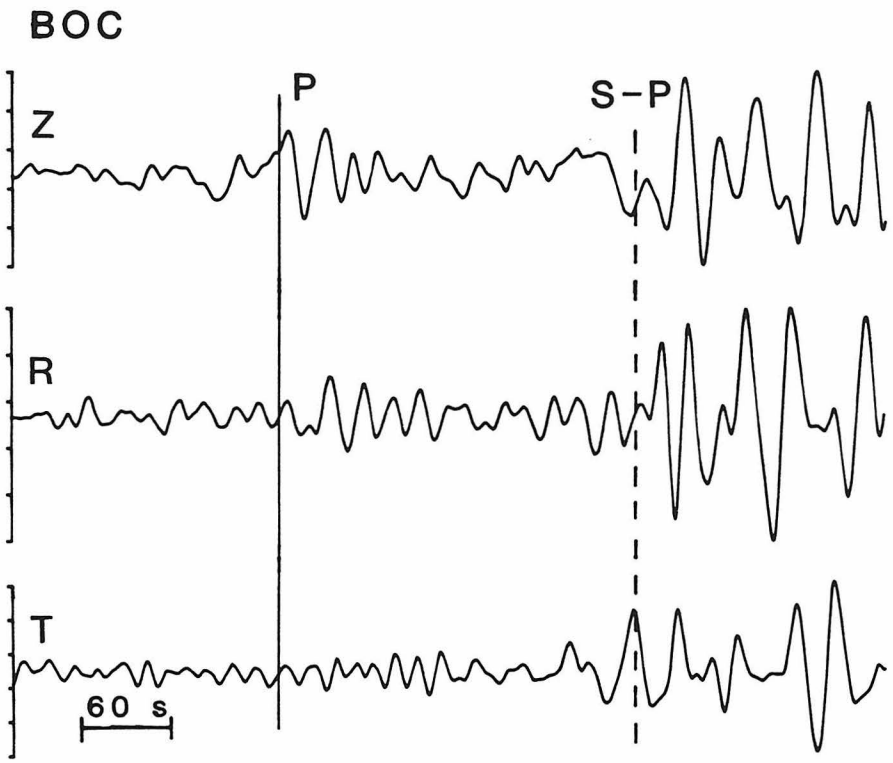

Figure 12. Detail of the beginning of the BOC record of event 94B. The vertical axis has been expanded so that the P phase can be observed.

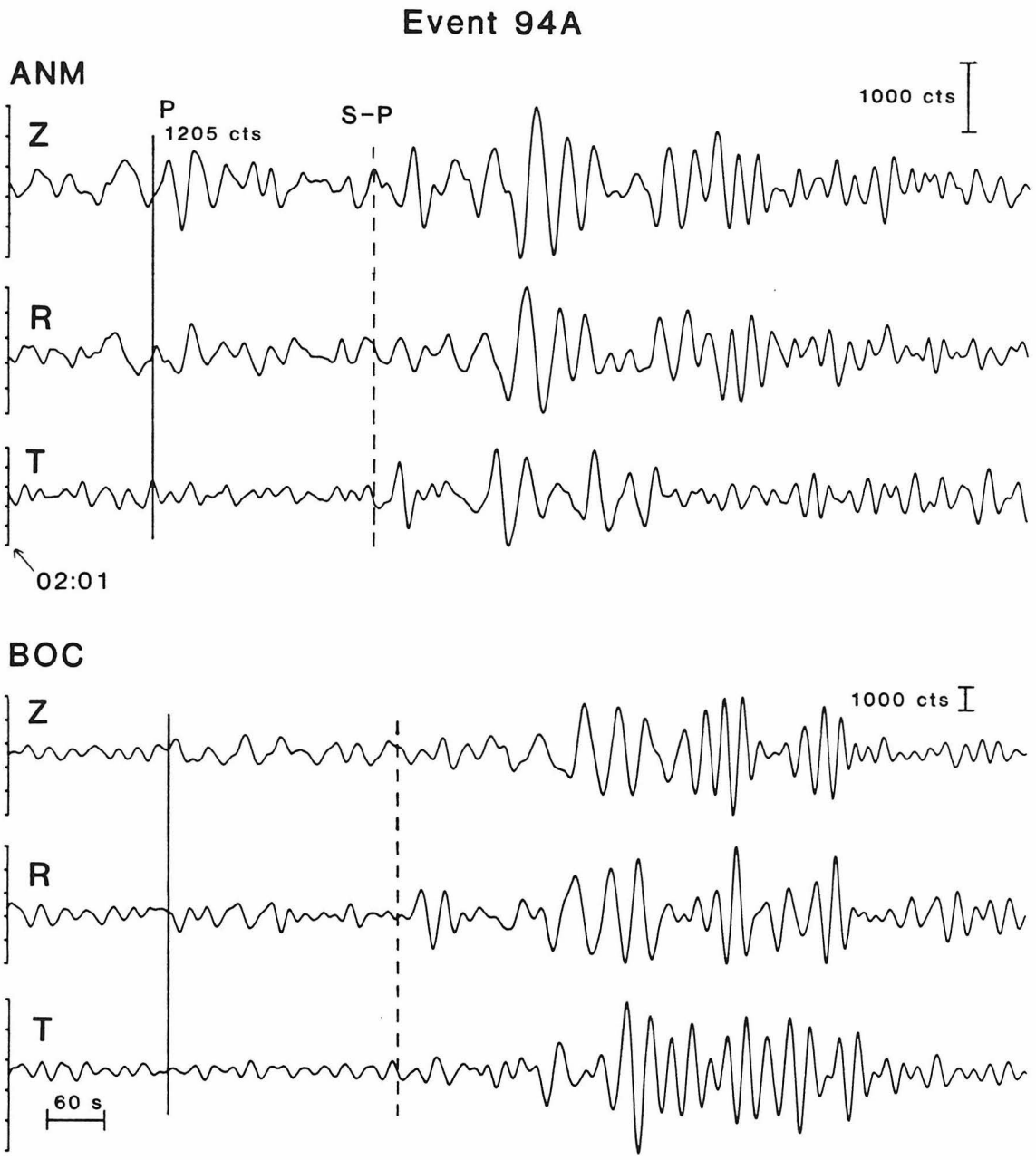

Figure 13. ANM and BOC records from event 94A. Note that the records are similar to but longer period than those of event 94B shown in Figure 11, and that the *P* arrival is not clear except on the vertical ANM record. The origin time of the *P* wave is nearly 14 min later than the inferred origin time of the 94A IDA Rayleigh and DWWSSN air wave signals.

records and air waves by about 12 minutes (Table 6), which was already late compared to ground reports. There are some low-amplitude signals at ANM before the *P* arrival, but they are much smaller and of questionable association. Recall that the 94A event was observed to involve a sustained series of explosions lasting approximately 30 minutes, so that the body wave signal could be due to a single larger explosion that occurred well into the sequence. However, event 94B was also reported to have sustained explosive activity, yet, in contrast to 94A, its body wave arrivals correspond to the same origin time as the longer-period signals, as well as the field reports of eruption onset. Further, the 94B records show characteristics of the radiation pattern of a vertical single force source, but this is not as clear for 94A. Although we know the 94A signal originated at El Chichón during the second eruption, it is difficult to interpret the records against the large background signal, which is probably present because the eruption had already begun.

Impulse of event 94B inferred from forward modeling. Assuming that the 94B *P* wave was caused by a vertical single force source, the force amplitude and duration can be estimated by modeling the observed records. For the ANM *P* wave, we use a WKBJ approximation to describe the propagation through the upper mantle, and a velocity model appropriate for a tectonic region (Chapman, 1978; Walck, 1984). The record is best fit with a force magnitude of 7.3 x 10^{16} dyne and a triangular time function with a 6-s base, for a seismic impulse of 2.2 x 10^{17} dyne s. To check this estimate, we also model the short-period ($\sim$20 s) vertical Rayleigh wave in the opposite azimuth at station BOC by using the propagator matrix method described by Harkrider (1964*a*) to calculate surface wave dispersion, and find a peak force of 5.8 x 10^{16} dyne with a 6-s base triangular time function, or, a seismic impulse of 1.7 x 10^{17} dyne

s, in good agreement with the ANM value. The synthetic seismograms are shown in Figure 14. The inferred impulse is over ten times that of the largest secondary eruption of Mt. St. Helens (1.4 x 10^{19} dyne s), but much smaller than the impulse of the major Mt. St. Helens eruption at 1.4 x 10^{19} dyne s (Table 2; Kanamori and Given, 1983).

Conclusions

Seismic signals associated with the El Chichón eruptions were observed in two period bands; long-period, low-amplitude Rayleigh waves (T $\sim$ 180-200 s) from all three eruptions, and shorter-period body and Rayleigh waves from the two largest eruptions. In addition, air waves recorded on DWWSSN instruments were seen from all three eruptions. The source of the long-period surface waves and air waves appears to be coupled in that both types of signals have unusually long durations, indicative of a protracted source; they also have concurrent origin times. The precise physical source of the signals is unknown, but one suggestion is that they are caused by atmospheric disturbances or turbulences during the eruptions that directly load the ground to produce the low-amplitude Rayleigh wave motion. Such disturbances could be explosions, but that raises the question of why a series of explosions is not more apparent as vertical single-force sources in the body wave records. One conclusion is that the source is inherently long period and thus not efficient at generating impulsive body phases large enough to be seen teleseismically. The amplitudes of the long-period signals agree with the relative ranking by ground observers, air fall volume, and near-field short-period seismic signals of the sizes of the three eruptions; the third eruption (94B) created the largest signal, the second eruption (94A) the second

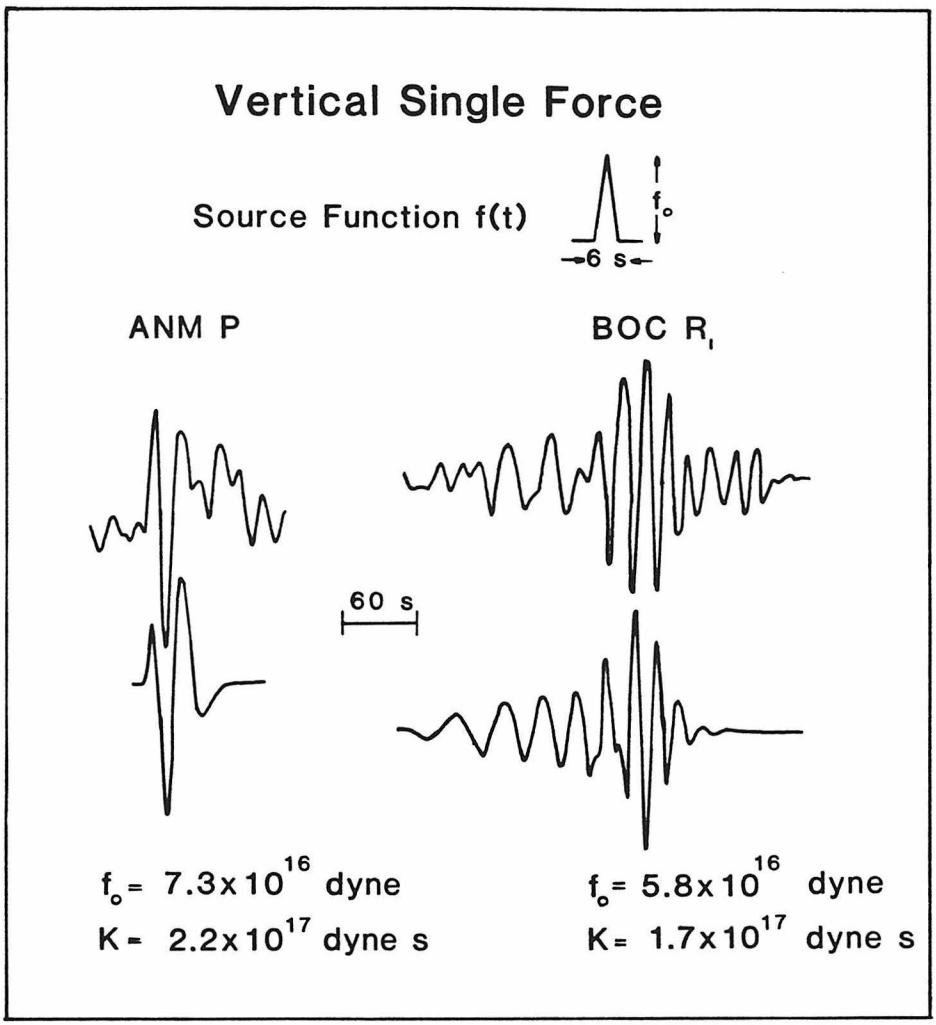

Figure 14. Observed ANM *P* wave and BOC Rayleigh wave (upper traces) from event 94B shown with synthetic seismograms (lower traces) made assuming a vertical single force source and a triangular time function. Both records are best fit with a triangle base of 6 s. Resulting force magnitudes and impulses are shown.

largest, and the first eruption (88) the smallest. The signal duration from event 94B was also longer than that of the others; ground observers report that eruption 94B endured about 70 min, while event 94A lasted approximately 30 min.

Shorter-period body phases and Rayleigh waves from the two larger eruptions were observed at two SRO stations within upper-mantle triplication distances at opposite azimuths. The records from the last and largest eruption (94B) show characteristics of a vertical force radiation pattern and have an origin time near that of the longer-period signals and estimates of eruption time from ground observers; thus we tentatively interpret the signal as being due to the initial explosion of the sequence. If this source assumption is correct, the eruption can be quantified by a force magnitude and duration. We find that the seismic impulse is $\sim$ 2 x 10^{17} dyne s, which is over ten times larger than the largest secondary eruption of Mt. St. Helens, but two orders of magnitude less than the main eruption. The short-period signal from event 94A does not show some of the single force characteristics that were seen for event 94B. The P wave is seen at ANM but unclear at BOC. Further, the signal is much longer period than that of event 94B. The signal origin time (01:58) is well into the explosive sequence, which was documented as beginning abruptly at 01:32 with a two minute accuracy (De la Cruz-Reyna, pers. comm.). Thus we hesitate to interpret the signal as having a single-force source. Alternatives are that the signal may be earthquake-related, or it may be the short-period expression of the longer-period source that generated the IDA signals. Since the event was known to begin abruptly with violent explosions, the lack of single-force signals earlier in the record is puzzling. It could be that event 94A simply had smaller explosions than 94B. The late-arriving, longer-period P wave at ANM from event 94A has a larger amplitude than 94B, so that if it is due to the explosion source, it would have a larger seismic impulse.

5. Lamb Pulses from Mt. Asama, Japan

Asama Volcano in Honshu, Japan (36.40° N, 138.52° E) is one of Japan's most active and well-observed volcanoes. Mt. Asama has experienced several episodes of explosive activity in the last 15 years (Simkin et al., 1981). The Matsushiro Seismic Observatory of the Japan Meteorological Agency (JMA) is located 31 km northwest of Mt. Asama, and is the site of WWSSN station MAT and ASRO station MAJO (operational since 1977). In addition, JMA runs several shorter-period seismographs in the vicinity of the volcano.

In this Section, we discuss seismological observations of explosive activity at Mt. Asama experienced in February-March, 1973, April 25, 1982, and April 8, 1983 (Shimozuru et al., 1975; Shimozuru et al., 1982; *SEAN Bulletin*, 1983). The 1973 episode comprised several large explosions occurring over a matter of months, whereas the 1982 and 1983 events were more isolated events. JMA observers have recognized "explosion earthquakes" at Asama for some time; that is, seismic signals from the explosions themselves that are presumably explainable with the source model described in Section 2. Here, we discuss seismic signals from the explosions recorded on the long-period, three-component instruments MAT and MAJO. Instrument amplitude responses for the WWSSN, ASRO, and other long-period instruments are shown in Figure 15.

Seismograms of three explosions of Mt. Asama from the WWSSN station at Matsushiro are compared in Figure 16. Longer-period records available from ASRO station MAJO from the 1982 eruption are also shown. The three MAT records are shown with the same vertical scale. Times of the 1973 explosions are known very accurately and are given in Table 8. Two predominant observations can be made

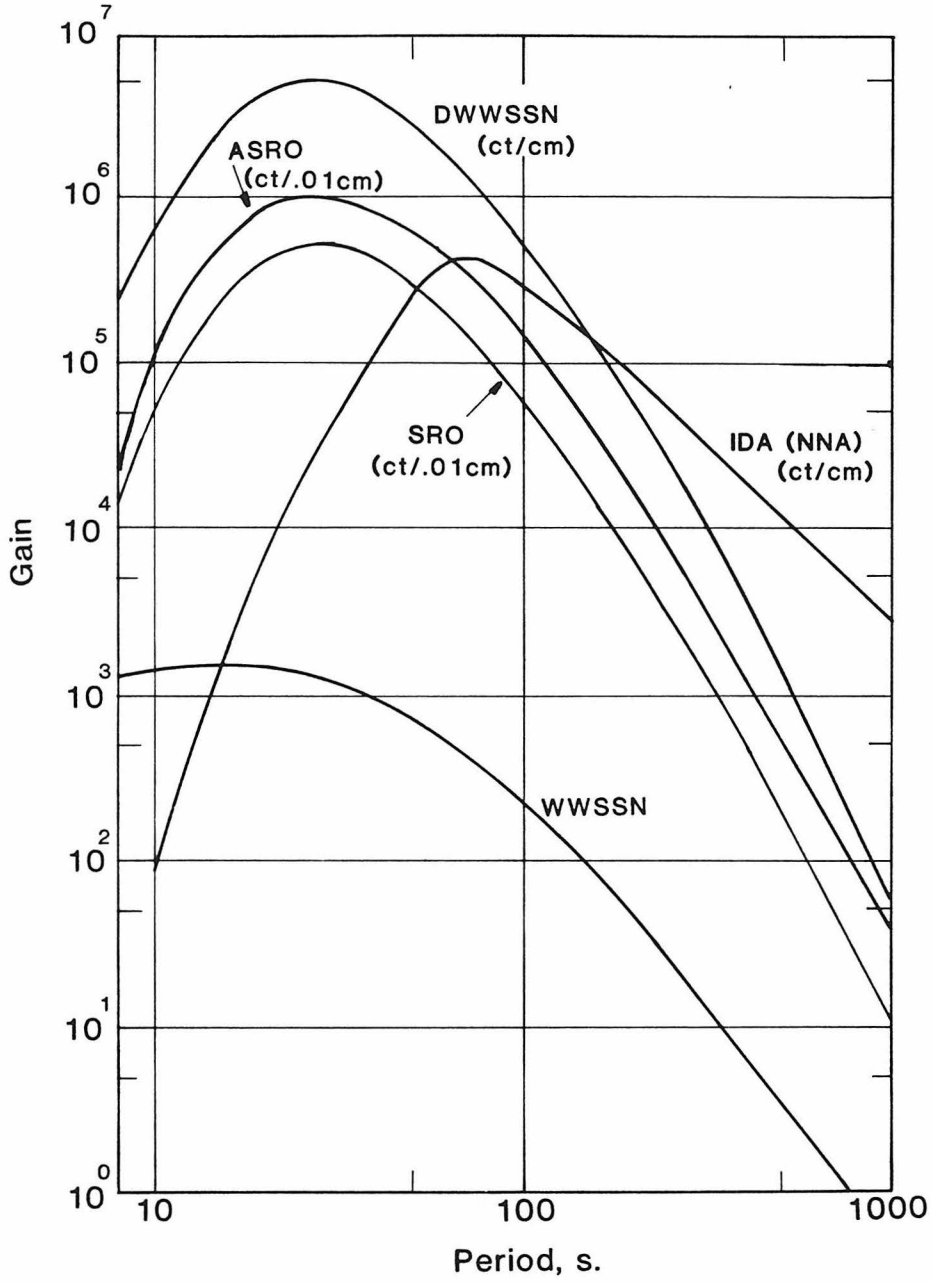

Figure 15. Instrument gains versus period of several of the instruments used in this study: WWSSN, IDA, and GDSN instruments SRO, ASRO, and DWWSSN.

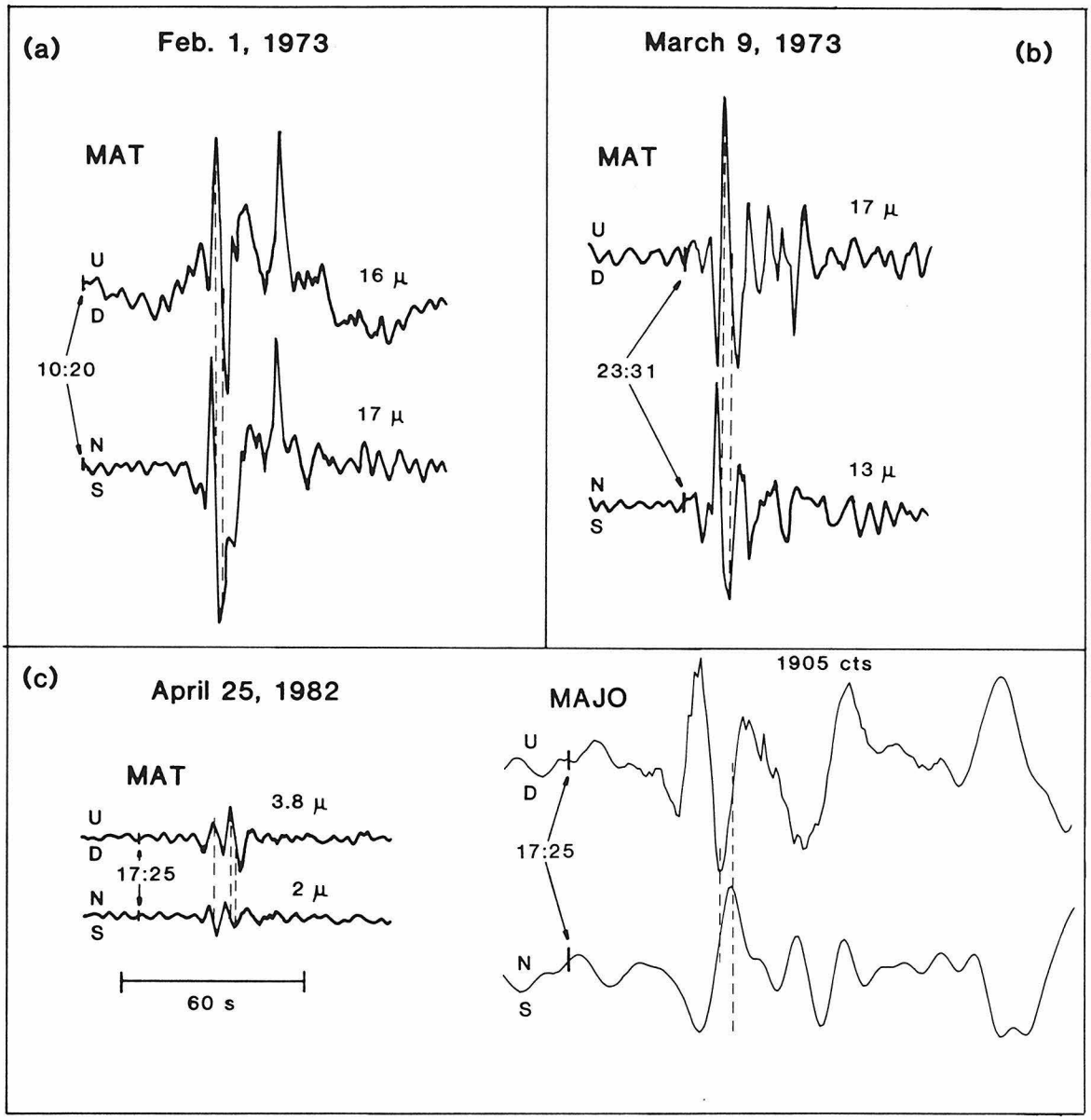

Figure 16. Vertical and north-south components of observed records of three explosions of Mt. Asama. (*a*) February 1, 1973. (*b*) March 9, 1973. (*c*) April 25, 1982, showing both the WWSSN record and the longer-period ASRO record at MAJO. Vertical scales are the same except for the MAJO record. Approximate peak-to-peak ground amplitudes are given over the traces for the WWSSN records. Lines indicate that the vertical and north-south components of ground motion are 90° out of phase.

Table 8

Inferred Seismic Impulses for Eruptions of Mt. Asama

Eruption	Explosion Time	Seismic Impulse, [1] dyne s
February 1, 1973	10:20 26.0s	2.3×10^{16}
March 9, 1973	23:30 56.0s	1.8×10^{16}
April 25, 1982	17:25	4.2×10^{15}
April 8, 1983		1.8×10^{16}

[1] From Kanamori and Given (1983) except for April 1983, from Takeo et al. (1984).

from Figure 16; first, the waveforms are not identical for the three explosions, secondly, the signal has an emergent beginning and the vertical and north-south components of ground motion are 90^o out of phases as expected for Rayleigh motion, which indicates that the records are from a nearby near-surface source that excites a sharp Rayleigh pulse such as the vertical single force. This plus the control on explosion times confirms that the records are the seismic manifestation of the explosions; except for these signals, the records are very quiet within several minutes of the explosion times. Note that the February 1 and March 9 records in particular are complex in that they show arrivals $\sim$ 25 s behind the first signal arrival. The MAT records from the April 8, 1983 eruption are not shown, but they are almost identical to the March 1973 event.

By the time of the April 1982 eruption, the ASRO station MAJO at Matsushiro was operating. Figure 17 shows a comparison of the vertical records from the largest secondary eruption of Mt. St. Helens on the DWWSSN station at Longmire with the April 1982 Mt. Asama records from MAJO. The initial part of the Asama record is similar to the Mt. St. Helens record, but has a longer-period pulse after the initial arrival that is not seen for the Mt. St. Helens event. The Mt. Asama air wave arrives about 90 s after the seismic pulse.

The dissimilarities in the MAT waveforms of the three Asama explosions introduce a new consideration into the single force model — the cause of source differences. Aside from the major Mt. St. Helens eruption, which had a complex time history, the Mt. St. Helens Lamb pulse records were very similar between eruptions (Figure 4); however it should be noted that the Asama explosions were recorded on a shorter-period instrument than (and at about half the distance as) the Mt. St. Helens eruptions. The variation in the Mt. Asama explosion records has been initially

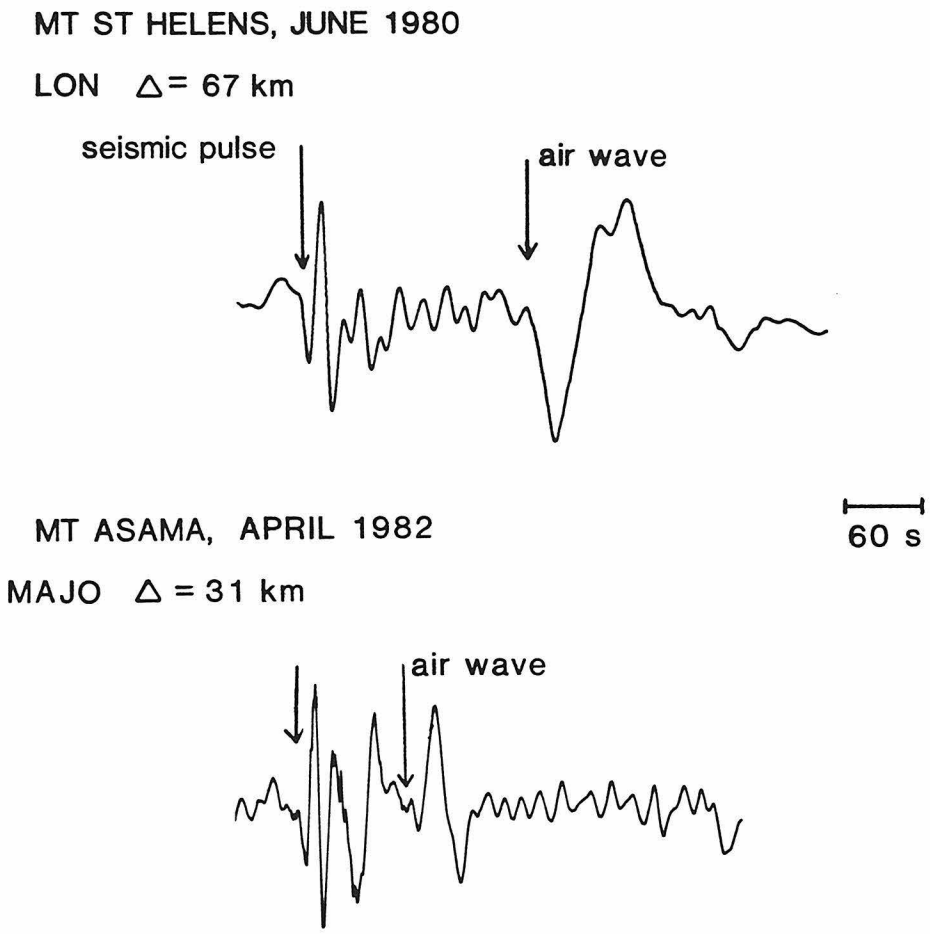

Figure 17. Comparison of Lamb pulse records from the largest secondary eruption of Mt. St. Helens and the April 1982 eruption of Mt. Asama, recorded on DWWSSN and ASRO instruments respectively.

examined by Kanamori and Given (1983). In what follows, I summarize their results because of their importance to the theme of this Chapter.

Time functions of the three Asama explosions assuming the vertical single-force source were obtained by Kanamori and Given (1983) by direct deconvolution of the vertical force Green's function from the observed vertical-component WWSSN records. Resulting force time functions are shown in Figure 18. All the Asama time functions are shorter period and more complex than the Mt. St. Helens time function. The March 1973 and April 1982 time functions clearly begin as a downward force (up on Figure 18) but the February 1973 time function has a very small initial downward force, followed by a large upward force. In fact all the Asama records appear to have a large upward component. This should not be caused by the relaxation of the ground due to pressure release, because that response was incorporated into the isotropic component (implosion source) as discussed in the description of the model in Section 2. There could be several other possible explanations for this result. First, perhaps the source is more complicated at the shorter periods observed in the WWSSN band. However, for the two eruptions observed on both the standard WWSSN and longer-period instruments — Mt. St. Helens June 13 and Mt. Asama 1982 — the source time function deconvolved from the WWSSN record can fit both the amplitude and waveform of the signal on the longer-period instrument. Second, the particulars of the volcano, such as the vent shape or a directedness to the explosion, may influence the source. Further, it may be that the Asama time functions are shorter period than the Mt. St. Helens event because the force duration is related to the dimensions of the vent area or pressure reservoir (see Figure 1). The Mt. St. Helens system had just been purged by a climactic eruption the previous month, and had a recently defined vent and chamber of large dimensions. Asama, on the other hand, has only erupted in

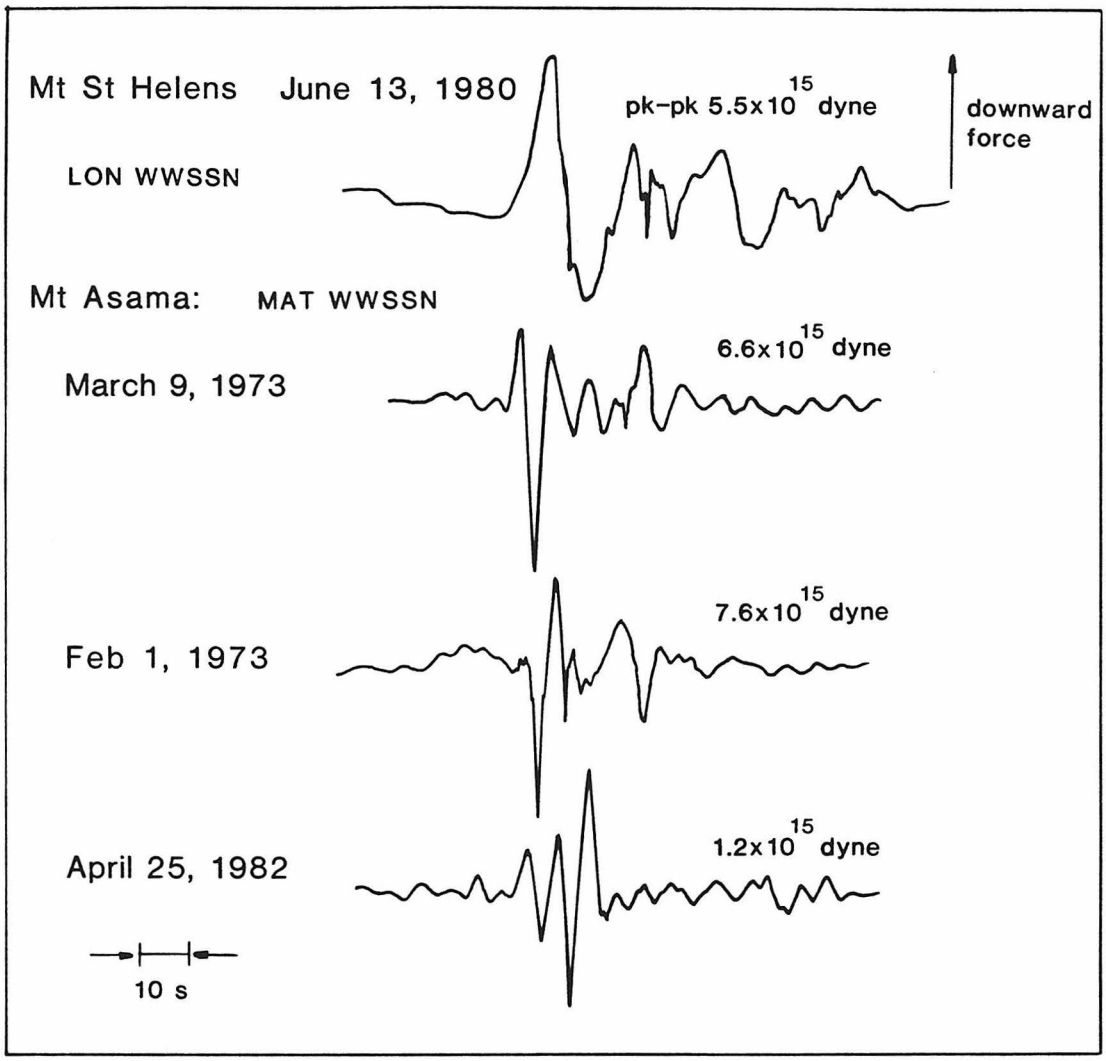

Figure 18. Force time functions for Mt. St. Helens and Mt. Asama eruptions deconvolved from WWSSN vertical records assuming the vertical single-force source. Downward force is up in the Figure. Peak-to-peak amplitudes of the time functions in dynes are shown.

smaller explosions (VEI$\leq$3) since 1783 (Simkin et al., 1981).

Takeo et al. (1984) studied the source of the April 1983 explosion earthquake, which had nearly identical waveforms to the March 1973 event, using the source model of Kanamori et al. (1984). They noted that explosion signals from Mt. Asama frequently have a component not explainable by a purely vertical force, which may be a horizontal force component or a small dislocation source. They concluded from waveform analysis that the April 1983 signal was due to a combination of two downward forces 10 s apart and a strike-slip dislocation component occurring 17 s later, with a moment of 3.2 x 10^{21} dyne cm, which is equivalent to an earthquake magnitude of 3.6. They interpreted this component as tectonic release on faults immediately surrounding Mt. Asama. Takeo also noted that the removal of mass in lid AB (Figure 1) from the system may contribute an upward force to the seismic source, which was not considered in the model proposed by Kanamori et al. (1984).

Kanamori and Given (1983) assigned peak forces f_o and seismic impulses K to the Mt. Asama explosions. These are given in Table 8 and shown with the results from Mt. St. Helens and El Chichón in Figure 19. In addition, Takeo et al. (1984) found an impulse of 1.8 x 10^{16} dyne s for the 1983 explosion, which is similar to the values of the March 1973 and February 1973 explosions.

Conclusions

Observable differences in near-field seismic signals from three different explosions of Mt. Asama show that the explosion source can be more complicated than the simple model that was successful in explaining the near-field observations of Mt. St. Helens. However, the Mt. St. Helens Lamb pulses were examined by forward modeling

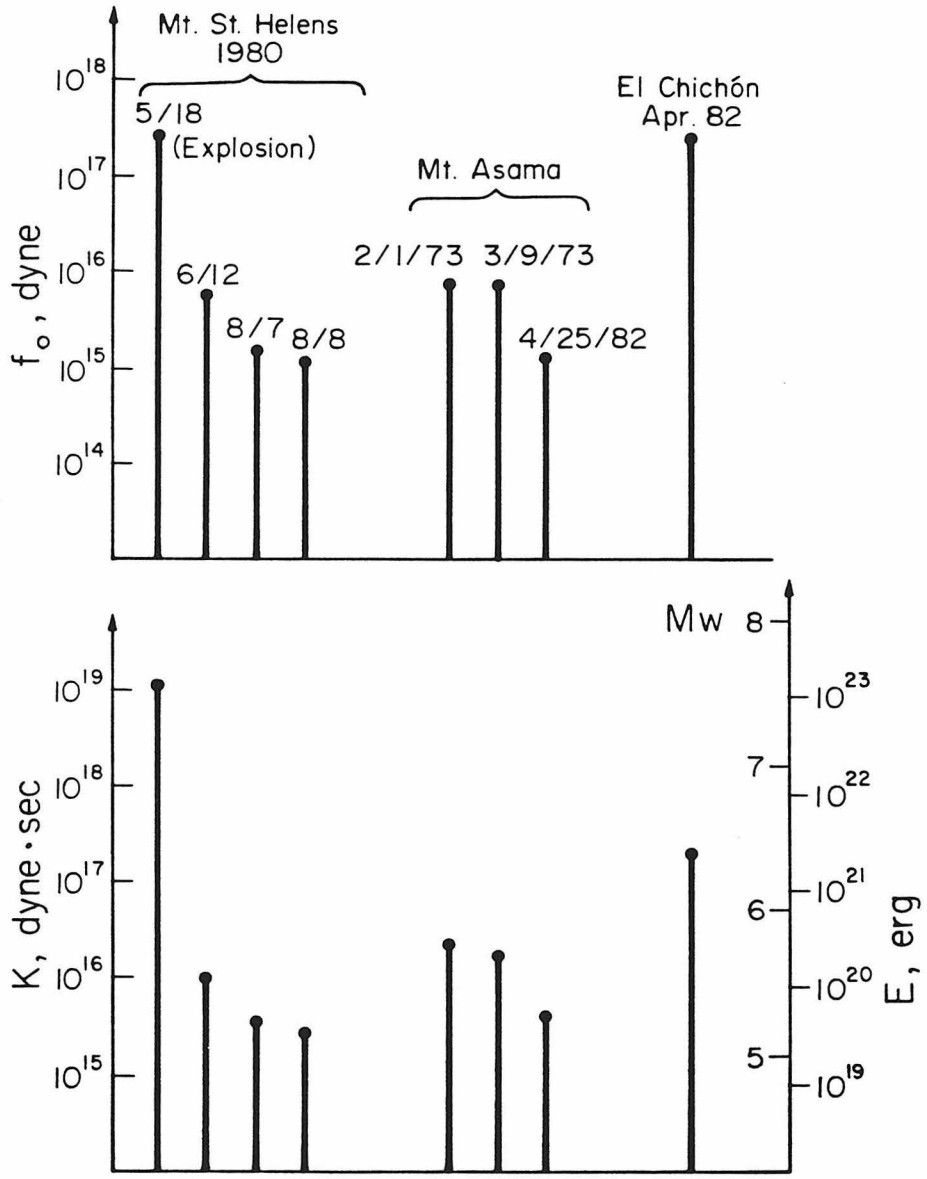

Figure 19. Chart comparing peak force magnitude f_o (upper) and seismic impulse K (lower) inferred from seismic signals for explosive volcanic eruptions discussed in this Chapter. Energy and equivalent earthquake magnitude are shown on the right.

of the DWWSSN records. It is possible that a more rigorous deconvolution of the shorter-period WWSSN records would reveal fine structure to the time functions along the lines of the Mt. Asama observations. Complications may include multiple explosions, differences in source duration, a non-vertical component to the force, or a small dislocation source expressing tectonic stress release that occurs at the time of eruption. It may be that the single force model is best applied to larger eruptions such as the major Mt. St. Helens eruption, where the explosive component would be much larger than other effects such as a concurrent stress release.

6. Atmospheric Waves Observed from Large Explosive Eruptions

Waves traveling in the atmosphere have been observed following the largest, most explosive volcanic eruptions. For example, the volcano Krakatau (Krakatoa) in Indonesia in 1883 generated atmospheric waves that were observed for 5 antipodal passages — the equivalent of observing the R_7 seismic surface wave passage. Atmospheric waves from the May 1980 eruption of Mt. St. Helens were observed in Europe and Asia. In this Section, we present observations of air waves from several large explosive eruptions, and note that the air wave amplitude, dominant period of the waveform, and signal duration can vary significantly with the overall "size" of the eruption. We describe and test a preliminary model of air wave excitation where the volcanic source is proportional to the total volume of atmosphere displaced by the outflowing volcanic products.

Previous Studies of Atmospheric Wave Propagation

Pekeris (1939) first considered the propagation of a pulse from a surface source in atmospheres of very simplified temperature and density variations in an attempt to explain observations of the globally recorded air wave from the eruption of Krakatau. However, aside from Krakatau and a large meteor impact in Siberia in 1908, natural sources large enough to be the source of globally observable atmospheric traveling waves that could be detected by barographs were quite rare. Interest in near-surface sources of atmospheric waves was renewed with the development of thermonuclear weapons. Large (i.e., megaton) nuclear tests detonated in the atmosphere were routinely recorded on sensitive barographs, dubbed "microbarographs," that had been designed in part for detection of nuclear explosions (Yamomoto, 1957; Carpenter et al., 1962; Donn and Ewing, 1962). Bolt (1964) and Mikumo (1968) also noted atmospheric waves recorded on a microbarograph at Berkeley, California from the 1964 $M_W = 9.2$ Alaska earthquake, which were modeled as the effect of the displacement of the bottom of the atmosphere due to the abrupt tectonic uplift associated with the earthquake. Press and Harkrider (1962) derived dispersion curves for air waves with periods up to 25 minutes for a realistic atmospheric structure. They found that the effect of gravity is important in controlling the velocity at periods larger than ~ 4 min, but that group velocities approach the acoustic velocity at short periods; thus they called the traveling atmospheric waves "acoustic-gravity waves." Figure 20 shows their dispersion results.

After negotiation of the atmospheric test ban treaty in 1963, research focus on discrimination and quantification of nuclear tests switched to classical seismology. Many of the microbarograph instruments, which had never been standardized into a global network, ceased operation. However many of those left in 1980 recorded the eruption of Mt. St. Helens (Donn and Balachandran, 1984).

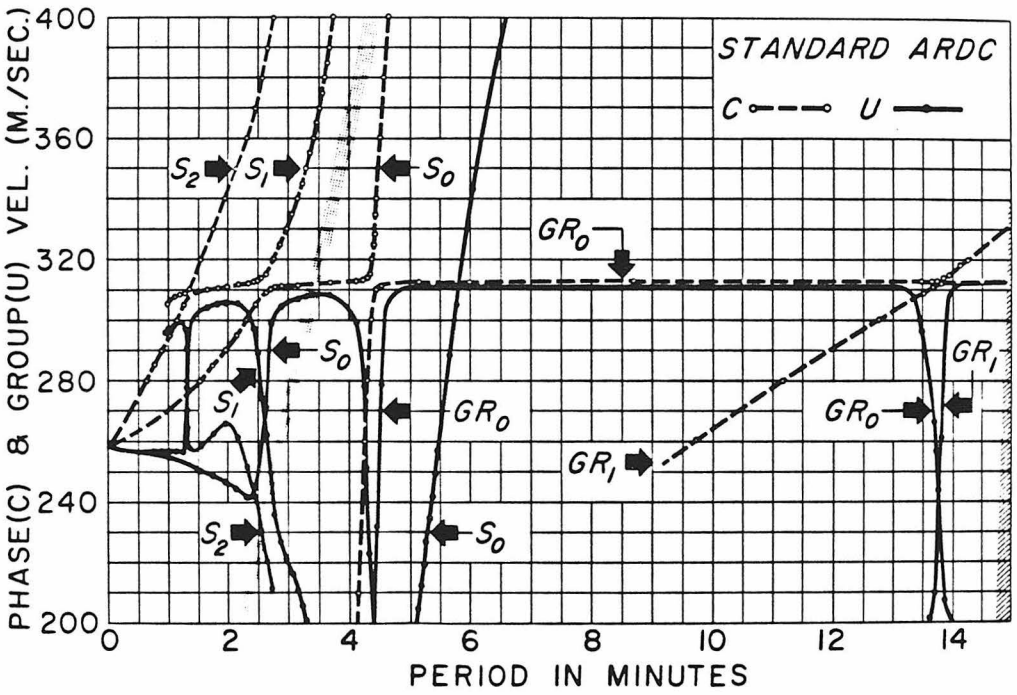

Figure 20. Theoretical phase and group velocity dispersion curves of atmospheric modes for a standard atmospheric structure terminated at 220 km height by an isothermal half-space, from Press and Harkrider (1962). GR_i and S_i denote gravity modes and acoustic modes, respectively.

Observations of Far-Field Air Waves from Volcanic Explosions

The Krakatau eruption in 1883 produced air wave arrivals with durations of several hours on weather barographs around the world. Mt. St. Helens, on the other hand, was globally recorded on microbarographs but was only seen on weather barographs within 400 km of the volcano. In what follows, we note qualitative differences of far-field air waves excited by several volcanic eruptions.

Figure 21 shows a weather barogram of the Krakatau air wave from a station in Pavlovsk, Russia, 88^o away (Gorshkov, 1960), compared with a suite of air wave records from the 1956 eruption of Bezymianny, which has been compared to Mt. St. Helens in terms of explosive power (Passechnik, 1958; Gorshkov, 1960). The vertical scale is arbitrary but the horizontal time scale is the same for all traces. The Krakatau signal endured for over 8 hours, while the air waves from Bezymianny are much more simple and pulse-like, with a dominant period of $\sim$ 15 min. The A_2 waves from Bezymianny, which traveled to the station via the antipode, have similar waveforms to the closest record at 40 km, illustrating that the dispersive effects of the atmosphere at these periods are very small. The Bezymianny records are all from stations within the Soviet Union, so that the instrument effects are likely to be similar. Pekeris (1939) discussed whether the large period of the Krakatau air waves implied an eruption duration of similar size. He estimated a dominant period of about 15 min in the Krakatau records, which can be seen in the trace in Figure 21. Pekeris inferred from his calculations that if the vent dimension was on the order of .5 km, the 15 min air wave period implied a source duration of approximately 15 min, whereas if the effective vent covered the entire island of Krakatau, the source duration may only be several seconds. Records from a pressure gauge in Batavia (now Jakarta, Indonesia)

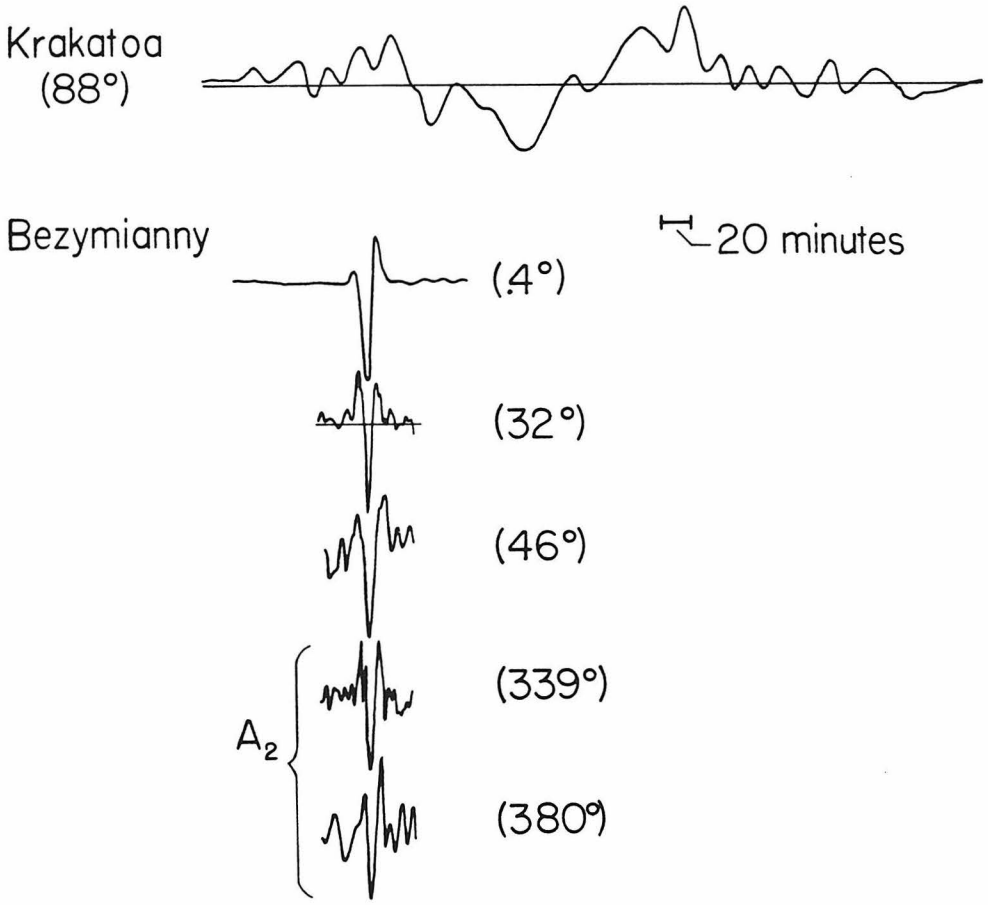

Figure 21. Comparison of observed air waves from the explosive eruptions of Krakatau in 1883, recorded on a weather barogram, with Bezymianny in 1956, recorded on microbarographs across the Soviet Union. A_2 denotes waves that traveled via the antipode. The horizontal scale is the same for the two events.

show many discrete explosions from Krakatau recorded intermittently over about 19 hours (Simkin and Fiske, 1983). Thus from the air wave records we can deduce what is confirmed by direct observations; namely, the Krakatau event consisted of discrete explosions over a protracted time of many hours, whereas the Bezymianny event occurred predominantly as one large isolated explosion.

Figure 22 shows the closest Bezymianny record redrawn with microbarograph recordings of air waves from Mt. St. Helens. The Mt. St. Helens air wave is shorter period and appears to have a double pulse, particularly at Berkeley. The differences among the Mt. St. Helens records are most likely due to differences in the characteristics of the recording devices. Amplitudes of the microbarograms are not shown but will be discussed below. Although the near-field weather barograms of the Mt. St. Helens eruption are preferentially larger to the north (Reed, 1980), the far-field air wave amplitudes are not enhanced in any direction. Recall that the initial blast of Mt. St. Helens was on the north face of the volcano, where a magma chamber was uncapped by the landslide. The northward motion of the landslide mass itself may have also contributed to the northward enhancement of near-field air waves.

Amplitudes in millibars of air waves from various eruptions are plotted versus distance in Figure 23. The Krakatau air waves are an order of magnitude greater than those from Bezymianny, with amplitudes of one millibar — about one thousandth of an atmosphere — at distances of 100^{o}. Bezymianny amplitudes are about twice as large as those from Mt. St. Helens. A few observations are shown of air wave amplitudes from the largest eruption of El Chichón; these are slightly less than but comparable to the air waves from Mt. St. Helens. The $1/\sqrt{\sin\Delta}$ curve shows the geometrical spreading of surface waves over a sphere, which approximately describes the air wave amplitude fall-off at large distances from the source.

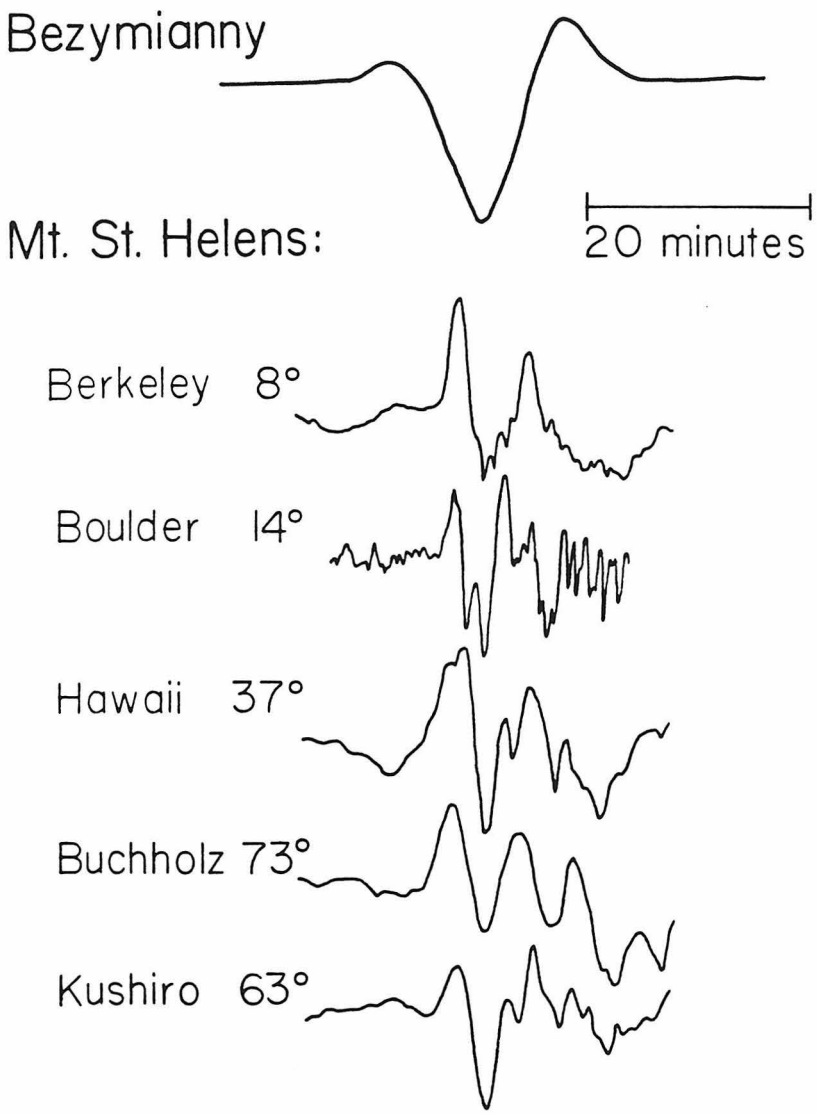

Figure 22. Bezymianny record replotted with air waves observed from the May 18, 1980 eruption of Mt. St. Helens.

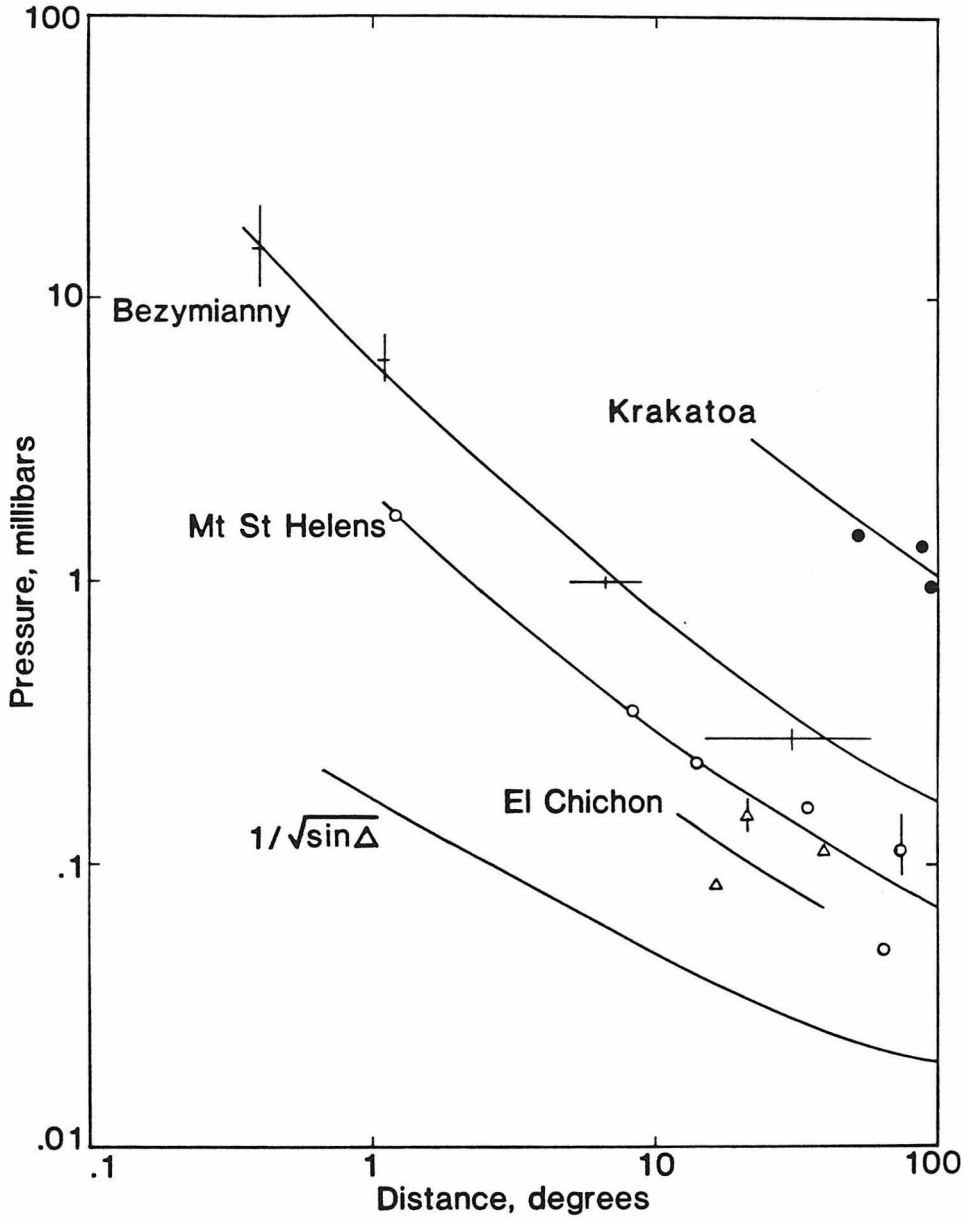

Figure 23. Amplitude decay with distance of air waves from various eruptions. The $1/\sqrt{\sin\Delta}$ curve approximates the amplitude fall-off at distances greater than 10^{o}.

A rather obvious but important point of Figure 23 is that in terms of air wave amplitude, the ranking of the sizes of the eruptions is the same as the ranking by other measures, such as the estimated volume of eruption products, or for the more recent eruptions, the amplitude of the seismic waves associated with the eruptive blast. This also held for the waveforms, with the larger explosions having a longer-period waveform, implying explosions with longer durations or larger vent dimensions.

Air Waves Recorded on Seismographs

As discussed in Section 4 on El Chichón, the passage of the atmospheric wave is occasionally seen on seismograms. There are different mechanisms by which this can occur. If the seismometer mass is not sealed from the atmosphere, it can respond directly to the change in buoyancy force acting on it as the local air density changes during the passage of the air wave. Secondly, if the instrument is sealed from the atmosphere, the mass may still respond to small ground motions coupled with the traveling air wave if the instrument has enough sensitivity at long periods. A sealed instrument may also respond to a local gravitational perturbation as the local air density changes temporarily. Kanamori and Given (1983) estimated the size of the ground displacement y equivalent to a mass motion induced by a pressure change ΔP if the mass responds to buoyancy as being

$$y = \frac{T^2 g}{4\pi^2} \frac{\rho \, l_v}{\rho_m \, l_g} \frac{\Delta P}{P} \tag{2}$$

where T is the period, g is the acceleration of gravity, ρ is the air density, ρ_m is the average density of the effective mass of the seismograph, l_v is the distance between the pendulum pivot and the center of volume of the effective mass of the

seismograph, and l_g is the distance between the pivot point and the center of gravity of the effective mass. For the DWWSSN instrument, this relation becomes

$$\frac{\Delta P}{P} \sim 806 \frac{y}{T^2} \tag{3}$$

where y is measured in cm and T is in seconds. This relation is very approximate and can depend strongly on the local conditions of the instrument site. For example, if the instrument is partially sheltered from the ambient atmosphere in a building or a basement, the effect may be only partial.

Kanamori (pers. comm.) estimated that the buoyancy effect is much larger than the coupled ground motion or gravitational effect for unsealed instruments. Recall from the record section of El Chichón event 94B (Figure 7) that the air wave passage was most clearly recorded on the unsealed DWWSSN instruments, although there is some signal at the air wave arrival time on the buried SRO instruments and IDA instruments as well, presumably recorded by one of the alternate mechanisms. Figure 24 shows a spectacular record of the Mt. St. Helens air wave recorded on the WWSSN seismograph at De Bilt, The Netherlands. Because of the uncertainty in instrument calibration and recording mechanism, we did not use seismograph recordings of air waves to estimate the amplitudes shown in Figure 23.

A Preliminary Model of the Source of Atmospheric Waves from Volcanic Explosions

As a preliminary model of air wave excitation from a volcanic eruption, we use the vertical velocity source assumed by Pekeris (1939) and the dispersion and excitation results for a multilayered atmosphere of Press and Harkrider (1962) and Harkrider (1964*b*). The calculation is essentially identical to that of Pekeris except that

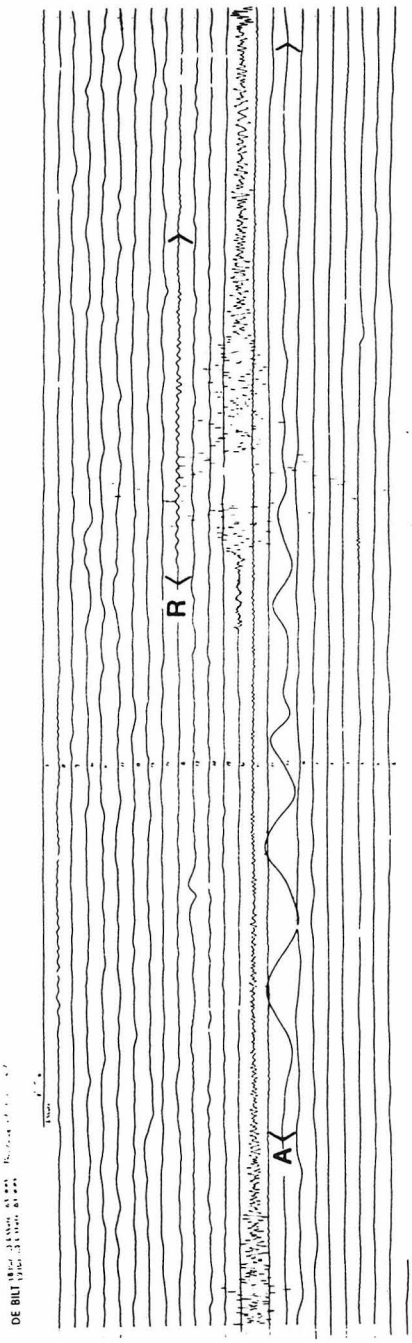

Figure 24. Air wave (A) from Mt. St. Helens recorded on a long-period vertical WWSSN seismograph at De Bilt, The Netherlands. R denotes the Rayleigh wave arrival from Mt. St. Helens.

he was limited by assuming a very simple atmospheric structure that could be solved with analytic approximations. In this model, the vertical velocity source describes the outflow of the volcanic products into the atmosphere.

The spectrum of the pressure variation $p(r,t)$ from a surface source seen by a surface observer at r is given by

$$\hat{p}(\omega,r) = \frac{1}{2\pi}\int_0^\infty \hat{w}(\omega,k)A(\omega,k)J_o(kr)kdk \tag{4}$$

where ω and k are the angular frequency and spatial wave number, $\hat{w}$ is the velocity source excitation term, and $A(\omega,k)$ describes the transfer function of the atmosphere. The source term w is taken to have a Gaussian dependence in space and time:

$$w(r,t) = \frac{1}{\pi^{3/2}\tau^2 L^2} e^{-t^2/\tau^2}\, e^{-r^2/L^2} \tag{5}$$

so that the transformed source function is

$$\hat{w}(\omega,k) = e^{-\omega^2\tau^2/4} e^{-k^2L^2/4} \tag{6}$$

The parameters τ and L are thus measures of the source duration and radius. If $\tau = L = 0$, the calculation is for an instantaneous velocity applied at one point. The integral of $w(r,t)$ over space and time is a volume, interpreted as being the volume of gas introduced into the atmosphere. Then the energy or work done against the atmosphere is the product of this volume with atmospheric pressure, and the source strength is proportional to energy.

We can approximate Equation 4 by using the residue contributions arising from singularities of the atmospheric function $A(\omega,k)$, following Press and Harkrider (1962), Harkrider (1964*b*), and Harkrider and Press (1967). Singularities corresponding to the fundamental gravity mode GR_o and the first three acoustic modes (S_o, S_1, and

S_2) were used in the calculation. The pressure spectrum was then Fourier-transformed to obtain the pressure variation with time, $p(r,t)$. Results of the calculation done for varying source times and dimensions for a source-to-station distance corresponding to Mt. St. Helens seen at Berkeley, California are shown in Figure 25. The pressure variation has been convolved with an instrument response taken from Mikumo (1968)'s calibration of the Berkeley microbarograph. The calculation can approximate the initial part of the observed barogram with some filtering from a finite source to remove higher frequencies. For example, a spatial point source ($L = 0$) with a source duration τ of about 40 s does well in fitting the first pulse of the Berkeley record (Figure 25). Note that the observed record implies a dual event with the second source starting about 5 min after the first. Compilations of eyewitness reports of the eruption and the time function of the explosive sequence inferred from the seismic waves suggest a burst of events at about 2-3 min after the beginning of the sequence but do not show a source at 5 min (see Figure 3). Mikumo and Bolt (1985) did a quantitative analysis of the Mt. St. Helens air waves similar to that above and concluded that the first and second pulse observed at Berkeley were due to the initial lateral blast and subsequent vertical explosion respectively, but they could not explain why the inter-blast time differed from the seismic results. One proposed explanation was that the second source may have been due to a delayed impulse applied at some height in the atmosphere.

By comparing the amplitudes of the observed air wave with our calculation, we infer a source strength of roughly 6 x 10^{22} ergs. This is close to the value of Mikumo and Bolt (1985) at 4 x 10^{22} ergs, and the same order of magnitude as the kinetic energy of the eruption inferred from the seismic signal by Kanamori and Given (1983).

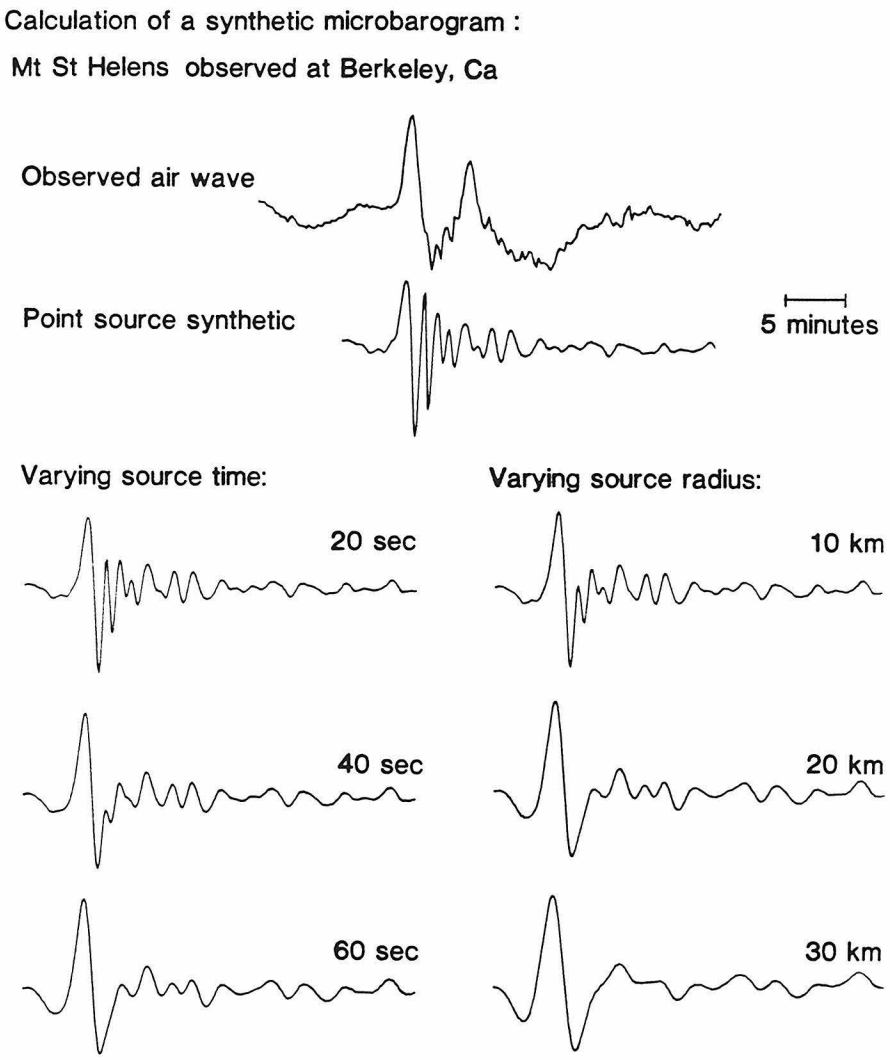

Figure 25. Calculation of synthetic microbarograms from Mt. St. Helens showing the effect of varying the source duration τ and the source radius L .

Conclusions

Atmospheric waves show promise as a quantitative measure of the explosive volcanic source. Air wave amplitudes are larger from larger explosions and in general the ranking of explosive power on this basis is consistent with the ranking inferred from seismic waves associated with the explosions. Further, the dominant period observed in the air waves may be an indication of the combined effects of explosion duration and vent size. The overall character of the air wave records contains information about the time history or multiplicity of discrete explosions at the source. One problem with analyzing air wave records has been in the instability and variety of the pressure-sensing devices used, as well as in the difficulty of separating this kind of low-amplitude signal from background atmospheric variations. Seismographs are sensitive to air waves, and may provide quantitative measures if the recording mechanism and calibration is understood. A preliminary model of air wave excitation from volcanoes where the source strength is proportional to the volume of atmosphere displaced by the outflowing volcanic products matched the frequency content of the observed air wave from Mt. St. Helens with realistic values of the source duration. The source strength or energy estimated from the calculation was comparable to the energy estimated from seismic waves generated by the explosion.

7. Conclusions

Seismic and atmospheric waves generated by explosive volcanic eruptions can be used as a research tool for investigating the nature of the volcanic source. In general,

volcanic explosions of VEI $\geq$ 4 are large enough to be seen teleseismically with existing high-gain, long-period digital instrumentation. Volcanoes with VEI = 3 such as Mt. Asama can be observed if a digital seismograph is deployed within 100 km.

The vertical single force model of a volcanic explosion developed for Mt. St. Helens appears applicable to other volcanoes in general. However, extra components of the source that may not be explicable by the vertical single force have been observed and warrant further study. Mt. St. Helens was an order of magnitude larger than any recent volcano in terms of seismic radiation, but it would have been only marginally recorded if the standard global long-period instrument were still the WWSSN seismograph. Future events of comparable size are necessary for the integration of our results into a coherent picture of the seismic source of a volcanic eruption.

References

Bolt, B. A., Seismic air waves from the great 1964 Alaskan earthquake, *Nature, 202,* 1095-1096, 1964.

Burger, R. W., and C. A. Langston, Source mechanism of the May 18, 1980, Mount St. Helens eruption from regional surface waves, *J. Geophys. Res., 90,* 7653-7664, 1985.

Carpenter, E. W., G. Harwood, and T. Whiteside, Microbarograph records from the Russian large nuclear explosions, *Nature, 4805,* 857, 1961.

Chapman, C. H., A new method for computing synthetic seismograms, *Geophys. J. Roy. Astr. Soc., 54,* 481-518, 1978.

Christiansen, R. L., and D. W. Peterson, Chronology of the 1980 eruptive activity, in *The 1980 Eruptions of Mount St. Helens, Washington, U. S. Geol. Surv. Prof. Pap., 1250,* 17-30, 1981.

De la Cruz-Reyna, S., The March-April 1982 eruptions of El Chichón volcano, Chiapas, Mexico, *EOS, Trans. Am. Geophys. Union, 64,* 1126, 1982.

Donn, W. L., and N. K. Balachandran, Mt. St. Helens eruption of 18 May 1980: Air waves and explosive yield, *Science, 213,* 539-541, 1981.

Donn, W. L., and M. Ewing, Atmospheric waves from nuclear explosions, *J. Geophys. Res., 67,* 1855-1866, 1962.

Gorshkov, G. S., Determination of the explosion energy in some volcanoes according to barograms, *Bull. Volcanol., 23,* 141-144, 1960.

Gorshkov, G. S., Directed volcanic blasts, *Bull. Volcanol., 26,* 83-88, 1963.

Harkrider, D. G., Surface waves in multilayered elastic media: 1. Rayleigh and Love waves from buried sources in a multilayered elastic half space, *Bull. Seismol. Soc. Am., 54,* 627-679, 1964*a*.

Harkrider, D. G., Theoretical and observed acoustic-gravity waves from explosive sources in the atmosphere, *J. Geophys. Res., 69,* 5295-5321, 1964*b*.

Harkrider, D. G., and F. Press, The Krakatoa air-sea waves: An example of pulse propagation in coupled systems, *Geophys. J. Roy. Astr. Soc., 13,* 149-159, 1967.

Haskov, J., De la Cruz-Reyna, S., S. K. Singh, F. Medina, and C. Gutiérrez, Seismic activity related to the March-April 1982 eruptions of El Chichón volcano, Chiapas, Mexico, *Geophys. Res. Lett., 10,* 293-296, 1983.

Hédervári, P., On the energy and magnitude of volcanic eruptions, *Bull. Volcanol., 25,* 373-385, 1963.

Herrin, E., 1968 Seismological tables for P phases, *Bull. Seismol. Soc. Am., 58,* 1193-1195, 1968.

Kanamori, H., and J. W. Given, Analysis of long-period seismic waves excited by the May 18, 1980 eruption of Mount St. Helens - A terrestial monopole?, *J. Geophys. Res., 87,* 5422-5432, 1982.

Kanamori, H., and J. W. Given, Lamb pulse observed in nature, *Geophys. Res. Lett., 10,* 373-376, 1983.

Kanamori, H., J. W. Given, and T. Lay, Analysis of seismic body waves excited by the Mount St. Helens eruption of May 18, 1980, *J. Geophys. Res., 89,* 1856-1866, 1984.

Lamb, H., On the propagation of tremors over the surface of an elastic solid, *Phil. Trans. Roy. Soc. (London) A, 203,* 1-42, 1904.

Medina, F., El volcán Chichón (in Spanish), *GEOS Boletín Union Geofisica Mexicana, 2,* 4-19, 1982.

Mikumo, T., Atmospheric pressure waves and tectonic deformation associated with the Alaskan earthquake of March 28, 1964, *J. Geophys. Res., 73,* 2009-2025, 1968.

Mikumo, T., and B. A. Bolt, Excitation mechanisms of atmospheric pressure waves from the 1980 Mt. St. Helens eruption, *Geophys. J. Roy. Astr. Soc., 81,* 445-463,

1985.

Moore, J. G., and C. J. Rice, Chronology and character of the May 18, 1980 explosive eruptions of Mount St. Helens, in: *Explosive Volcanism: Inception, Evolution, and Hazards, Geophysics Study Committee,* Nat. Acad. Press, Washington, D.C., Chapter 10, 1983.

Newhall, C. G., and S. Self, Volcanic Explosivity Index, *J. Geophys. Res., 87,* 1231-1238, 1982.

Passechnik, I. P., Seismic and air waves which arose during an eruption of the volcano Bezymianny, on March 30, 1956, *Bull. Acad. Sci. USSR Geophys. Ser., 8,* Engl. Trans., 650-653, 1958.

Pekeris, C. L., The propagation of a pulse in the atmosphere, *Proc. Roy. Soc. London, Ser. A, 171,* 434-449, 1939.

Pollack, J. B., and T. P. Ackerman, Possible effects of the El Chichón volcanic cloud on the radiation budget of the northern tropics, *Geophys. Res. Lett., 10,* 1057-1060, 1983.

Pollack, J. B., O. B. Toon, E. F. Danielson, D. J. Hoffman, and J. M. Rosen, The El Chichón volcanic cloud: An introduction, *Geophys. Res. Lett., 10,* 989-992, 1983.

Press, F., and D. Harkrider, Propagation of acoustic-gravity waves in the atmosphere, *J. Geophys. Res., 67,* 3889-3908, 1962.

Reed, J. W., Air pressure waves from Mt. St. Helens eruptions, *EOS, Trans. Am. Geophys. Union, 61,* 1136, 1980.

Richards, P. G., Elementary solutions to Lamb's problem for a point source and their relevance to three-dimensional studies of spontaneous crack propagation, *Bull. Seismol. Soc. Am., 69,* 947-956, 1979.

Shimozuru, D., S. Utibori, N. Gyoda, E. Koyama, T. Miyazaki, T. Matsumoto, N. Osada, and H. Terao, The 1973 explosive activity of Asama volcano - General description of volcanic and seismic events (in Japanese), *Bull. Earthq. Res. Inst. Tokyo Univ., 50,* 115-151, 1975.

Shimozuru, D., N. Gyoda, T. Kagiyama, E. Koyama, M. Hagiwara, and H. Tsuji, The 1982 eruption of Asama volcano (in Japanese), *Bull. Earthq. Res. Inst. Tokyo Univ., 57,* 537-559, 1982.

Simkin, T., and R. S. Fiske, *Krakatau 1883: The Volcanic Eruption and its Effects,* 464 pp., Smithsonian Institution Press, Washington, D.C., 1983.

Simkin, T., L. Siebert, L. McClelland, D. Bridge, C. Newhall, and J. H. Latter, *Smithsonian Institution Volcanoes of the World,* Hutchinson Ross Publishing Company, Stroudsburg, PA., 1981.

Takeo, M., N. Hamada, S. Kashiwabara, and K. Uhira, Analysis of long-period seismic waves excited by the explosive eruption of Mt. Asama on April 8, 1983 (in Japanese), *Kazan, J. Volocanol. Soc. Japan, 29,* 31-44, 1984.

Walck, M. C., The P wave upper mantle structure beneath an active spreading center: The Gulf of California, *Geophys. J. Roy. Astr. Soc., 76,* 697-723, 1984.

Weintraub, B., The disaster of El Chichón, *National Geographic, 162,* 654-684, 1982.

Yamomoto, R., The microbarographic oscillations produced by the explosions of hydrogen bombs in the Marshall Islands, *Bull. Am. Meteorol. Soc., 37,* 406, 1956.

Yokoyama, I., Energetics in active volcanoes, I., *Bull. Earthq. Res. Inst. Tokyo Univ., 35,* 185-195, 1956.

Yokoyama, I., Energetics in active volcanoes, II. and III., *Bull. Earthq. Res. Inst. Tokyo Univ., 35,* 75-107, 1957.